

# Investigation of 3D-~~radiative transfer~~ effects for UV / vis satellite and ground based observations of volcanic plumes

5 Thomas Wagner<sup>1</sup>, Simon Warnach<sup>1,2</sup>, Steffen Beirle<sup>1</sup>, Nicole Bobrowski<sup>2,3</sup>, Adrian Jost<sup>1</sup>, Janis Puķīte<sup>1</sup>, and Nicolas Theys<sup>4</sup>

<sup>1</sup>Satellite Remote Sensing Group, Max Planck Institute for Chemistry, Mainz, Germany

<sup>2</sup>Institute of Environmental Physics, University of Heidelberg, Heidelberg, Germany

<sup>3</sup>Istituto Nazionale Geofisica e Vulcanologia Catania, Italy

10 <sup>4</sup>Royal Belgian Institute for Space Aeronomy (BIRA-IASB), Brussels, Belgium

*Correspondence to:* Thomas Wagner (thomas.wagner@mpic.de)

**Abstract.** We investigate effects of the 3-dimensional (3D) structure of volcanic plumes on the retrieval results of satellite and ground based UV-vis observations. For the analysis of such measurements usually 1D scenarios are assumed (the atmospheric properties only depend on altitude). While 1D assumptions are well suited for the analysis of many atmospheric phenomena, they are usually less appropriate for narrow trace gas plumes. For UV/vis satellite instruments with large ground pixel sizes like GOME-2, SCIAMACHY, or OMI, 3D effects are of minor importance, but usually these observations are not sensitive to small volcanic plumes. In contrast, observations of TROPOMI aboard Sentinel-5P have a much smaller ground pixel size (3.5 x 5.5 km<sup>2</sup>). Thus on the one hand, TROPOMI can detect much smaller plumes than previous instruments. On the other hand 3D effects become more important, because the TROPOMI ground pixel size is smaller than the height of the troposphere and also smaller than horizontal atmospheric photon path lengths in the UV/vis spectral range.

In this study we investigate the following 3D-effects using Monte-Carlo radiative transfer simulations: 1. the light mixing effect caused by horizontal photon paths, 2. the saturation effect for strong SO<sub>2</sub> absorption, 3. geometric effects related to slant illumination and viewing angles, and 4. Plume side effects related to slant illumination angles and photons reaching the sensor from the sides of volcanic plumes. Especially the first two effects can lead to a strong and systematic underestimation of the true trace gas content if 1D retrievals are applied (more than 50% for the light mixing effect, and up to 100% for the saturation effect). Besides the atmospheric radiative transfer, the saturation effect also affects the ~~the~~-spectral retrievals. Geometric effects have a weaker influence on the quantitative analyses, but can lead to a spatial smearing of elevated plumes or even to virtual double plumes. Plume side effects are small for short wavelengths, but can become large for longer wavelengths (up to 100% for slant viewing and illumination angles). For ground based observations, most of the above mentioned 3D effects are not important, because of the narrow FOV and the closer distance between the instrument and the volcanic plume. However, the light mixing effect shows a similar strong dependence on the horizontal plume extension as for satellite observations and should be taken into account for the analysis of ground based observations.

## 35 1 Introduction

SO<sub>2</sub> emitted from volcanoes ~~is~~-has been observed from satellites since about 40 years. After successful first detections for large eruptions by the TOMS instrument (Krueger, 1983), subsequent UV/vis satellite instruments with continuous spectral coverage allowed also the observation of smaller plume amounts (Eisinger and Burrows, 1998; Afe et al., 2004, Khokhar et al., 2005, Krotkov et al., 2006; Yang et al., 2007, 2010; Nowlan et al., 2011; Rix et al., 2012; Hörmann et al., 2013; Li et al., 2013; Penning de Vries et al., 2014; Theys et al., 2015, Fioletov et al., 2016; Zhang et al., 2017; Theys et al., 2017, 2019, 2021a). Furthermore, besides SO<sub>2</sub>, also other trace gases like BrO, OCIO and IO in volcanic plumes could be analysed from these observations (Theys et al., 2009; Heue et al., 2011; Rix et al., 2012; Hörmann et al., 2013; Theys et al., 2014; Schönhardt et al., 2017; Suleiman et al., 2019).

45 Since the launch of the GOME-1 instrument aboard ERS-2 in 1995 (Burrows et al., 1999), the ground pixel size of UV/vis sensors has strongly decreased from 40 x 320 km<sup>2</sup> (GOME-1) down to 3.5 x 5.5 km<sup>2</sup> (TROPOMI), see Table 1. The ground pixel size of TROPOMI is thus only slightly larger or even similar to the extension of ~~plumes emitted from point sources~~ ~~pollution plumes~~, in particular to those from small/medium volcanic eruptions or passive degassing. Thus with TROPOMI, many small/medium volcanic plumes ~~have~~ become detectable, which could not be detected with the former instruments (also the high signal to noise ratio of TROPOMI contributes to the increased sensitivity to small volcanic plumes). An example of TROPOMI observations of SO<sub>2</sub> and BrO for a narrow volcanic plume is shown in Fig. 1 (Warnach, 2022). Shown are the slant column densities (SCD, commonly interpreted as the integrated concentrations along the light path) of both trace gases.

To illustrate the effects of this improved horizontal resolution, we compare the expected trace gas absorptions of small/medium volcanic plumes for different satellite instruments. As a reference, we take the GOME-2 instrument, because from GOME-2 observations it was possible for the first time to observe enhanced BrO amounts for several volcanic plumes (Hörmann et al., 2013). A typical detection limit for the SO<sub>2</sub> SCD in the SO<sub>2</sub> standard fit range (about 312 to 324 nm, Hörmann et al., 2013; Theys et al., 2017, 2021b) is about  $1 \times 10^{16}$  molec/cm<sup>2</sup>. The detection limit is similar for the different instruments, but depends slightly on the signal to noise ratio (see Theys et al., 2019). A SCD of  $1 \times 10^{16}$  molec/cm<sup>2</sup> corresponds to a differential SO<sub>2</sub> optical depth of about 0.001 when measured with a FWHM of about 0.5 nm, ~~like as~~ for the TROPOMI instrument. We will use this optical depth as detection limit for SO<sub>2</sub> in this study. This choice is ~~of course a little bit~~ ~~somewhat~~ arbitrary, but it will serve as a realistic reference point. The detection limit will probably improve in the future using advanced analyses techniques, see e.g. the recent study by Theys et al. (2021a).

If we use the above mentioned SO<sub>2</sub> SCD of  $1 \times 10^{16}$  molec/cm<sup>2</sup> for a GOME-2 observation (as a reference case) and assume that the horizontal extension of ~~an~~ observed volcanic plume is smaller than ~~or equal to the size of~~ a TROPOMI ground pixel (e.g. ~~1 x 1 km<sup>2</sup> compared to 3.5 x 5.5 km<sup>2</sup>~~), we can estimate the SO<sub>2</sub> SCDs observed for instruments with different ground pixel sizes assuming that the measured SCD scales according to the geometric coverage of the volcanic plume. We will see later (light mixing effect) that assuming simple geometry does not perfectly describe these observations, but nevertheless provides a good estimate for the overall effect. The resulting SO<sub>2</sub> SCDs for the different satellite ground pixels are shown in Table 1. The SO<sub>2</sub> SCD for TROPOMI can be higher than the SO<sub>2</sub> SCD for GOME-2 observations by more than 2 orders of magnitude. Even compared to OMI the increase is larger than a factor of 10.

The results of these simple calculations indicate the great potential of TROPOMI observations for the detection of small/medium volcanic plumes: many weak plumes on the scale of TROPOMI ground pixels were invisible for previous sensors. The corresponding increase in the frequency of detection is difficult to quantify, because the exact frequency distribution of plume sizes and amounts of SO<sub>2</sub> and aerosols is not known. In addition, also the self-shielding of plumes by aerosols or clouds formed from the plume probably depends on the plume sizes themselves. Nevertheless, we can quantify the increase in the detection frequency from the satellite observations themselves. For example, Hörmann et al. (2013) found 220 volcanic SO<sub>2</sub> plumes per year in GOME-2 data, whereas Warnach (2022) found 870 SO<sub>2</sub> plumes per year in TROPOMI data (both studies cover different time periods). In view of the SCD ratios discussed above (see Table 1), this increase by a factor of about 4 in the detection frequency seems rather small (see also Theys et al., 2019). The main and simple reason for the small increase of the number of detections is that many volcanic plumes are larger than the size of a TROPOMI pixel.

For such plumes, the SO<sub>2</sub> SCD detected by TROPOMI will be similar to those ~~observed by instruments with larger pixels, up to the size of the plume itself.~~ ~~for the observations with larger ground pixels~~. However, another reason for the rather low increase of detections is related to 3D effects which are the topic of this paper. As shown below, for TROPOMI observations, 3D effects can cause an underestimation of the true ~~trace gas content of the plume~~ ~~amount~~ by more than 50 % (light mixing effect). For plumes with strong SO<sub>2</sub> absorptions, the underestimation can become even larger.

3D effects are fundamental effects and do not only affect UV/vis satellite observations with small ground pixel sizes like TROPOMI. However, for instruments with large ground pixel sizes, 3D effects are typically much smaller than for TROPOMI, and the related errors are typically ignored, because they are smaller than other measurement uncertainties (e.g. related to aerosols or the layer height). For small ground pixel sizes (like for TROPOMI), however, the importance of 3D effects increases because of the following reasons:

- 1) the horizontal pixel dimensions are typically smaller (except for situations with low visibility) than atmospheric photon path lengths (see table 1). Thus light scattered horizontally across the borders of the satellite ground pixels becomes important.
- 2) the horizontal pixel dimensions are smaller than the vertical extent of the troposphere. Thus geometric effects related to slant illumination and viewing geometry become important.
- 3) the horizontal pixel dimensions are similar to those of volcanic plumes. Thus the relative contribution of photons from the sides of the plume increases.
- 4) one TROPOMI ground pixel might cover the very early part of a volcanic plume, for which the SO<sub>2</sub> concentration can be extremely high. Due to the strong SO<sub>2</sub> absorption, photons will then not penetrate the full plume.

Based on these general aspects, different specific 3D effects can be deduced. In this study we investigate and quantify four specific 3D effects. Two of them (light mixing effect and geometrical effect) were already investigated by Schwärzel et al. (2020, 2021) for ground based and aircraft measurements of NO<sub>2</sub>. In this study, we extend these investigations to satellite observations (with different ground pixel sizes). We also investigate two additional 3D effects (saturation effects and plume side effects). The four specific 3D effects are described in more detail below (see also Fig. 2):

a) Light mixing effect: part of the detected photons originates from air masses outside the observed ground pixel (and also from outside the trace gas plume). This leads to a reduction of the trace gas absorption compared to the scenario of a horizontally extended plume (Fig. 2a). Here it should be noted that in case of spatially varying surface albedo or aerosol distributions, the light mixing effect could be further enhanced (over a dark surface surrounded by a bright surface) or decreased (over a bright surface surrounded by a dark surface) will be increased, which is especially important for aerosol retrievals from satellite (Richters, 1990; Lyapustin and Kaufman, 2001). Also the contributions from different parts within the ground pixel depend on the brightness distribution within the pixel. But here we focus on scenarios with constant surface albedo.

b) Saturation effect (Fig. 2b): for strong trace gas absorptions (especially for SO<sub>2</sub> in volcanic plumes) the exact spatial extent of the plume (depending e.g. on the mixing with air from outside) becomes important. If e.g. a trace gas amount is confined in a small part of the satellite ground pixel, the absorption in that part can become very strong. In extreme cases the backscattered light intensity can even approach zero. Then all light measured by the satellite will originate from the remaining part of the satellite ground pixel (outside the narrow plume) where no SO<sub>2</sub> absorption takes place. In such extreme cases, no trace gas absorption will effectively be observed by the satellite. If instead the same amount of molecules is distributed over a larger volume (and thus a larger fraction of the satellite ground pixel), an increased (but typically still too small) SO<sub>2</sub> absorption will be seen. Thus the effective trace gas absorption systematically depends on the horizontal extent of a plume and thus on the temporal evolution of the plume and its mixing with air from outside.

c) Geometric effects: for TROPOMI, the ground pixel size is smaller than the vertical extent of the troposphere. Thus, especially for elevated plumes, geometric effects caused by slant viewing directions and/or slant solar illumination angles can cause a smearing-out and apparent displacement of the volcanic plume compared to its true location. In extreme cases, even double plumes might result (Fig. 2c).

d) Plume side effects: especially if aerosols are present within the plume, edge effects can become important. Their importance increases with decreasing plume size, because a larger fraction of the measured light then reaches the detector

130 from the sides of the plume compared to the top (Fig. 2d). The plume side effect includes the light mixing effect, but adds the dependence on illumination and viewing angle.

Usually all four effects occur for satellite observations at the same time. But in this study we investigate them ~~seperately~~ separately in order to assess their importance for specific measurement scenarios. For these investigations we use the 3D Monte Carlo model TRACY-2 (Wagner et al., 2007; Kern et al., 2010).

135 It should be noted that for ground based measurements, a fifth 3D effect becomes important, the so-called light dilution effect (Kern et al., 2010). It has contributions from the light mixing effect, but is mainly caused by light scattered into the line of sight of the instrument between the plume and the instrument without having crossed the (localised) trace gas plume. Since for satellite observations, the observed light typically has not traversed the whole atmosphere, but part of it is scattered above the trace gas layer (leading to air mass factors (AMFs) below unity; for the ~~difinition-definition~~ of the AMF, see section 2), the light dilution effect is already implicitly considered in radiative transfer simulations (even in calculations of 1D AMFs). In this study the light dilution effect is thus explored as a separate effect only for ground based observations.

140 The paper is organised as follows. In section 2 the 3D Monte-Carlo radiative transfer model TRACY-2 is introduced. Sections 3 to 6 present simulations of the above mentioned four 3D-effects. Section 7 discusses 3D-effects for ground based observations, and section 8 presents a summary and outlook.

## 145 2 The Monte Carlo radiative transfer model TRACY-2

The Monte Carlo radiative transfer model TRACY-2 was developed by Tim Deutschmann at University of Heidelberg, Germany. TRACY-2 allows the simulation of individual photon paths between the Sun and an observing instrument with flexible boundary conditions. The location and properties of the detector (e.g. width and shape of the field of view, FOV) can be freely chosen. The atmospheric properties, especially the trace gas and aerosol distributions, can be varied in all three dimensions. TRACY-2 is based on the backward Monte Carlo method: a photon emerges from a detector and undergoes various interactions in the atmosphere until the photon leaves the top of the atmosphere (where it is ‘forced’ into the sun with appropriate weighting factors). A large number of random photon paths is generated reproducing the light contributing to the simulated measurement. Depending on the atmospheric conditions and the FOV, the number of simulated photons in this study ranges from 10 ~~thousand-thousand~~ to 1 million. Air mass factors (AMFs) are derived from the modelled radiances with (I) and without ( $I_0$ ) the absorber of interest:

$$AMF = \frac{\ln\left(\frac{I_0}{I}\right)}{VCD \cdot \sigma} \quad (1)$$

160 with  $\sigma$  being the absorption cross section of the considered trace gas and VCD the vertical column density (the vertically integrated trace gas concentration). Good agreement between TRACY-2 and other radiative transfer models was found in an extensive comparison exercise (Wagner et al., 2007). In Fig. 3 an exemplary simulation with TRACY-2 is shown for a TROPOMI observation of an idealised narrow plume.

For the simulations, an atmospheric domain extending  $\pm 20^\circ$  in latitude and longitude around the plume location (centered at  $0^\circ$  longitude and  $0^\circ$  latitude) and from the surface to 1000 km altitude is chosen. The horizontal resolution is high close to the center (500 m from the center until 10 km) and coarser outside (11.1 km until 111 km; 55.5 km until 555 km, and one grid cell from 555 km to ~~20°2222 km~~). For some simulations (see Figs. 4-5 and 20) even a finer horizontal grid was used to investigate the effect of very narrow plumes (100 m until 22.5 km, 55.5 km until 555 km). The vertical resolution was set to 200 m below 6 km, 1 km until 25 km, 2 km until 45 km, and 5 km until 100 km altitude, and one layer from 100 km to 1000 km. The surface albedo was set to 5%. This value was chosen, because typical albedo values in the considered wavelength

ranges over volcanic areas are close to this value (see Fig. A1.1 in appendix A1). The exact choice of the surface albedo is, nevertheless, not critical, because the ratio of AMFs for narrow plumes and those for horizontally extended plumes hardly depends on the surface albedo (see Fig. A1.2 in appendix A1). Vertical profiles of temperature, pressure and O<sub>3</sub> concentration are taken from the US standard atmosphere (United States Committee on Extension to the Standard

175 Atmosphere, 1976).

The satellite instrument is placed at 824 km above sea level representing the altitude of the TROPOMI instrument. For the investigation of the effects of very narrow plumes (Figs. 4-5 and 20) as well as for the plume scans (like in Fig. 56) a narrow FOV of 0.014° (corresponding to a ground pixel diameter of 200 m) is used. For the simulations of real satellite measurements, rectangular FOVs corresponding to the nominal ground pixel sizes of the different satellite instruments (see

180 table 1) are used.

Volcanic plumes are defined for SO<sub>2</sub>, BrO, and IO based on ground based and satellite observations (for details see section 2.1). Simulations are performed for selected wavelengths relevant for the considered trace gases: for SO<sub>2</sub>, four wavelengths (313.1, 324.15, 332.0, 370.3 nm) are chosen for the dominant absorption bands of the different fit ranges (Theys et al., 2017). Simulations for BrO are performed at 340 nm, and for IO (and NO<sub>2</sub>, and H<sub>2</sub>O) at 440 nm. Note that substantial amounts of NO<sub>2</sub> are not expected in volcanic plumes. Also, the increase of the atmospheric water vapor absorption due to water vapor inside the volcanic plume is expected to be very small. Nevertheless, because NO<sub>2</sub> and H<sub>2</sub>O are often analysed in the same spectral range as IO, the IO results are also representative for H<sub>2</sub>O and NO<sub>2</sub> observations if the ratios of the respective differential cross sections in the spectral range around 440 nm are applied (see section 2.1.3 and appendix A1A2). Thus the IO results could also be used for the potential detection of enhanced NO<sub>2</sub> or H<sub>2</sub>O in volcanic (or other emission)

190 plumes.

AMFs are calculated according to equation 1 for single wavelengths ('monochromatic AMFs'). Thus the wavelength dependence of the AMF (Marquardt et al. 2000; Puķīte et al., 2010, 2016) is not explicitly taken into account, which for strong absorbers usually causes an overestimation of the monochromatic AMFs compared to the true AMFs. In a case study (section 4.3) the effect of the wavelength dependence of the AMF was investigated. It was found that the wavelength dependence of the AMF is negligible for most scenarios (with weak absorptions) considered here. Only for scenarios with strong SO<sub>2</sub> absorptions (with optical depth larger than 0.05 to 0.1) the wavelength dependence of the AMF becomes important and further amplifies the underestimation of the true AMF. But such scenarios can easily be identified and excluded from the data analysis, and for such scenarios wavelengths with weaker SO<sub>2</sub> absorptions should be selected. Thus, the effect of the wavelength dependence of the AMF is ignored in this study, and the main findings can be derived from monochromatic AMFs (equation 1). While this strongly reduces the computational effort, the computation time for the 3D simulations still remains rather high. The calculation of a single monochromatic 3D AMF takes about 5 min on a state of the art notebook.

200

## 2.1 Selected trace gas scenarios

205

The construction of realistic trace gas scenarios is a challenging task. The assumed trace gas plumes should represent realistic distributions, which are based on ground based observations. They should also fit to satellite observations of narrow plumes, which, however, are often close to the detection limit, because the plumes only cover part of the satellite ground pixel. From the satellite observations no information on the sub-ground pixel scale can be obtained.

210 For this study, trace gas scenarios were set up for SO<sub>2</sub>, BrO, and IO. BrO and IO are typically weak absorbers with absorption optical depths clearly below 0.1. Thus they do not significantly affect the atmospheric light path distribution, and only the relative spatial distribution, but not the absolute trace gas amount is important for the calculation of the AMFs. The scenarios for SO<sub>2</sub>, BrO, and IO were chosen, because these trace gases were already observed in volcanic plumes. Moreover,

215 the corresponding wavelengths cover the spectral range from about 310 to 440 nm, over which the probability of Rayleigh scattering strongly changes (by a factor of 4). Thus the light mixing effect (and also the geometric effect and the side scattering effect) are expected to differ substantially for the chosen wavelengths. A second set of wavelengths is selected for the SO<sub>2</sub> scenarios (4 wavelengths covering the spectral range from about 313 to 370 nm, for details see section 2.14). But here we are not primarily interested in the effect of the wavelength dependence of Rayleigh scattering, but rather on the strong wavelength dependence of the SO<sub>2</sub> absorption cross section. This second set of wavelengths is used to study the saturation effect for SO<sub>2</sub>.

220 The trace gas scenarios defined below will be used to decide whether the trace gas absorption of a given measurement scenario will be above the detection limit or not. For that purpose we also chose the following detection limits: optical depths of 0.0005 for BrO and IO, and 0.001 for SO<sub>2</sub>. Of course these choices are ~~somehow-somewhat~~ arbitrary, but represent realistic reference points for single observations. Here it should be noted that in some cases (e.g. for continuous degassing volcanoes and stable wind fields) many observations might be averaged. In such cases the detection limits will decrease for the statistical mean. Also, for possibly improved future algorithms and instruments the detection limit might be reduced. Then also observations with trace gas absorptions currently below the detection limit will become significant leading to a larger total number of more observations are expected to become significant observations. Thus the results obtained in this study should be seen as a general orientation. The differential cross sections (high-frequency amplitudes) used to convert the SCDs of the different trace gases into optical depths are given in Table ~~A1A2~~.1 in the appendix ~~A1A2~~. Here it should be noted that in our radiative transfer simulations the absolute absorption cross sections were used.

### 2.1.1 Size of the volcanic plumes

235 Plume diameters close to volcanic vents are typically  $\leq 1$  km (see e.g. Bobrowski et al., 2003; Bobrowski and Platt, 2007; Dinger et al., 2021). Thus we assume as a standard scenario a plume with an extension of  $1 \times 1 \times 1$  km<sup>3</sup>. Of course this is a simplification, since realistic plumes close to the volcanic vent will be more complex (including e.g. a vertical updraft above the vent, and a horizontal outflow part). But here we are interested in the basic effects. In addition to the standard scenario, we also assume plumes with larger horizontal extensions, but with the same vertical extent and the same total amount of molecules. This allows us to study the light mixing effect and saturation effect depending on the turbulent dilution state of the plume. For simplicity we assume that the dilution will only occur in the horizontal dimensions. ~~We~~ For most simulations (light mixing effect and saturation effect) we investigate plumes in ~~three-four~~ altitude ranges: 0-1 km, 5-6 km, ~~and~~ 10-11 km, and 15-16 km. For the study of the geometric effects and the side scattering effects only plumes at specific heights are chosen to illustrate the general dependencies.

### 2.1.2 BrO

245 Maximum BrO SCDs measured from ground range up to  $1.4 \cdot 10^{15}$  molec/cm<sup>2</sup> (Bobrowski et al., 2003; Bobrowski and Platt, 2007; Bobrowski and Giuffrida, 2012). However, because of the sparseness of these observations, the maximum occurring BrO SCDs will probably be higher, and we use in the following a maximum ~~value-VCD~~ of  $5 \cdot 10^{15}$  molec/cm<sup>2</sup> (for the 'standard plume' of  $1 \times 1 \times 1$  km<sup>3</sup>). Here we assume that the measured SCD is similar to the corresponding VCD. This assumption is approximately fulfilled for ground based measurements in zenith direction, or if the plume has an almost circular cross section. Applying simple geometric consideration, this results in a VCD of  $2.6 \cdot 10^{14}$  molec/cm<sup>2</sup> for a TROPOMI observation with a ground pixel size of  $3.5 \times 5.5$  km<sup>2</sup> ~~(assuming that for the ground based measurements the SCD equals the VCD, i.e. assuming that the ground based telescope is directed towards the zenith).~~ This value is similar to maximum BrO VCDs observed by TROPOMI for narrow plumes (plumes with extensions of a TROPOMI ground pixel or

less). For such cases, Warnach (2022) observed BrO VCDs up to about  $2.5 \cdot 10^{14}$  molec/cm<sup>2</sup> (assuming a 1D-AMF of 0.5 corresponding to plumes close to the surface). The BrO scenario corresponds to a total number of BrO molecules in the standard plume (1 x 1 x 1 km<sup>3</sup>) of  $5 \cdot 10^{25}$ . An overview about the corresponding BrO VCDs for the different horizontal plume extensions is given in Table 3.

### 2.1.3 IO

Also IO is a weak absorber, but because of the sparseness of IO observations in volcanic plumes (e.g. Schönhardt et al., 2017), we simply use the same VCD ( $5 \cdot 10^{15}$  molec/cm<sup>2</sup>) as for BrO for the standard plume (1 x 1 x 1 km<sup>3</sup>) corresponding to a VCD of  $2.6 \cdot 10^{14}$  molec/cm<sup>2</sup> for a TROPOMI observation. This value probably overestimates the true IO amounts in volcanic plumes. But since IO is a weak absorber, the results are representative also for plumes with smaller IO amounts.

The corresponding VCDs for the different horizontal plume extensions are shown in Table 3.

The results of the IO scenarios could be also transferred to measurements of NO<sub>2</sub> and H<sub>2</sub>O, if they were analysed in the same spectral range (around 440 nm). To convert the IO results to the corresponding NO<sub>2</sub> and H<sub>2</sub>O results, just the ratios of the cross sections have to be applied. With a (differential) absorption cross section of  $3 \cdot 10^{19}$  cm<sup>2</sup> for NO<sub>2</sub>, and  $3 \cdot 10^{26}$  cm<sup>2</sup> for H<sub>2</sub>O (see table A1.1), all IO VCDs and SCDs would have to be multiplied by 83 and  $8.3 \cdot 10^8$  for NO<sub>2</sub> and H<sub>2</sub>O, respectively. The IO VCD for the standard plume ( $5 \cdot 10^{15}$  molec/cm<sup>2</sup>) corresponds to a NO<sub>2</sub> VCD of  $4.15 \cdot 10^{17}$  molec/cm<sup>2</sup> and a H<sub>2</sub>O VCD of  $4.15 \cdot 10^{24}$  molec/cm<sup>2</sup>.

### 2.1.4 SO<sub>2</sub>

~~SO<sub>2</sub>-absorptions of volcanic plumes can cover a wide range.~~ SO<sub>2</sub> can act as weak, but also as a very strong absorber, depending on the one hand on the amount of molecules in a plume, which can vary over many orders of magnitude. On the other hand it strongly depends on the selected wavelength range. At short wavelengths, the SO<sub>2</sub> absorption cross section is much stronger than at longer wavelengths. Around 310 nm, the absorption cross section is about  $3.5 \cdot 10^{-19}$  cm<sup>2</sup>, around 320 nm about  $5 \cdot 10^{-20}$  cm<sup>2</sup>, around 330 nm about  $2 \cdot 10^{-21}$  cm<sup>2</sup>, and around 370 nm  $6 \cdot 10^{-22}$  cm<sup>2</sup> (see Fig. 64).

The standard wavelength range for the TROPOMI SO<sub>2</sub> analysis is 312 to 326 nm (Theys et al., 2021b). This wavelength range is especially well suited for plumes with small SO<sub>2</sub> amounts. For the scenario with SO<sub>2</sub> as a weak absorber we chose a VCD of  $1 \cdot 10^{18}$  molec/cm<sup>2</sup> for the standard plume (1 x 1 x 1 km<sup>3</sup>). For a TROPOMI observation this corresponds to a VCD of  $5.2 \cdot 10^{16}$  molec/cm<sup>2</sup> and an differential optical depth of about  $1 \cdot 10^{-19}$  cm<sup>2</sup>, see table A1.1 (the differential optical depth would be by about 20% larger without the adaptation of the SO<sub>2</sub> absorption cross section to the TROPOMI spectral resolution). Here it should be noted that the (absolute) optical depth of the standard plume itself (1 x 1 x 1 km<sup>3</sup>) is much larger (about 0.25). Thus for very narrow plumes, the weak SO<sub>2</sub> scenario is already at the edge between a weak and strong absorber. But for larger plumes, the corresponding SO<sub>2</sub> absorption quickly decreases (for a 2 x 2 x 1 km<sup>3</sup> plume it is about 0.06).

In addition to this scenario, we also consider 4 scenarios with SO<sub>2</sub> as a strong absorber (in the standard TROPOMI fit range). The maximum SO<sub>2</sub> VCD is chosen according to Kern et al. (2020), who observed a very high SO<sub>2</sub> VCD (about 2 to  $3 \cdot 10^{20}$  molec/cm<sup>2</sup>) over an about 2 km wide plume from the Kilauea volcano about 4 km downwind of the vent. Thus we use a VCD of  $4 \cdot 10^{20}$  molec/cm<sup>2</sup> as maximum VCD for the standard plume (1 x 1 x 1 km<sup>3</sup>). A very high SO<sub>2</sub> SCD of  $3.2 \cdot 10^{19}$  molec/cm<sup>2</sup> was also observed at Mount Etna by Bobrowski et al. (2010). Very high SO<sub>2</sub> VCDs up to  $5 \cdot 10^{19}$  molec/cm<sup>2</sup> were also observed by TROPOMI for the La Palma eruption in Summer-September to December 2021 (e.g. Warnach, 2022). Here the plume usually covered several TROPOMI ground pixels, but with maximum SO<sub>2</sub> VCDs for individual TROPOMI pixels

300 indicating a characteristic horizontal plume extension similar to a TROPOMI pixel. To cover a large range of strong SO<sub>2</sub>  
absorptions, we chose the following VCDs (for a 1 x 1 x 1 km<sup>3</sup> plume): 1 · 10<sup>19</sup> molec/cm<sup>2</sup>, 2.5 · 10<sup>19</sup> molec/cm<sup>2</sup>, 1 · 10<sup>20</sup>  
molec/cm<sup>2</sup>, and 4 · 10<sup>20</sup> molec/cm<sup>2</sup>. The corresponding VCDs for the different SO<sub>2</sub> scenarios and horizontal plume  
extensions are given in Table 3. The standard fit range is represented by simulations at 313.1 nm (where the strongest SO<sub>2</sub>  
absorption peak is located). In addition, also simulations at 324.15 nm, 332.0 nm, 370.3 nm are performed. The  
corresponding optical depths for the chosen wavelengths are summarised in Table 4.

305

## 2.2 Aerosol input data

For the investigation of aerosol effects two scenarios are considered. For both scenarios an aerosol optical depth (AOD) of  
10 (for the 1 x 1 x 1 km<sup>3</sup> plume) is assumed, either with purely scattering aerosols (SSA = 1) or strongly absorbing aerosols  
310 (SSA=0.8). The first case represents plumes with sulfuric acid aerosols, the second case plumes with ash particles. The phase  
function is represented by the Henyey-Greenstein model with an asymmetry parameter of 0.68. These simplified scenarios  
were chosen to represent the basic characteristics of aerosol containing volcanic plumes. It should be noted that there is a  
lack of observations of the total amount of aerosols in fresh plumes, mainly because the high AOD in such situations itself  
prevents accurate measurements of the AOD. Like for the trace gases, also the aerosol amount is kept constant for the  
315 different horizontal plume extension leading to different AODs for different horizontal plume extensions (see table 3).

## 3 Light mixing effect

The effect of horizontal light paths on satellite observations has first been investigated for aerosol retrievals from satellites  
320 (Richter, 1990; Lyapustin and Kaufman, 2001). Such retrievals are based on radiance measurements, and the effect of  
horizontal light paths can strongly affect the measurements in the presence of strong spatial radiance contrasts, e.g. caused  
by sea-land boundaries or cloud edges. In such cases, horizontal light paths cause an increase (decrease) of the radiance  
above the dark (bright) scene and thus systematically affects the aerosol retrieval. This effect (for absolute radiance  
measurements) was referred to as adjacency effect (Richter, 1990).

325 Trace gas measurements are usually not based on absolute radiance measurements but on narrow-band relative (differential)  
absorptions. ~~Also for~~ such measurements, horizontal light paths can ~~also~~ play an important role. But in contrast to aerosol  
measurements (based on absolute radiances), horizontal light paths affect the measurements even for scenes without spatial  
radiance contrasts (if spatial gradients of the trace gas of interest are present). In order to distinguish the effect of horizontal  
light paths on trace gas measurements from those on absolute radiance measurements (adjacency effect), we refer to it in this  
330 study as light mixing effect.

Light mixing effects for trace gas measurements have first been investigated by Schwärzel et al. (2020; 2021) for ground  
based and aircraft measurements. They found that like for the aerosol measurements, the light mixing effect for trace gas  
measurements causes a spatial smoothing of the trace gas signals.

335 Here we extend these investigations to satellite observations. First we investigate the fundamental effects of horizontal  
photon paths (for scenarios without aerosols). Then we quantify the light mixing effect for ground pixel sizes of different  
satellite sensors and also scenarios with aerosols taking into account also realistic detection limits.

### 3.1 General findings and dependencies of the light mixing effect for trace gas observations

340 Fig. 4-5 presents trace gas AMFs for different plume altitudes and wavelengths as function of the horizontal plume  
extension. The vertical plume thickness is 1 km. The wavelengths were chosen to represent typical trace gas analyses



relevant for volcanic studies (SO<sub>2</sub> around 313 nm, BrO around 340 nm, IO around 440 nm, see section 2.1). The AMFs strongly depend on the horizontal plume extension. This dependency gets stronger towards shorter wavelengths, because of the higher probability of Rayleigh scattering and thus a larger contribution of photons originating from outside the satellite's FOV. Interestingly, the normalised AMFs (divided by the corresponding 1D AMFs) for different altitudes show a similar dependence on the horizontal plume extension indicating compensating effects of the increasing free path lengths and the decreasing scattering probability with increasing altitude (because of the decreasing air density). The results in Fig. 4-5 show that the light mixing effect can cause a strong underestimation of the trace gas amounts of a volcanic plume if a 1D AMF is used in the data analysis. The underestimation is largest for small plumes and short wavelengths (up to > 70%).

In Fig. 5-6 so-called plume scans for plumes with different horizontal extensions are presented for a plume altitude of 5 - 6 km (results for other plume altitudes are shown in Fig. A3.1 in appendix A3). The highest AMFs occur directly above the plume center, but even these AMFs are systematically smaller compared to the corresponding 1D AMFs (orange horizontal lines). The deviation is strongest for short wavelengths and narrow plumes. The AMFs slightly decrease from the plume center towards the edges. Outside the plume they decrease rapidly, but stay clearly above zero.

This 'smoothing' of the AMF (compared to the horizontal extent of the plume) reflects the effect of horizontal photons paths and is directly connected to the atmospheric visibility. Towards short wavelengths, the free photon paths get shorter and the scattering probability gets higher. Thus the smoothing effect is strongest at short wavelengths. These general dependencies are also found for other plume altitudes (see Fig. A3.1 in appendix A3), but the absolute values of the AMFs strongly increase with increasing plume height both for narrow plumes and horizontally extended plumes (while the ratios of the AMFs for narrow plumes to those of horizontally extended plumes are similar for the different plume altitudes).

One interesting question is whether the decrease of the AMF above the plume (compared to the 1D AMF) and the increase outside the plume (compared to a zero AMF) exactly compensates each other. Indications for such a compensation are illustrated in Fig. 7 (note that for a quantitative interpretation, two horizontal dimensions have to be considered). To answer this question, simulations for satellite observations with a very large FOV corresponding to a ground pixel size of 200 x 200 km<sup>2</sup> are performed. Such large ground pixels are larger than typical horizontal photon paths (see Table 2). Thus almost all photons which have 'seen' the trace gas plume will stay inside the FOV.

The simulation results (together with similar results for a TROPOMI FOV) for a wavelength of 313 nm and a plume height of 5-6 km are shown in Fig. 8 (results for other combinations of wavelengths and plume altitudes are shown in Fig. A3.2 in appendix A3). The top panels present the detected-retrieved fraction of the plume amount-content (using a 1D-AMF) as function of the horizontal plume extension. This fraction is defined as the ratio of the retrieved number of trace gas molecules using a 1D AMF and the true number of trace gas molecules of the plume (as used as input in the radiative transfer simulations). The detected-retrieved fraction of the plume amount-content is calculated as follows: First the simulated SCD for 3D plumes is divided by the corresponding 1D AMF yielding the average VCD across the satellite ground pixel. This VCD is then multiplied by the area of the ground pixel size yielding the total number of molecules. Finally, this value is divided by the number of trace gas molecules used as input for the simulations. Note that if the satellite ground pixel is smaller than the plume, only the input number of plume molecules covered by the satellite ground pixels is used to calculate the retrieved fraction of the plume content.

For TROPOMI, the retrieved fractions of the plume amount largely underestimate (between about 15 and 60% by >50%, depending on altitude and wavelength) the input trace gas amounts for small plume sizes, in agreement with the results shown in Figs. 4-5 and 56. The largest underestimation occurs for short wavelengths and a plume size similar to the ground pixel size. This can be understood by the results of the plume scans shown in Fig. 56, where the AMFs at the plume edges are the smallest within the plume. For plumes larger than the TROPOMI ground pixel, the retrieved fraction of the plume content (within the ground pixel size) then increases with plume size, because these scenarios converge to the 1D scenario (horizontally homogeneous trace gas layer).

385 Interestingly, for the large FOV (corresponding to a satellite ground pixel of 200 x 200 km<sup>2</sup>) the retrieved fractions of the plume amount ~~is-are~~ close to unity independent ~~from-of~~ the plume size. This confirms the above expectation that the decrease of the AMF in the area of the plume (compared to the 1D AMF) and the increase of the AMF outside the plume (compared to zero) compensate each other. In conclusion we find that the correct plume amount can be retrieved using 1D AMFs only for two extreme cases:

390 a) The ground pixel size is much larger than the free photon path length and the plume size (Fig. 8 right). However, in such cases the trace gas absorption is very weak and usually below the detection limit (see Fig. 8 bottom right). Thus small/medium volcanic plumes can usually not be detected by instruments with a large ground pixel size.

b) The plume ~~is homogenous and size is~~ much larger than the free photon path length (and the ground pixel size). ~~While the first condition is usually not well fulfilled, the second condition~~ This is typically fulfilled for strong eruptions. But such plumes are large and can usually be detected by satellite instruments with low spatial resolution (no observations with high spatial resolution are needed). ~~For such large ground pixel sizes, also the effect of horizontal gradients will be rather small.~~ Thus small plumes (like for small/medium volcanic eruptions or degassing events) can only be observed by sensors with a small ground pixel size (like TROPOMI). But for such observations the retrieved trace gas amount will be systematically and strongly underestimated if 1D AMFs are applied in the data analysis.

400

### 3.2 Quantitative analysis for different ground pixel sizes taking into account the detection limit of the spectral retrieval

As shown in the previous section, all molecules of a volcanic plume could in principle be retrieved with a 1D AMF if the satellite ground pixel would be large (> about 100 x 100 km<sup>2</sup>). Thus, even for satellite measurements with small ground pixels it should be possible to retrieve all molecules of a volcanic plume if the results of many neighboring ground pixels (surrounding the volcanic plume) were summed up. However, since the AMFs for pixels outside the volcanic plume are typically rather small (Fig. 56), for most of the observations of neighboring ground pixels the trace gas absorption will be below the detection limit. This finding is confirmed in Fig. 9, which shows simulation results for the trace gas scenarios for the weak absorbers introduced in section 2.1. Here again it should be noted that these results are valid only for the assumed trace gas scenarios and detection limits. For higher plume amounts and/or lower detection limits, lower SCDs, e.g. those for the neighboring pixels might be above the detection limit. Moreover, for scenarios with constant emissions (degassing) and stable wind fields, several measurements could be averaged, which would also lower the detection limit which is usually determined by photon noise. Nevertheless, from these simulations we derive the following general conclusions:

415 a) The trace gas SCDs from neighboring pixels are usually rather small. For TROPOMI observations the ratios of the maximum SCDs from the neighboring pixels relative to the SCDs of the center pixel range from 2% for 440 nm to 87% for 313 nm. Thus these measurements will often be below the detection limit.

b) even if measurements of the neighboring pixels are above the detection limit, their contribution to the detected total plume amount is small. For the two closest neighboring pixels (because of symmetry in total 4) their additional contribution ranges from about 64% (440 nm) to about 4611% (313 nm) ~~(relative contributions with respect to the true plume content).~~

420 c) for OMI, SCIAMACHY, or GOME-2, the SCDs of the neighboring pixels are always below the detection limit for the scenarios (with narrow volcanic plumes) considered ~~here (see in Table 3).~~

Fig. 10 shows the retrieved fraction of the plume molecules (for a 1 x 1 x 1 km<sup>3</sup> plume ~~between 5 and 6 kmat different altitudes~~) as function of the ground pixel size for the three selected wavelengths. As discussed before, the strongest underestimation is found for TROPOMI and for short wavelengths. For SCIAMACHY and GOME-2 observations, the underestimation is only between a few and 15 percent. However, for these sensors the retrieved trace gas SCDs are below the detection limit for the narrow plumes considered here. Interestingly, very similar results are found for 313 and 340 nm,

probably because of some compensating effects of the increase of the light mixing effect, but also an increase of the probability for multiple scattering towards shorter wavelengths. For plumes close to the surface (0 - 1 km altitude) very similar fractions are found (~~not shown~~) as for the plume between 5 and 6 km, but because of the decreasing sensitivity of the satellite observations towards the ground, the corresponding trace gas absorptions are smaller and for the weak SO<sub>2</sub> scenario even below the detection limit. For plumes at higher altitudes, the underestimation becomes smaller because the probability of multiple scattering due to Rayleigh scattering decreases and thus the differences of the AMFs for narrow and horizontally extended plumes become smaller.

### 3.3 Influence of aerosols

Fig. 11 presents AMFs (similar to Fig. 56) and normalised radiances (radiance/irradiance) for plume scans in near-nadir viewing geometry (solar zenith angle, SZA=0°) for different wavelengths (for SO<sub>2</sub> at 313 nm, BrO at 340 nm, and IO at 440 nm) and aerosol scenarios. The plumes are located between 5 and 6 km and contain the trace gas together with the aerosols (results for other plume heights are shown in Fig. A3.3 in appendix A3). Again the amount of molecules in the plume content is assumed to be constant (and homogeneously distributed), ~~that thus~~ the trace gas VCDs and AOD vary with the horizontal plume extent (see Table 3). The aerosols are assumed either purely scattering (SSA=1) or strongly absorbing (SSA=0.8). The different colours in Fig. 11 and Fig. A3.3 represent AMFs and normalised radiances for plumes with different horizontal extensions (from 1 x 1 km<sup>2</sup> to 40 x 40 km<sup>2</sup>).

For small plume extensions (and thus high ~~aerosol-extinction~~AOD in the plume) a strong effect of aerosols is seen (except for short wavelengths and plumes close to the surface): for the scenarios with scattering aerosols, both the AMF and the normalised radiance increase compared to the scenarios without aerosols (Fig. 56). For the scenarios with absorbing aerosols the opposite is found. For the interpretation of the simulated radiances it is important to take into account that especially for the low altitude plumes a substantial fraction of the atmospheric molecules is still located above the volcanic plume, which scatter the sun light towards the instruments without having 'seen' the plume. Thus, even for narrow plumes with absorbing aerosols the reduction of the observed radiance above the plume is relatively small. The low radiances at 313 nm are caused by the stratospheric ozone absorption, which is negligible at longer wavelengths.

For observations with extended FOV, the effective AMF results from the spatial averaging of the AMF weighted by the radiance. In that way the increased (decreased) radiance above scattering (absorbing) aerosols further increases (decreases) the AMFs for scattering (absorbing) aerosols. As a consequence, aerosols can have a rather strong impact on the effective AMF compared to the scenarios without aerosols.

In Fig. 12 the retrieved ratios of the plume ~~amount-content~~ (ratio of the retrieved number of trace gas molecules assuming a 1D AMF and the true number of trace gas molecules in the plume) for TROPOMI observations are shown for aerosol scenarios (for a 1 x 1 x 1 km<sup>3</sup> plume). Compared to the results for the aerosol-free cases the results are higher (for scattering aerosols) or lower (for absorbing aerosols). The strongest differences are found for IO at 440 nm, because the relative effect of the aerosols compared to Rayleigh scattering increases towards longer wavelengths. For scattering aerosols, the true plume amount-content can even be overestimated ~~caused-by~~due to the light path enhancement ~~due-to~~from increased multiple scattering in the plume as well as more backscattered light from the plume (higher reflectance above the plume). Very similar to the scenarios without aerosols, the ratios of the maximum SCDs of the neighboring pixels to the SCDs of the center pixels- range from 2 % to 9%.

### 4 Saturation effect

470 For strong atmospheric absorbers like SO<sub>2</sub>, the exact plume extent becomes especially important. If the same amount of  
molecules is confined in a small or large volume (depending on the dilution state of the plume), the corresponding VCDs and  
vertical optical depths vary. For narrow horizontal plume extensions (e.g. in fresh plumes before effective mixing with  
ambient air) the optical depth is higher than for more diluted plumes (Fig. 2b). This effect is illustrated in Fig. 13 for SO<sub>2</sub>  
475 observations at a wavelength of 313 nm (representative for the standard SO<sub>2</sub> fit range, see Fig. 64) and a plume height of 5 –  
6 km. Results for other plume heights are shown in Fig. A3.4 in appendix A3. In the left part of the figure the spatial  
distributions of the SO<sub>2</sub> VCDs are shown for the scenarios with SO<sub>2</sub> as weak absorber (top), ,strong,1' (middle), and  
,strong,4' (bottom), see table 3. The different colours indicate the different horizontal extensions of the plume (with the total  
amount of molecules kept constant). In the center and right part of the figure, plume scans of the AMF and the backscattered  
480 normalised radiance are shown. As expected, for the scenario with SO<sub>2</sub> as weak absorber even for the smallest horizontal  
plume extension (1 x 1 km<sup>2</sup>) the radiance above the plume is the same as outside the plume (top, right). The decrease of the  
AMF compared to the 1D-AMF is thus simply a result of the light mixing effect (section 3). For higher SO<sub>2</sub> concentrations,  
however (middle and bottom panel), the radiance is systematically reduced above the plume (like for the scenario with  
strong aerosol absorption, see Fig. 11 bottom), because a substantial fraction of the photons is absorbed by SO<sub>2</sub>. Here it is  
interesting to note that even for the highest SO<sub>2</sub> concentrations the radiance does not approach zero indicating that part of the  
485 light is backscattered from molecules above the volcanic plume (while almost all photons reaching the volcanic plume are  
probably absorbed by SO<sub>2</sub>). Accordingly, with increasing plume height a stronger reduction of the observed radiance for  
plumes with high SO<sub>2</sub> amounts is found (see Fig. A3.4 in the appendix A3). For the scenarios with high SO<sub>2</sub> amounts, also  
the AMFs above the plume are systematically reduced compared to the scenarios with weak SO<sub>2</sub> absorption, because the SO<sub>2</sub>  
absorption is so strong that the observed photons have only ,seen' part of the vertical plume extension (similar to the  
490 scenario with strong aerosol absorption, see Fig. 11 bottom). The combined effects of reduced backscattered radiance and  
reduced AMFs strongly reduces the effective AMFs, when averaged over a satellite ground pixel. The reduction of the AMF  
is largest for the narrow plumes.

#### 4.1 SO<sub>2</sub> results for TROPOMI observations for different plume contents and wavelengths

495 Fig. 14 shows the fraction of the retrieved plume ~~molecules~~ content for a plume at 5 – 6 km altitude as function of the plume  
size derived from TROPOMI observations if a 1D-AMF is assumed in the analysis. In addition, the retrieved SO<sub>2</sub> SCDs are  
shown. Similar results for other plume altitudes are shown in Fig. A.3.5 in appendix A3. The simulations are performed for  
the 4 scenarios with strong SO<sub>2</sub> absorption (see table 3) and 4 wavelengths (313.1 nm, 324.15 nm, 332.0 nm, 370.3 nm, see  
500 table 4 and Fig. 64). From the results in Fig. 14 and Fig. A3.5 several conclusions can be drawn:

- a) a systematic and strong underestimation for short wavelengths is found (in addition to the light mixing effect). This  
additional underestimation is caused by the strong SO<sub>2</sub> absorption for narrow plumes and is referred to in this study as  
saturation effect. The underestimation caused by the saturation effect is similar for the different plume heights.
- b) in spite of the strong SO<sub>2</sub> absorption, in some cases, the retrieved SO<sub>2</sub> SCDs are below the threshold value (red horizontal  
505 line), above which the operational SO<sub>2</sub> retrieval switches to the alternative fit windows (at longer wavelengths). The  
threshold values are  $4 \cdot 10^{17}$  molec/cm<sup>2</sup> for the switch from fit range 1 to 2 and  $6.7 \cdot 10^{18}$  molec/cm<sup>2</sup> for the switch from fit  
range 2 to 3, see Theys et al. (2021b). This is an important finding, because in such cases no analyses in the alternative fit  
windows will be performed and such high SO<sub>2</sub> amounts stay undetected in the current TROPOMI SO<sub>2</sub> retrieval. In contrast  
to the underestimation caused by the saturation effect the retrieved trace gas SCDs depend strongly on the plume altitude.
- c) To retrieve the correct SO<sub>2</sub> SCD (and to avoid the saturation effect), it is recommended that simultaneous analyses in  
510 different wavelength ranges are performed. If the SCDs at shorter wavelengths are found to be systematically smaller than  
those at longer wavelengths, the results of the retrievals at the longer wavelengths should be considered. Only if in the

standard fit window similar SCDs are obtained as at longer wavelengths, the results from the standard fit window should be used. This procedure would avoid that high SO<sub>2</sub> amounts stay undetected. Specific thresholds for the differences of the results in the different fit windows should be defined in a dedicated and more detailed study taking also into account the increasing detection limits towards longer wavelengths.

#### 4.2 SO<sub>2</sub> results for observations from different satellites

Fig. 15 presents an overview on the fraction of the retrieved SO<sub>2</sub> amounts–content of the plume by different satellite instruments for scenarios with strong absorptions (see table 3) for a 1 x 1 x 1 km<sup>3</sup> plume at 5 – 6 km altitude. Similar results for other plume altitudes are shown in Fig. A3.6 in appendix A3. For all SO<sub>2</sub> scenarios a strong dependence of the retrieved SO<sub>2</sub> SCD (and the retrieved fraction of the retrieved–plume moleculescontent) is found. The wavelength above which the underestimation becomes negligible depends on the SO<sub>2</sub> scenario (see table 3). For high SO<sub>2</sub> amounts, only analyses at long wavelengths yield reasonable results (but are of course still affected by the light mixing effect). Interestingly, the saturation effect is similar for the different instruments (with different ground pixels sizes), indicating that the saturation effect is mainly determined by the plume properties. Overall, similar results for the different plume heights are found, but for plumes at high altitudes a difference is found for the longer wavelengths compared to plumes at lower altitudes: there the retrieved fraction of the plume content increases especially for the instruments with small pixel sizes (TROPOMI and OMI), because the light mixing effect becomes less efficient with increasing altitude due to the reduced probability of multiple Rayleigh scattering.

#### 4.3 Effect of the wavelength dependence of the AMF

So far the simulations were performed at single wavelengths in order to save computation time. These wavelengths were chosen to represent the dominant differential absorption cross sections for the different SO<sub>2</sub> fit windows (see Fig. 6-4 and table A2A2.1). While these monochromatic simulations can give a good first indication of the saturation effect, they neglect the effect of the wavelength dependence of the AMF (Marquard et al., 2000; Puķīte et al., 2010, 2016). This wavelength dependence is mainly caused by the wavelength dependence of the SO<sub>2</sub> absorption cross section, because for increasing absorption cross sections the penetration depth of the backscattered photons (and hence the AMF) decreases: the AMF is smallest for the highest values of the cross sections, and the wavelength-dependence of the AMF leads to a further decrease of the differential optical depth:

$$\tau(\lambda) = VCD \cdot AMF(\lambda, \sigma(\lambda)) \cdot \sigma(\lambda) \quad (2)$$

Note that an additional wavelength dependency of the AMF due to Rayleigh scattering is less important for the rather small fit windows considered here. We quantify the effect of the wavelength dependence of the AMF as described in appendix A2A4.

It is found that the effect of the wavelength dependence of the AMF is small for cases with small optical depths. For cases with high optical depths and thus strong saturation effects, the true underestimation becomes larger than for the monochromatic AMFs. But such cases can be easily identified by the comparison of the retrieved SO<sub>2</sub> SCDs from different spectral ranges. For the SO<sub>2</sub> analysis, then an appropriate spectral range (with negligible saturation effect) has to be selected. For such analyses, also the effect of the wavelength dependence of the AMF becomes negligible.

## 555 | 5 Geometric effects for elevated plumes

The simulations presented so far were carried out for scenarios with overhead sun ( $SZA = 0$ ) and nadir-looking instruments (viewing zenith angle,  $VZA = 0$ ). These scenarios were chosen to investigate the light mixing and saturation effects in a fundamental way. In typical measurement situations, however, the illumination and viewing directions deviate from the vertical axes. Especially for elevated plumes, the trace gas absorption will then not be seen for the ground pixel exactly below the plume (Fig. 2c). In extreme cases, even double plumes might be observed. These effects of slant illumination and viewing angles are referred to as geometric effects in this study and are investigated in this section. Geometric effects lead to an increase of the horizontal extension over which the plume signal is seen compared to the observation geometry with  $SZA = VZA = 0$ . But at the same time, also the magnitude of the absorption is decreased, and might effectively fall below the detection limit. This reduction of the absorption is simply caused by the fact that for such cases ~~with  $SZA \neq VZA$~~  the atmospheric light paths cross the plume only once (or less) for a given viewing angle.

In Fig. 16 the AMFs for plume scans for observations of elevated plumes with various combinations of  $SZA$  and  $VZA$  are shown. The blue lines show the AMFs for observations with a narrow FOV (right y axis); the bright blue horizontal bars represent simulations for a TROPOMI FOV (3.5 km in across track dimension, left axis). Note that we kept the ground pixel size constant (3.5 x 5.5. km<sup>2</sup>) for all viewing angles in order to study the basic effects in a systematic way. For real TROPOMI observations, the ground pixel sizes increase for slant viewing angles. The TROPOMI AMFs are systematically lower than the AMFs for the narrow FOV, because the plume covers only a small fraction of the TROPOMI ground pixel (for nadir view ~5%).

The simulations shown in Fig. 16 are performed for 440 nm (IO). Similar results, but with less clear peaks, are obtained for the other wavelengths (for  $SO_2$  at 313 nm and BrO at 340 nm see Fig. A5.1 and A5.2 in appendix A3A5). In addition to the AMFs, also sketches of the corresponding observation geometries are shown above the sub figures. As expected, the plume signals seen by the satellite are usually not found for those ground pixels covering the plume. Instead, maxima of the AMF are found for the downward and upward light paths crossing the plume, but slightly enhanced values are also found in between these maxima. They are caused by sunlight which has crossed the plume and is then scattered towards the instrument before it reached the ground. As a general finding, the apparent horizontal extent of the plume increases for observations with slant illumination and/or slant viewing angles compared to observations with  $SZA = VZA = 0$ . At the same time the magnitude of the AMF decreases for observations with slant illumination and/or slant viewing angles. Both aspects have a direct influence on the ~~detected-retrieved~~ total fraction of the plume ~~amount-content~~: on the one hand, the ‘smearing’ of the plume signal can lead to a larger number of ground pixels with enhanced absorptions and thus to a larger total covered area. On the other hand, ground pixels with weak absorptions (e.g. between the two AMF maxima) might fall below the detection limit (especially for scenarios with low trace gas VCDs). Both dependencies are seen in Fig. 17 where the number of pixels above the detection limit and the ~~detected-retrieved~~ total fraction of the plume ~~amount-content~~ for TROPOMI observations with various viewing and illumination angles are shown for different scenarios of weak absorbers (see table 3). For the different trace gases, different numbers of pixels with SCDs above the detection limit are found. The largest numbers are found for IO at 440 nm (weakest probability of Rayleigh scattering) and slant viewing and illumination angles (with opposite direction, relative azimuth angle,  $RAA = 0^\circ$ ), for which the apparent spatial extent of the plume gets largest. Interestingly, the ~~detected-retrieved~~ fraction of the plume ~~amount-content~~ is similar for all viewing geometries.

## 595 | 6 Plume side effects for low plumes

For slant illumination and viewing angles, interactions of photons with the sides of the plumes can become important, especially for plumes containing aerosols. However, even for plumes free of aerosols, photons entering or leaving the plumes

from the sides have 'seen' different trace gas absorptions compared to the 1D scenarios. In this section plume side effects are investigated for TROPOMI observations and for a narrow plume ( $1 \times 1 \times 1 \text{ km}^3$ ) located directly above the surface. We chose this low plume altitude, because for such plumes the side scattering effect can be investigated without interference with the geometric effects (section 5). Of course, the side scattering effect also affects plumes at higher altitudes (in addition to geometric effects). The aerosol scenarios are similar as in section 2.2 with an AOD of 10 and a single scattering albedo of 1.0 (purely scattering aerosols) or 0.8 (strongly absorbing aerosols). ~~Note that plume side effects play also a role for the scenarios in the previous section on geometric effects. But there the focus was on the horizontal smearing and apparent displacement of elevated plumes.~~

In the middle panels of Fig. 18a,b the AMFs and normalised radiances for plume scans with a narrow FOV ( $0.014^\circ$ ) for (a) IO at 440 nm and (b) SO<sub>2</sub> at 313 nm are shown (blue symbols). The simulations are performed for a slant viewing angle (VZA =  $60^\circ$ ) and selected SZAs ( $0^\circ$  and  ~~$6050^\circ$~~  in forward and backward direction). The plumes of  $1 \times 1 \times 1 \text{ km}^3$  are located at the surface (red boxes) and contain the trace gas and scattering aerosols with an AOD of 10. In addition to the AMFs for the narrow FOV, also AMFs for a TROPOMI FOV (3.5 km in across track direction) are shown (horizontal magenta bars). Especially for IO at 440 nm the normalised radiances and AMFs for the narrow FOV show complex dependencies on the viewing angle. Moreover, while the enhanced values of the radiances and the AMFs are found at similar viewing angles, there are also systematic differences in the details of their viewing angle dependencies. These are caused by the different sensitivities of both quantities on the atmospheric light paths. While the radiance mainly depends on the probability of scattering (on molecules and aerosols), the AMF also strongly depends on the length of the light path through the trace gas plume. These dependencies can be e.g. seen in the upper left part of Fig. 18a, where the maximum of the radiance is found at about 1.5 km, while the maximum AMF is found at a distance of about 0.8 km from the plume center. Also clear differences for forward and backward illumination are found. The stronger and more structured signals for IO at 440 nm are caused by the fact that the direct sun light can penetrate ~~more-deepdeeper~~ into the atmosphere than at shorter wavelengths and thus geometric effects (like shadowing for a VZA of  $60^\circ$  and a SZA of  $-50^\circ$ ) are more clearly visible. Also the AMFs for the TROPOMI FOV differ systematically for different illumination directions. The TROPOMI AMFs (for ground pixels covering the plume) as function of the SZA and for different aerosol scenarios) are shown in the bottom panels of Fig. 18 (also for a VZA of  $60^\circ$ ). Besides the 3D-AMFs also the corresponding 1D-AMF (without aerosols) are presented. A clear dependence on the SZA is found for all AMFs, which is slightly asymmetric (for forward and backward illumination) for the non-nadir viewing direction (VZA =  $60^\circ$ ). These dependencies are caused by two effects: first by the angular dependence of Rayleigh scattering which is relevant for both the 1D and 3D simulations; second by the angular dependence of Rayleigh scattering and aerosol scattering (if aerosols are present) for the 3D plumes).

Fig. 19 shows the ~~detected-retrieved~~ fraction of the plume ~~amount-content~~ for the different 3D cases if the corresponding 1D-AMF is applied in the data analysis (similar to Fig. 12). For SO<sub>2</sub> at 313 nm and BrO at 340 nm only weak dependencies on the SZA are found indicating that at these short wavelengths the direct sun light does not penetrate deep into the atmosphere (because of the high probability of Rayleigh scattering). Also only a weak dependence on the viewing angle is found. The low AMFs for the VZA of  $60^\circ$  are related to the fact that for such slant angles the FOV for a 3.5 km wide ground pixel is rather small, and not the whole vertical extent of the  $1 \times 1 \times 1 \text{ km}^3$  plume falls within the FOV.

In contrast to 313 nm and 340 nm, for IO at 440 nm systematic dependencies of the retrieved fraction of the plume content on the SZA are found, indicating the increased penetration depth of the direct sun light. For plumes without aerosols, almost constant ~~ratios-values~~ are found for SZA <  $70^\circ$ , while for SZA  $\geq 70^\circ$  the ~~ratios-values~~ strongly decrease. For observations of 3D plumes under such slant illumination angles part of the direct sun light has not crossed the plume (like for the 1D scenario) before it is reflected / scattered towards the instrument. For the scenario with scattering aerosols, the retrieved fraction of the plume content ratios-are-is always > 1 indicating the effect of multiple scattering (together with the increased radiance from the plume providing more weight for the trace gas signal from the plume). The ~~ratios-values~~ systematically

increase with increasing SZA (except for the highest SZA). This increase is related to the higher contribution of photons entering the plume from the sides (pronounced forward scattering). For the non-nadir observations (VZA  $\neq$  0) also a slight asymmetric dependence on the SZA is found.

645 For the scenario with absorbing aerosols, low ~~ratios-values~~ and almost no SZA-dependence are found for all wavelengths indicating that the aerosol absorption prevents the penetration of the solar photons deep into the volcanic plume (together with the reduced radiance from the plume). In summary, as already shown in section 3.3, the 3D-AMFs (and thus the retrieved fraction of the plume content) for plumes with scattering aerosols can be strongly increased compared to aerosol-free plumes. This overestimation is strongest for long wavelengths. In such cases the satellite measurements strongly overestimate the ~~amount-true plume content-of plume molecules~~ if a 1D AMF is applied up to >100% towards high SZA and high VZA (note that the largest VZAs for such observations are about 66° as for example for TROPOMI). Interestingly, the retrieved fraction of the plume content ratio-of-the 3D-AMF for scattering aerosols versus the 1D-AMF (without aerosols)-at 313 nm is close to unity regardless of the geometry. For SO<sub>2</sub>-measurements of such plumes in the standard fit range, the application of 1D-AMFs will thus lead to rather small errors.

655 For observations of plumes without aerosols or with absorbing aerosols the satellite measurements strongly underestimate the ~~amount-number~~ of plume molecules if a 1D AMF (without aerosols) is applied in the data analysis (in agreement with the results shown in section 3.3).

## 7 Ground based measurements

660 3D effects are not only important for satellite observations of volcanic plumes, but also for ground based observations. In this section we briefly deal with this topic but only discuss the light mixing effect for ground based observations, because it is the most fundamental 3D radiative transfer effect. Kern et al. (2010) investigated 3D effects for ground based observations of volcanic plumes. Their focus was on the effect of sun light scattered into the line of sight between-of the instrument and without having crossed the volcanic plume before, is referred to as light dilution effect (see also Millán, 1980). The light dilution effect is usually the dominant effect for such observations. While the exchange of light between the plume and outside the plume by multiple scattered photon was also included in their simulations, its contribution to the 3D radiative effects was not explicitly discussed.

In our simulations for ground based observations we therefore consider two scenarios (see Fig. 20):

670 a) ground based observations for zenith direction and very small SZA (here 0.3°): In this scenario the single-scattered light must have crossed the narrow plume before it is scattered into the instrument (like for the satellite observations with SZA = VZA = 0, see section 3). Thus no direct sun light is scattered into the line of sight of the instrument without having crossed the plume before. These results can be directly compared to the results for satellite observations.

b) ground based observations for zenith direction and slightly larger SZA (here 10°): In this scenario the single-scattered light has not crossed the narrow plume before it is scattered into the instrument (like for scenarios in Kern et al., 2010).

675 Note that for both scenarios single scattered light can also be scattered above the plume into the line of sight of the instrument, but these light paths do not fall under the definition of the light dilution effect.

The results for both scenarios are shown in Fig. 21. For the first scenario, like for the satellite observations (Fig. 5), the strongest dependence is found for 313 nm, because the probability of Rayleigh scattering is largest for the short wavelengths. But the altitude dependence is opposite to that for the satellite observations. Here it is interesting to note that for the AMF ratio between narrow and horizontally extended plumes, no monotonous altitude dependence is found. This is caused by the non-monotonous altitude dependence of the 1D AMFs for horizontally extended plumes. Interestingly, the highest 1D AMFs are found for plumes at medium altitudes (here altitudes of 5 and 10 km). For plumes at lower altitudes, the effect of



multiply scattered photons is reduced because of the low surface albedo. For higher altitudes, it is reduced because of the low probability of Rayleigh scattering with decreasing air density.

685 The results for the second scenario show even lower AMFs for the narrow plumes than those for the first scenario. This is caused by the direct sun light scattered into the line of sight without having crossed the plume before (similar as for the scenarios in Kern et al., 2010). However, a direct comparison of the results of Kern et al. (2010) to the results of this study is complicated, because of two reasons: first, Kern et al. (2010) assumed a plume with infinite extension in one horizontal direction, while we assumed confined plumes in all dimensions. Second, they compared the AMFs of their 3D radiative transfer simulations with the assumption of a geometric light path through the plume, while in our study we compare the 3D AMFs with the corresponding 1D AMFs for horizontally extended plumes. Despite these differences, the general dependencies of the results of Kern et al. (2010) and our results are very similar: They referred to this effect as light dilution effect. Their simulations were performed with the same radiative transfer model TRACY-2 as used in this study. As a general set up they assumed a plume with a vertical extension of 500 m and a horizontal extension of 600 m located at different altitudes. The instrument was directed to the plume either in slant or vertical direction. The SZA was always 30°. Kern et al. (2010) found that the AMF can be strongly reduced by the light dilution<sup>3D</sup> effects. While for plumes in close proximity to the ground, directly above the surface, the AMF was is similar to the geometric AMF (but smaller than the corresponding 1D-AMF), it strongly decreased~~decreases~~ with increasing plume altitude (or horizontal distance between instrument and plume).

700 In this section we perform similar simulations, but we vary also the horizontal plume extent and the SZA (see Fig. 20). Like for the satellite observations (Fig. 4), a strong and systematic dependence of the AMFs on the horizontal plume extension is found. These results indicate that usually for ground based observations not only the dilution effect (as described in Kern et al. (2010)) but also the light mixing effect is important.

705 This becomes particularly obvious for the simulation results for SZA = 0° (Fig. 20 top). In these cases (in contrast to the scenarios in Kern et al. (2010)) no direct sun light is scattered into the line of sight between the plume and the instrument, but still a systematic dependence of the AMFs on the horizontal plume extent is found. Like for satellite observations, the strongest dependence of the AMF is found for 313 nm, because the probability of Rayleigh scattering is largest for the short wavelengths. But the altitude dependence is opposite to that for the satellite observations.

710 When comparing the results for SZA = 0° and SZA = 10°, an interesting difference is found for narrow elevated plumes. For 10° SZA, direct sunlight can reach the line of sight of the instrument below the plume without having traversed the plume (dilution effect as in Kern et al., 2010) leading to much smaller AMFs than for the simulations with exact overhead sun (SZA = 0°). Except for these narrow elevated plumes, the results for both SZAs are almost identical indicating that the light mixing effect occurs independently from whether the direct sun light is scattered into the line of sight with or without having crossed the plume before. Or in other words, the light mixing effect is the more fundamental effect, and the dilution effect (if the direct sun light has not crossed the plume before) can further strongly decrease the AMF.

715 The results of this study also indicate that the correction factors presented by Kern et al. (2010) are only valid for the chosen plume size (vertical extent of 500 m, horizontal extent ~~of in one dimension:~~ 600 m, and infinite in the other dimension). However, aAn assumed change of the plume extent from 200 m to 4 km changes the AMFs by about 5 % (for 440 nm) and 30 % (for 313 nm). The dependence of the AMFs on the horizontal plume extent is probably smaller for more realistic plumes (like those in Kern et al., 2010). Nevertheless, Thus for future analyses of ground based observations, the plume size should be also taken into account. It should be noted that our simulations cover only a limited set of scenarios (zenith view, small SZA, no aerosols, no strong SO<sub>2</sub> absorptions). While our results are useful to illustrate the general influence of the light mixing effect and dilution effect on ground based observations, they are not representative for all measurement situations. Simulations for a more comprehensive set of scenarios (including more realistic plumes) and covering also the other 3D effects should be performed in future studies.

## 8 Conclusions

730 In this study different 3D effects were investigated with a focus on satellite observations. The new TROPOMI instrument aboard Sentinel-5P has a much smaller ground pixel size (down to 3.5 x 5.5 km<sup>2</sup>) than previous sensors. Thus TROPOMI can detect small volcanic plumes, which were invisible for ~~the precursor~~ ~~previous~~ instruments. However, for observations with small ground pixels, 3D effects become important, which were of minor importance for the observations with larger ground pixels.

735 We investigated the following four 3D effects: the light mixing effect caused by horizontal photon paths, the saturation effect caused by strong SO<sub>2</sub> absorption, geometric effects related to slant illumination and viewing angles, and side-scattering effects related to photons originating from the sides of volcanic plumes.

Especially the first two effects can lead to a strong and systematic underestimation of the true trace gas content of the plume if 1D assumptions are used in the data analysis (up to more than 50% for the light mixing effect, and up to 100% for the saturation effect).

740 Thus for TROPOMI analyses of small volcanic plumes the light mixing effect has to be considered if the volcanic plume covers only 1 satellite ground pixel (or a small number of ground pixels with a clear maximum for a single ground pixel or in general if strong gradients on spatial scales of the TROPOMI ground pixel size are present). In such cases, wavelength-dependent correction factors (according to the results in Fig. 10) have to be applied to the results if a 1D AMF is used. The strongest underestimation (>50%) caused by the light mixing effect occurs for observations at short wavelengths and plumes below 10 km.

745 The saturation effect can lead to a further strong underestimation of the analysis results for cases with strong SO<sub>2</sub> absorptions. The strongest saturation effect occurs for observations at short wavelengths and for narrow plumes with high SO<sub>2</sub> VCDs (e.g. about > 95% underestimation for observations at 313 nm of a 1 x 1 x 1 km<sup>3</sup> plume with SO<sub>2</sub> VCDs > 2.5 · 10<sup>19</sup> molec/cm<sup>2</sup>). In extreme cases, in spite of the strong SO<sub>2</sub> absorption, the SO<sub>2</sub> SCDs retrieved in the standard fit window might even stay below the threshold for the switch of fit windows, and such plumes might remain undetected. For future analyses (not only for TROPOMI, but also for other sensors) we recommend to always retrieve SO<sub>2</sub> SCDs simultaneously in different fit windows. If the SCDs retrieved at short wavelengths (standard analysis) are found to be systematically smaller than at the other wavelengths, the SCDs from the alternative fit windows should be used.

750 Geometric effects typically have a weaker influence on the quantitative results, but they can affect the spatial pattern under which elevated plumes are 'seen' by the satellite instrument. Usually, localised elevated plumes are widened and even double peaks can occur. These effects should be kept in mind if complex plume patterns are observed. They might be simply caused by slant viewing and/or illumination angles.

755 Plume side effects are usually small for short wavelengths, but become larger for longer wavelengths. Especially if scattering aerosols are present in volcanic plumes they can lead to a strong overestimation of the true plume content if 1D AMFs (without aerosols) are used. While this overestimation is rather small for nadir observations and overhead sun (between about 5% and 50% depending on wavelength), it can reach much higher values (up to >100%) for slant viewing and illumination angles. Here it is important to note that such effects will probably play a rather important role for future sensors like the upcoming geostationary Sentinel-4 mission (Bazalgette Courrèges-Lacoste et al., 2017) which measures under rather

760 slant viewing and illumination angles at northern latitudes. Also for ground based observations, 3D effects can become important. In addition to the dilution effect (see Kern et al. 2010), which mostly depends on the distance between the ground based instrument and the volcanic plume, also -especially the light mixing effect plays an important role, and a similarly shows a similar strong dependence on the horizontal plume

extension as for satellite observations [is found](#). Thus the horizontal plume extension should also be taken into account for the analysis of ground based observations.

In this study the most fundamental 3D effects were investigated, but some important questions remain open:

a) How representative are the assumed aerosol properties for real volcanic plumes? There is a huge knowledge gap about aerosol properties in volcanic plumes, mainly because especially for absorbing aerosols, the dense volcanic plumes can not be penetrated by optical remote sensing techniques. One option to overcome this difficulty could be [to perform](#) in situ and remote sensing measurements from drones flying into volcanic plumes. At least close to the edge of the plume, the aerosol extinction might be retrieved from direct sun measurements.

b) What is the consequence of 3D effects for the quantification of emission fluxes from real volcanoes? The simulations of this study were made for idealised volcanic plumes. In reality, more complex plume configurations will occur. Thus in particular two scenarios should be investigated: 1) confined or vertical plumes: in many cases (for small plumes) enhanced trace gas absorptions are found only directly above the volcano or close to it. If the horizontal wind speeds are low, also a vertically oriented plume might contribute to the observed trace gas absorption. 2) horizontal plumes: for larger eruptions often elongated plumes are found, which are dominated by horizontal transport. Both scenarios should be simulated and eventually a direct connection between the observed trace gas SCDs and the emission flux from the volcano should be established. Such simulations will be carried out in a follow-up study.

c) How important are 3D effects for other confined trace gas plumes? Confined trace gas plumes also occur for other localised emission sources, in particular power plants. For measurements of the SO<sub>2</sub> emissions from power plants (in the UV spectral range), a similar strong underestimation will occur (up to more than 50%) as for the volcanic plumes. As shown in this study, for NO<sub>2</sub> observations in the blue spectral range the light mixing effect is much smaller than for the UV spectral range. But these results were obtained for a pure Rayleigh atmosphere outside the plume. Since power plant emissions usually occur in polluted regions with high aerosol concentrations, aerosol scattering will enhance the diffuse atmospheric radiation compared to a pure Rayleigh atmosphere, which will possibly increase the light mixing. Also 3D effects for realistic power plant plumes will be addressed in a forthcoming study.

#### Author contributions

TW performed the simulations and [prepared-wrote](#) the manuscript with contributions from all co-authors.

#### Acknowledgements

The study ~~was partly funded by~~ [received funding from](#) BMBF/DLR Bonn (contract no. 50EE1811B). We thank Tjarda Roberts (Université d'Orléans) and Luke Surl (University of Aberdeen) for helpful discussions about volcanic plumes.

#### Competing interests

Thomas Wagner is executive editor of AMT. [Steffen Beirle is AMT associate editor.](#)

#### References

Afe, O. T., Richter, A., Sierk, B., Wittrock, F., and Burrows, J. P.: BrO emissions from volcanoes: a survey using GOME and SCIAMACHY measurements, *Geophys. Res. Lett.*, 31, L24113, <https://doi.org/10.1029/2004GL020994>, 2004.  
Bazalgette Courrèges-Lacoste, G., M. Sallusti, G. Bulsa, G. Bagnasco, Ben Veihelmann, S. Riedl, D. J. Smith, R. Maurer, "The Copernicus Sentinel 4 mission: a geostationary imaging UVN spectrometer for air quality monitoring," *Proc. SPIE*

- 10423, *Sensors, Systems, and Next-Generation Satellites XXI*, 1042307 (29 September 2017); <https://doi.org/10.1117/12.2282158>
- 815 Bobrowski, N., Hönninger, G., Galle, B., Platt, U., Detection of bromine monoxide in a volcanic plume. *Nature* 423, 273–276, 2003.
- Bobrowski, N., U. Platt, SO<sub>2</sub>/BrO ratios studied in five volcanic plumes, *Journal of Volcanology and Geothermal Research*, Volume 166, Issues 3–4, Pages 147–160, 2007.
- Bobrowski, N., Kern, C., Platt, U., Hörmann, C., and Wagner, T.: Novel SO<sub>2</sub> spectral evaluation scheme using the 360–390 nm wavelength range, *Atmos. Meas. Tech.*, 3, 879–891, doi:10.5194/amt-3-879-2010, 2010.
- 820 Bobrowski, N. and Giuffrida, G.: Bromine monoxide / sulphur dioxide ratios in relation to volcanological observations at Mt. Etna 2006–2009, *Solid Earth*, 3, 433–445, <https://doi.org/10.5194/se-3-433-2012>, 2012.
- Bogumil, K., J. Orphal, J. P. Burrows, Temperature dependent absorption cross sections of O<sub>3</sub>, NO<sub>2</sub>, and other atmospheric trace gases measured with the SCIAMACHY spectrometer, *Proc. ERS - Envisat Symposium. Looking down at our Earth in the New Millennium*, Gothenburg 16 - 20 October 2000.
- 825 Bovensmann, H., J. P. Burrows, M. Buchwitz, J. Frerik, S. Noe'l, V. V. Rozanov, K. V. Chance, and A. Goede (1999), SCIAMACHY—Mission objectives and measurement modes, *J. Atmos. Sci.*, 56, 127–150.
- Burrows, J. P., et al. (1999), The Global Ozone Monitoring Experiment (GOME): Mission concept and first scientific results, *J. Atmos. Sci.*, 56, 151–175.
- 830 Callies, J., Corpaccioli, E., Eisinger, M., Hahne, A., and Lefebvre, A.: GOME-2 – MetOp’s second-generation sensor for operational ozone monitoring, *ESA Bull.*, 102, 28–36, 2000.
- Dinger, F., Kleinbek, T., Dörner, S., Bobrowski, N., Platt, U., Wagner, T., Ibarra, M., and Espinoza, E.: SO<sub>2</sub> and BrO emissions of Masaya volcano from 2014 to 2020, *Atmos. Chem. Phys.*, 21, 9367–9404, <https://doi.org/10.5194/acp-21-9367-2021>, 2021.
- 835 Eisinger, M. and Burrows, J. P.: Tropospheric sulfur dioxide observed by the ERS-2 GOME instrument, *Geophys. Res. Lett.*, 25, 4177–4180, 1998.
- Fioletov, V. E., McLinden, C. A., Krotkov, N., Li, C., Joiner, J., Theys, N., Carn, S., and Moran, M. D.: A global catalogue of large SO<sub>2</sub> sources and emissions derived from the Ozone Monitoring Instrument, *Atmos. Chem. Phys.*, 16, 11497–11519, <https://doi.org/10.5194/acp-16-11497-2016>, 2016.
- 840 Flynn, L. E., Sefstor, C. J., Larsen, J. C., and Xu, P.: The Ozone Mapping and Profiler Suite, in: *Earth Science Satellite Remote Sensing*, edited by: Qu, J. J., Gao, W., Kafatos, M., Murphy, R. E., and Salomonson, V. V., Springer, Berlin, 279–296, doi:10.1007/978-3-540-37293-6, 2006.
- Heue, K.-P., Brenninkmeijer, C. A. M., Baker, A. K., Rauthe-Schöch, A., Walter, D., Wagner, T., Hörmann, C., Sihler, H., Dix, B., Frieß, U., Platt, U., Martinsson, B. G., van Velthoven, P. F. J., Zahn, A., and Ebinghaus, R.: SO<sub>2</sub> and BrO observation in the plume of the Eyjafjallajökull volcano 2010: CARIBIC and GOME-2 retrievals, *Atmos. Chem. Phys.*, 11, 2973–2989, <https://doi.org/10.5194/acp-11-2973-2011>, 2011.
- 845 Hönninger, G., Referenzspektren reaktiver Halogenverbindungen für DOAS-Messungen, Diploma thesis, Univ. of Heidelberg, Heidelberg, Germany, 1999.
- Hörmann, C., Sihler, H., Bobrowski, N., Beirle, S., Penning de Vries, M., Platt, U., and Wagner, T.: Systematic investigation of bromine monoxide in volcanic plumes from space by using the GOME-2 instrument, *Atmos. Chem. Phys.*, 13, 4749–4781, <https://doi.org/10.5194/acp-13-4749-2013>, 2013.
- 850 Kern, C., T. Deutschmann, L. Vogel, M. Wöhrbach, T. Wagner and U. Platt, Radiative transfer corrections for accurate spectroscopic measurements of volcanic gas emissions. *Bull Volcanol* 72, 233–247 (2010). <https://doi.org/10.1007/s00445-009-0313-7>.

- 855 Kern, C., A.H. Lerner, T. Elias, P. Nadeau, P.J. Kelly, C.A. Werner, L.E. Chlor, M. Cappos, Quantifying gas emissions associated with the 2018 rift eruption of Kīlauea Volcano using ground-based DOAS measurements. *Bull. Volcanol.* **82**, 55 (2020).
- Khokhar, M. F., Frankenberg, C., Van Roozendaal, M., Beirle, S., Kühl, S., Richter, A., Platt, U., and Wagner, T.: Satellite Observations of Atmospheric SO<sub>2</sub> from Volcanic Eruptions during the Time Period of 1996 to 2002, *J. Adv. Space Res.*, **36**, 879–887, <https://doi.org/10.1016/j.asr.2005.04.114>, 2005.
- 860 Krotkov, N. A., Carn, S. A., Krueger, A. J., Bhartia, P. K., and Yang, K.: Band residual difference algorithm for retrieval of SO<sub>2</sub> from the Aura Ozone Monitoring Instrument (OMI), *IEEE T. Geosci. Remote Sens.*, AURA Special Issue, **44**, 1259–1266, <https://doi.org/10.1109/TGRS.2005.861932>, 2006.
- Krueger, A. J.: Sighting of El Chichon sulfur dioxide clouds with the Nimbus 7 total ozone mapping spectrometer, *Science*, **220**, 1377–1379, 1983.
- 865 Levelt, P. F., van den Oord, G. H. J., Dobber, M. R., Malkki, A., Visser, H., de Vries, J., Stammes, P., Lundell, J. O. V., and Saari, H.: The Ozone Monitoring Instrument, *IEEE T. Geosci. Remote*, **44**, 1093–1101, <https://doi.org/10.1109/TGRS.2006.872333>, 2006.
- Li, C., Joiner, J., Krotkov, N. A., and Bhartia, P. K.: A fast and sensitive new satellite SO<sub>2</sub> retrieval algorithm based on principal component analysis: Application to the ozone monitoring instrument, *Geophys. Res. Lett.*, **40**, 6314–6318, <https://doi.org/10.1002/2013GL058134>, 2013.
- 870 Lyapustin, A. and Kaufman, Y., Role of adjacency effect in the remote sensing of aerosol, *J. Geophys. Res. Atmos.*, **106**, 11909–11916, <https://doi.org/10.1029/2000JD900647>, 2001.
- Marquard, L.C., T. Wagner, and U. Platt, Improved Air Mass Factor Concepts for Scattered Radiation Differential Optical Absorption Spectroscopy of Atmospheric Species, *J. Geophys. Res.*, **105**, 1315–1327, 2000 .
- 875 [Millán, M., M., Remote sensing of air pollutants. A study of some atmospheric scattering effects. \*Atmospheric Environment\*, \*\*14\*\*, 1241 – 1253, 1980.](#)
- Nowlan, C. R., Liu, X., Chance, K., Cai, Z., Kurosu, T. P., Lee, C., and Martin, R. V.: Retrievals of sulfur dioxide from the Global Ozone Monitoring Experiment 2 (GOME-2) using an optimal estimation approach: Algorithm and initial validation, *J. Geophys. Res.*, **116**, D18301, <https://doi.org/10.1029/2011JD015808>, 2011.
- 880 Penning de Vries, M. J. M., Dörner, S., Puķīte, J., Hörmann, C., Fromm, M. D., and Wagner, T.: Characterisation of a stratospheric sulfate plume from the Nabro volcano using a combination of passive satellite measurements in nadir and limb geometry, *Atmos. Chem. Phys.*, **14**, 8149–8163, <https://doi.org/10.5194/acp-14-8149-2014>, 2014.
- Puķīte, J., Kühl, S., Deutschmann, T., Platt, U., and Wagner, T.: Extending differential optical absorption spectroscopy for limb measurements in the UV, *Atmos. Meas. Tech.*, **3**, 631–653, <https://doi.org/10.5194/amt-3-631-2010>, 2010.
- 885 Puķīte, J. and Wagner, T.: Quantification and parametrization of non-linearity effects by higher-order sensitivity terms in scattered light differential optical absorption spectroscopy, *Atmos. Meas. Tech.*, **9**, 2147–2177, doi:10.5194/amt-9-2147-2016, 2016.
- Richter, R., A fast atmospheric correction algorithm applied to Landsat TM images, *Remote Sens.*, **11**, 159–166, <https://doi.org/10.1080/01431169008955008>, 1990.
- 890 Rix, M., Valks, P., Hao, N., Loyola, D. G., Schlager, H., Huntrieser, H. H., Flemming, J., Koehler, U., Schumann, U., and Inness, A.: Volcanic SO<sub>2</sub>, BrO and plume height estimations using GOME-2 satellite measurements during the eruption of Eyjafjallajökull in May 2010, *J. Geophys. Res.*, **117**, D00U19, <https://doi.org/10.1029/2011JD016718>, 2012.
- Rothman, L. S., Jacquemart, D., Barbe, A., Benner, D. C., Birk, M., Brown, L. R., Carleer, M. R., Chackerian Jr., C., Chance, K., Coudert, L. H., Dana, V., Devi, V. M., Flaud, J.-M., Gamache, R. R., Goldman, A., Hartmann, J.-M., Jucks, K. W., Maki, A.

- Mandin, G., J.-Y., Massie, S. T., Orphal, J., Perrin, A., Rinsland, C. P., Smith, M. A. H., Tennyson, J., Tolchenov, R. N., Toth, R. A., Vander Auwera, J., Varanasi, P., and Wagner, G.: The HITRAN 2004 molecular spectroscopic database, *J. Quant. Spectrosc. Ra.*, 96, 139–204, 2005.
- 900 Schönhardt, A., Richter, A., Theys, N., and Burrows, J. P.: Space-based observation of volcanic iodine monoxide, *Atmos. Chem. Phys.*, 17, 4857–4870, <https://doi.org/10.5194/acp-17-4857-2017>, 2017.
- Schwaerzel, M., Emde, C., Brunner, D., Morales, R., Wagner, T., Berne, A., Buchmann, B., and Kuhlmann, G.: Three-dimensional radiative transfer effects on airborne and ground-based trace gas remote sensing, *Atmos. Meas. Tech.*, 13, 4277–4293, <https://doi.org/10.5194/amt-13-4277-2020>, 2020.
- 905 Schwaerzel, M., Brunner, D., Jakub, F., Emde, C., Buchmann, B., Berne, A., and Kuhlmann, G.: Impact of 3D radiative transfer on airborne NO<sub>2</sub> imaging remote sensing over cities with buildings, *Atmos. Meas. Tech.*, 14, 6469–6482, <https://doi.org/10.5194/amt-14-6469-2021>, 2021.
- Suleiman, R. M., Chance, K., Liu, X., González Abad, G., Kurosu, T. P., Hendrick, F., and Theys, N.: OMI total bromine monoxide (OMBRO) data product: algorithm, retrieval and measurement comparisons, *Atmos. Meas. Tech.*, 12, 2067–2084, <https://doi.org/10.5194/amt-12-2067-2019>, 2019.
- 910 Theys, N., Van Roozendaal, M., Dils, B., Hendrick, F., Hao, N., and De Mazière, M. (2009), First satellite detection of volcanic bromine monoxide emission after the Kasatochi eruption, *Geophys. Res. Lett.*, 36, L03809, doi:10.1029/2008GL036552.
- Theys, N., De Smedt, I., Van Roozendaal, M., Froidevaux, L., Clarisse, L., and Hendrick, F.: First satellite detection of volcanic OCIO after the eruption of Puyehue-Cordón Caulle, *Geophys. Res. Lett.*, 41, 667–672, doi:10.1002/2013GL058416, 2014.
- 915 Theys, N., De Smedt, I., van Gent, J., Danckaert, T., Wang, T., Hendrick, F., Stavrakou, T., Bauduin, S., Clarisse, L., Li, C., Krotkov, N. A., Yu, H., Van Roozendaal, M.: Sulfur dioxide vertical column DOAS retrievals from the Ozone Monitoring Instrument: Global observations and comparison to ground-based and satellite data, *J. Geophys. Res.-Atmos.*, 120, 2470–2491, <https://doi.org/10.1002/2014JD022657>, 2015.
- 920 Theys, N., De Smedt, I., Yu, H., Danckaert, T., van Gent, J., Hörmann, C., Wagner, T., Hedelt, P., Bauer, H., Romahn, F., Pedernana, M., Loyola, D., and Van Roozendaal, M.: Sulfur dioxide retrievals from TROPOMI onboard Sentinel-5 Precursor: algorithm theoretical basis, *Atmos. Meas. Tech.*, 10, 119–153, <https://doi.org/10.5194/amt-10-119-2017>, 2017.
- Theys, N., Hedelt, P., Smedt, I. De, Lerot, C., Yu, H., Vlietinck, J., Pedernana, M., Arellano, S., Galle, B., Fernandez, D., Barrington, C., Taine, B., Loyola, D., and Van Roozendaal, M.: Global monitoring of volcanic SO<sub>2</sub> degassing from space with unprecedented resolution, *Nature Scientific Reports*, 9, 2643, <https://doi.org/10.1038/s41598-019-39279-y>, 2019.
- 925 Theys, N., Hedelt, P., Smedt, I. De, Lerot, C., Yu, H., Vlietinck, J., Pedernana, M., Arellano, S., Galle, B., Fernandez, D., Barrington, C., Taine, B., Loyola, D., and Van Roozendaal, M.: Global monitoring of volcanic SO<sub>2</sub> degassing from space with unprecedented resolution, *Nature Scientific Reports*, 9, 2643, <https://doi.org/10.1038/s41598-019-39279-y>, 2019.
- 930 Theys, N., Fioletov, V., Li, C., De Smedt, I., Lerot, C., McLinden, C., Krotkov, N., Griffin, D., Clarisse, L., Hedelt, P., Loyola, D., Wagner, T., Kumar, V., Innes, A., Ribas, R., Hendrick, F., Vlietinck, J., Brenot, H., and Van Roozendaal, M.: A sulfur dioxide Covariance-Based Retrieval Algorithm (COBRA): application to TROPOMI reveals new emission sources, *Atmos. Chem. Phys.*, 21, 16727–16744, <https://doi.org/10.5194/acp-21-16727-2021>, 2021a.
- Theys, N., I. De Smedt, C. Lerot, H. Yu, M. Van Roozendaal, S5P/TROPOMI SO<sub>2</sub>ATBD, Doc. No.: S5P-BIRA-L2-ATBD-400E, Issue 2.3.0, <https://sentinels.copernicus.eu/documents/247904/2476257/Sentinel-5P-ATBD-SO2-TROPOMI>, 2021b.
- United States Committee on Extension to the Standard Atmosphere: U.S. Standard Atmosphere, 1976, National Oceanic and Atmospheric Administration, National Aeronautics and Space Administration, United States Air Force, Washington D.C., 1976.

- 940 [Tilstra, L. G., Tuinder, O. N. E., Wang, P., and Stammes, P.: Directionally dependent Lambertian-equivalent reflectivity \(DLER\) of the Earth's surface measured by the GOME-2 satellite instruments, \*Atmos. Meas. Tech.\*, 14, 4219–4238, <https://doi.org/10.5194/amt-14-4219-2021>, 2021.](https://doi.org/10.5194/amt-14-4219-2021)
- Vandaele, A. C., Hermans, C., Simon, P. C., Carleer, M., Colin, R., Fally, S., Mérienne, M.-F., Jenouvrier, A., and Coquart, B.: Measurements of the NO<sub>2</sub> Absorption Cross-section from 42000 cm<sup>-1</sup> to 10000 cm<sup>-1</sup> (238–1000 nm) at 220K and 294 K, *J. Quant. Spectrosc. Ra.*, 59, 171–184, 1997.
- 945 Veefkind, J., Aben, I., McMullan, K., Förster, H., de Vries, J., Otter, G., Claas, J., Eskes, H., de Haan, J., Kleipool, Q., van Weele, M., Hasekamp, O., Hoogeveen, R., Landgraf, J., Snel, R., Tol, P., Ingmann, P., Voors, R., Kruizinga, B., Vink, R., Visser, H., and Levelt, P.: TROPOMI on the ESA Sentinel-5 Precursor: A GMES mission for global observations of the atmospheric composition for climate, air quality and ozone layer applications, *Remote Sens. Environ.*, 120, 70–83, <https://doi.org/10.1016/j.rse.2011.09.027>, 2012.
- 950 Wagner, T., J. P. Burrows, T. Deutschmann, B. Dix, C. von Friedeburg, U. Frieß, F. Hendrick, K.-P. Heue, H. Irie, H. Iwabuchi, Y. Kanaya, J. Keller, C. A. McLinden, H. Oetjen, E. Palazzi, A. Petritoli, U. Platt, O. Postlyakov, J. Pukite, A. Richter, M. van Roozendaal, A. Rozanov, V. Rozanov, R. Sinreich, S. Sanghavi, F. Wittrock, Comparison of Box-Air-Mass-Factors and Radiances for Multiple-Axis Differential Optical Absorption Spectroscopy (MAX-DOAS) Geometries calculated from different UV/visible Radiative Transfer Models, *Atmos. Chem. Phys.*, 7, 1809-1833, 2007.
- 955 Warnach, S., Bromine monoxide in volcanic plumes - A global survey of volcanic plume composition and chemistry derived from Sentinel-5 Precursor/TROPOMI data, PhD thesis, University of Heidelberg, 2022.
- Wilmouth, D. M., Hanisco, T. F., Donahue, N. M., and Anderson, J. G.: Fourier Transform Ultraviolet Spectroscopy of the A 2P<sub>3/2</sub>-X 2P<sub>3/2</sub> Transition of BrO, *J. Phys. Chem. A*, 103, 8935–8945, doi:10.1021/jp991651o, 1999.
- Yang, K., Krotkov, N., Krueger, A., Carn, S., Bhartia, P. K., and Levelt, P.: Retrieval of Large Volcanic SO<sub>2</sub> columns from the Aura Ozone Monitoring Instrument (OMI): Comparisons and Limitations, *J. Geophys. Res.*, 112, D24S43, <https://doi.org/10.1029/2007JD008825>, 2007.
- Yang, K., Liu, X., Bhartia, P., Krotkov, N., Carn, S., Hughes, E., Krueger, A., Spurr, R., and Trahan, S.: Direct retrieval of sulfur dioxide amount and altitude from spaceborne hyperspectral UV measurements: Theory and application, *J. Geophys. Res.*, 115, D00L09, <https://doi.org/10.1029/2010JD013982>, 2010.
- 965 Zhang, Y., Li, C., Krotkov, N. A., Joiner, J., Fioletov, V., and McLinden, C.: Continuation of long-term global SO<sub>2</sub> pollution monitoring from OMI to OMPS, *Atmos. Meas. Tech.*, 10, 1495–1509, <https://doi.org/10.5194/amt-10-1495-2017>, 2017.

970

975

980

985 **Tables**

**Table 1: Ground pixel sizes\* and expected SO<sub>2</sub> SCDs for an SO<sub>2</sub> plume with a horizontal extension smaller than or equal to the size of a TROPOMI pixel and a SO<sub>2</sub> SCD of  $1 \cdot 10^{16}$  molec/cm<sup>2</sup> (close to the detection limit) for a GOME-2 observation.**

Instrument	Pixel size [km x km]	Area [km <sup>2</sup> ]	SO <sub>2</sub> SCD [molec/cm <sup>2</sup> ]	SCD ratio with respect to the GOME-2 SCD
GOME-1 (Burrows et al., 1999)	40 x 320	12800	$2.5 \cdot 10^{15}$	0.25
GOME-2 (Callies et al., 2000)	40 x 80	3200	$1 \cdot 10^{16}$	1
OMPS (Flynn et al., 2006)	50 x 50	2500	$1.28 \cdot 10^{16}$	1.28
SCIAMACHY (Bovensmann et al., 1999)	30 x 60	1800	$1.78 \cdot 10^{16}$	1.78
OMI (Levelt et al., 2006)	13 x 23	299	$1.07 \cdot 10^{17}$	10.7
TROPOMI (Veefkind et al., 2021)	3.5 x 5.5**	19.25	$1.66 \cdot 10^{18}$	166.2

\*for OMI and TROPOMI at nadir

\*\*originally 3.5 x 7 km<sup>2</sup>

**Table 2: Free horizontal light paths (e-folding lengths) for different wavelengths and altitudes considering only Rayleigh scattering.**

Altitude	light path length at 313 nm (km)	light path length at 350 nm (km)	light path length at 440 nm (km)
0-1 km	9	16	30
5-6 km	14	25	47
10-11 km	35	66	122

**Table 3: Plume extensions and corresponding trace gas VCDs and AODs (lowest row) used in this study. For a given scenario the amount of trace gas is assumed to be constant but is distributed over different plume volumes (depending on the horizontal plume extension). The trace gas VCDs of the scenarios with 1 x 1 km<sup>2</sup> horizontal extension is used to identify the corresponding scenario in this study.**

Scenario	Trace gas VCDs for different horizontal plume extension								
	1 km	2 km	4 km	6 km	10 km	14 km	20 km	30 km	40 km
BrO VCD ( $1 \cdot 10^{13}$ molec/cm <sup>2</sup> )	<del>100500</del>	<del>125</del>	<del>31.36.25</del>	<del>13.92.78</del>	<del>15</del>	<del>2.550.54</del>	<del>01.25</del>	<del>0.1456</del>	<del>0.0631</del>
IO VCD ( $1 \cdot 10^{13}$ molec/cm <sup>2</sup> )	500	125	31.3	13.9	5	2.55	1.25	0.56	0.31
IO VCD ( $1 \cdot 10^{13}$ molec/cm <sup>2</sup> )	500	125	31.3	13.9	5	2.55	1.25	0.56	0.31
SO <sub>2</sub> VCD <sub>weak</sub> ( $1 \cdot 10^{17}$ molec/cm <sup>2</sup> )	<del>104</del>	<del>12.5</del>	<del>0.625</del>	<del>0.1428</del>	<del>0.041</del>	<del>0.02051</del>	<del>0.04025</del>	<del>0.004011</del>	<del>0.003006</del>
SO <sub>2</sub> VCD <sub>strong, 1</sub> ( $1 \cdot 10^{17}$ molec/cm <sup>2</sup> )	100	25	6.25	2.78	1	0.51	0.25	0.11	0.06
SO <sub>2</sub> VCD <sub>strong, 2</sub> ( $1 \cdot 10^{17}$ molec/cm <sup>2</sup> )	250	62.5	15.6	6.9	2.5	1.28	0.63	0.28	0.16
SO <sub>2</sub> VCD <sub>strong, 3</sub> ( $1 \cdot 10^{17}$ molec/cm <sup>2</sup> )	1000	250	62.5	27.8	10	5.10	2.50	1.11	0.63
SO <sub>2</sub> VCD <sub>strong, 4</sub> ( $1 \cdot 10^{17}$ molec/cm <sup>2</sup> )	4000	1000	250	111	40	20.4	10	4.44	2.5

Formatiert: Schriftart: 10 Pt.

Formatiert: Schriftart: 10 Pt.

Formatiert: Schriftart: 10 Pt.

Formatiert: Schriftart: 10 Pt.



Aerosol AOD	10	2.5	0.625	0.278	0.1	0.051	0.025	0.011	0.006
-------------	----	-----	-------	-------	-----	-------	-------	-------	-------

1005 **Table 4: SO<sub>2</sub> VCDs (for a 1 x 1 x 1 km<sup>3</sup> plume), chosen wavelengths, total absorption cross sections and corresponding vertical optical depths for the strong SO<sub>2</sub> scenarios (see table 3).**

Wavelength / Absorption cross section	SO <sub>2</sub> VCD <sub>strong, 1</sub> 1·10 <sup>19</sup> molec/cm <sup>2</sup>	SO <sub>2</sub> VCD <sub>strong, 2</sub> 2.5·10 <sup>19</sup> molec/cm <sup>2</sup>	SO <sub>2</sub> VCD <sub>strong, 3</sub> 1·10 <sup>20</sup> molec/cm <sup>2</sup>	SO <sub>2</sub> VCD <sub>strong, 4</sub> 4·10 <sup>20</sup> molec/cm <sup>2</sup>
313.1 nm / 2.45 · 10 <sup>-19</sup> cm <sup>2</sup>	2.45	6.13	24.5	98
324.15 nm / 1.55 · 10 <sup>-20</sup> cm <sup>2</sup>	0.16	0.39	1.55	6.2
332.0 nm / 1 · 10 <sup>-21</sup> cm <sup>2</sup>	0.01	0.025	0.1	0.4
370.3 nm / 6 · 10 <sup>-22</sup> cm <sup>2</sup>	0.006	0.015	0.06	0.24

1010 **Figures**

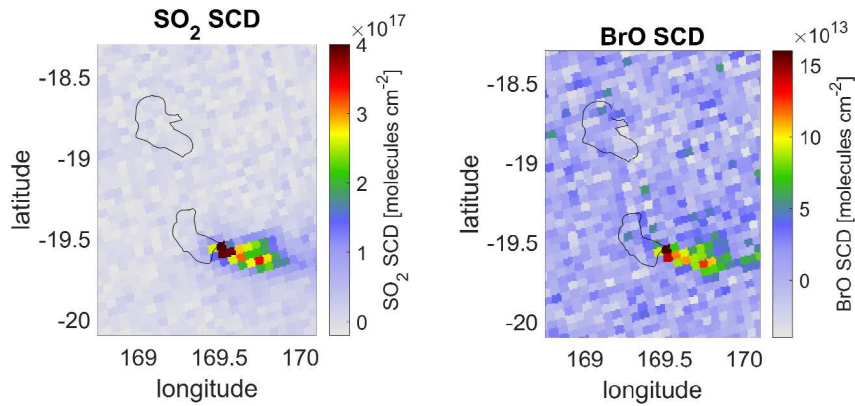


**Fig. 1: TROPOMI observations of the plume of Mount Yasur on 24.06.2020 (Warnach, 2022).**

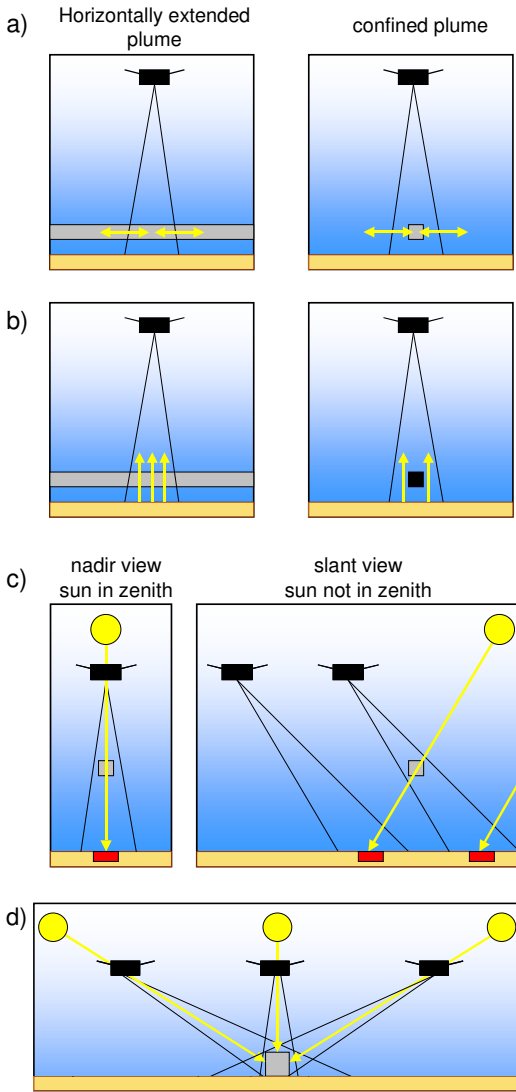
1015

1020

1025

1030

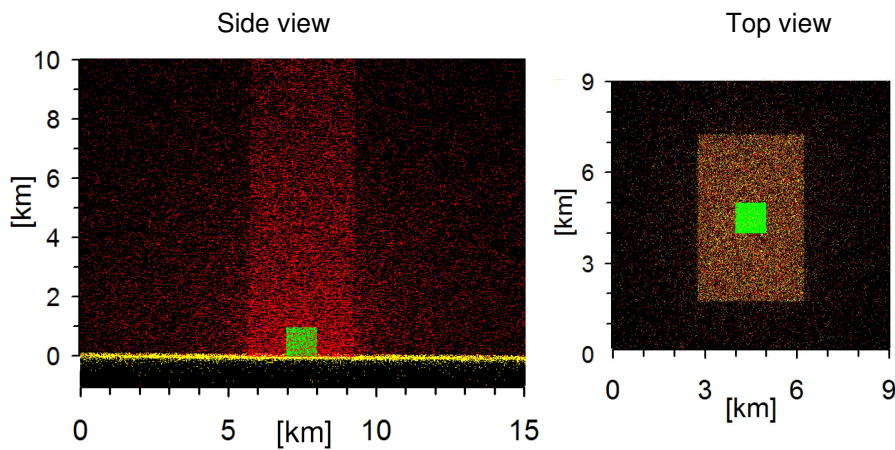
1035



1045

1050

**Fig. 2: The four 3D effects investigated in this study. a) Light mixing effect: part of the light seen by the satellite sensor originates from outside the satellite ground pixel. For horizontally confined plumes (right), such light paths contain no trace gas absorption. b) Saturation effect: for strongly absorbing species like SO<sub>2</sub>, the incoming sun light might be almost fully absorbed in the plume. This can lead to a strong underestimation for narrow plumes with high trace gas concentration. c) geometric effect: depending on the illumination and viewing geometry, the location of the ground pixel with enhanced trace gas absorption (the projection of the plume along the direction of the incoming sun light, red marks at the surface) can systematically differ from the true plume location (grey square). d) Plume side effect: for narrow volcanic plumes the contributions of photons reaching the sensor from the sides of the plume becomes important.**

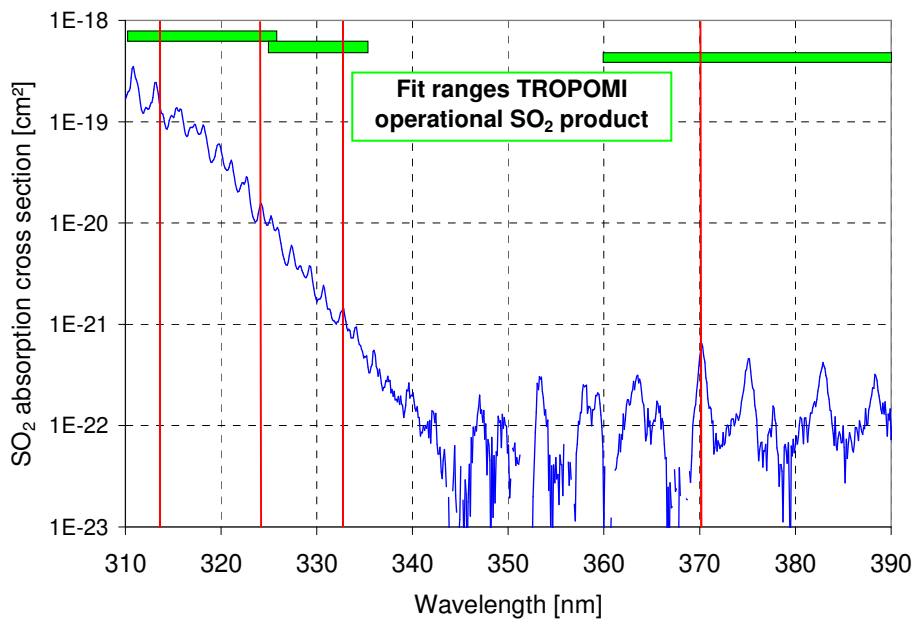


1060

Fig. 3: Exemplary simulation results from the Monte Carlo radiative transfer model TRACY-2. An idealised narrow volcanic plume ( $1 \times 1 \times 1 \text{ km}^3$ ) is observed by TROPOMI with a FOV according to a ground pixel size of  $3.5 \times 5.5 \text{ km}^2$ . Red dots indicate Rayleigh scattering events, **blue dots rotational Raman scattering events**, yellow dots surface reflections, and green dots aerosol scattering events (the volcanic plume is filled with purely scattering aerosols).

1065

Simulations are performed for 340 nm with 25000 photons for overhead sun and a nadir-looking satellite instrument.



1070

Fig. 4 SO<sub>2</sub> absorption cross section (273K, Bogumil et al., 2000, see also <https://www.iup.uni-remen.de/gruppen/molspec/databases/sciamachydata/index.html>). The green bars indicate different SO<sub>2</sub> fit ranges used in the operational TROPOMI product. The vertical bars indicate wavelengths used in the 3D RTM simulations.

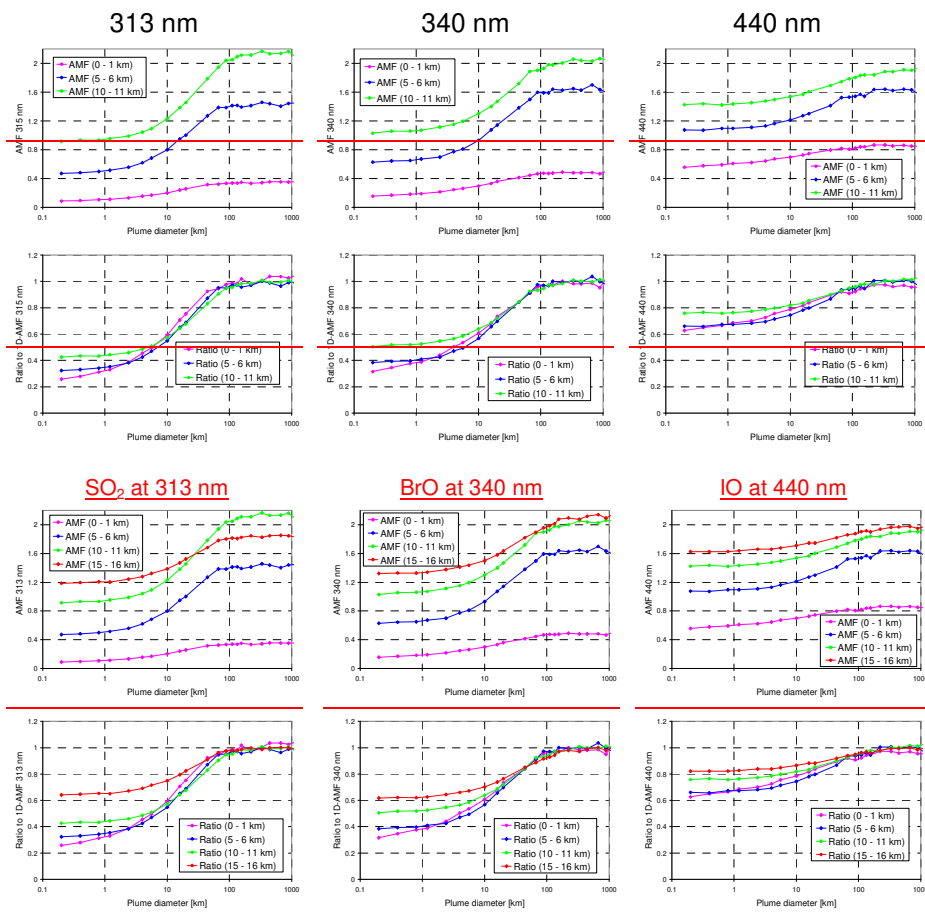


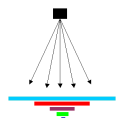
**Fig. 45:** Dependence of the AMF on the horizontal plume extension. Top: AMFs for different plume altitudes and wavelengths; bottom: AMFs normalised by the corresponding 1D AMFs (assuming a horizontally extended plume). The simulations are performed for SZA: 0°, VZA: 0°, FOV: 0.014°, satellite altitude: 824 km asl, no aerosols.

1080

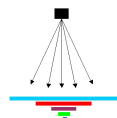
1085

1090

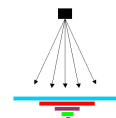
SO<sub>2</sub> at 313 nm



BrO at 340 nm



IO at 440 nm



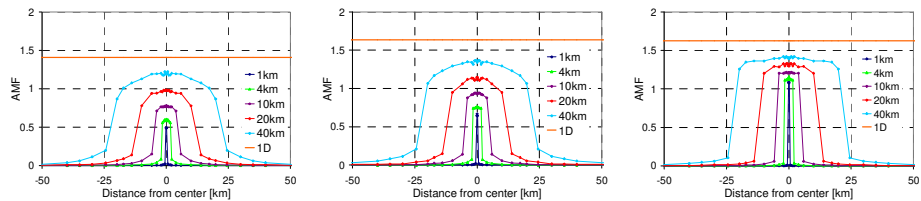
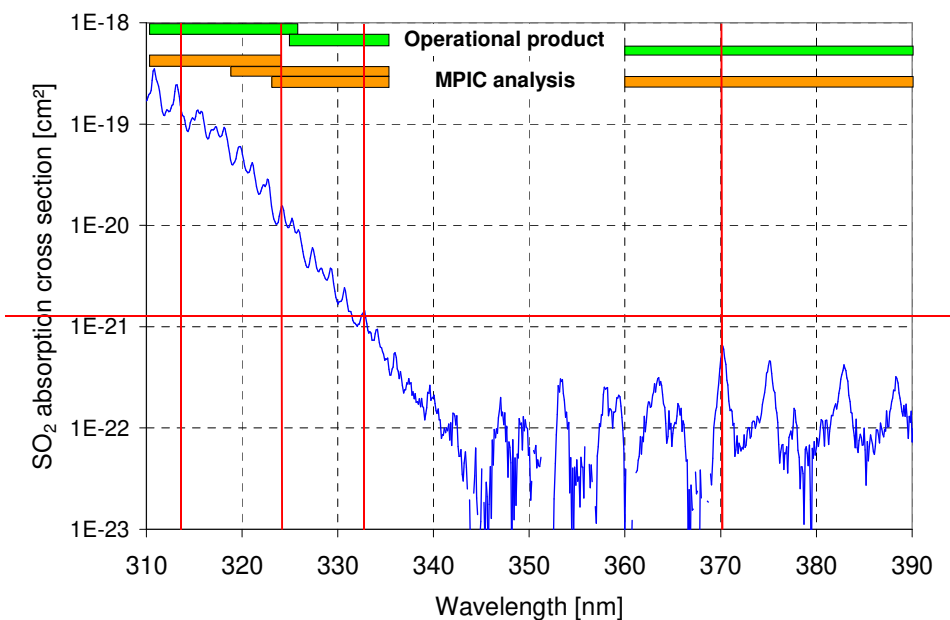


**Fig. 5-6** AMFs for plume scans in near-nadir viewing geometry ( $SZA=0^\circ$ ,  $VZA=0^\circ$ ) at different wavelengths. It is assumed that the satellite scans the plume with a narrow FOV ( $\sim 0.014^\circ$ ). The different colours represent AMFs for plumes at 5-6 km altitude and with different horizontal extensions (from  $1 \times 1 \text{ km}^2$  to  $40 \times 40 \text{ km}^2$ ). Results for other plume altitudes are shown in appendix A3.

1095

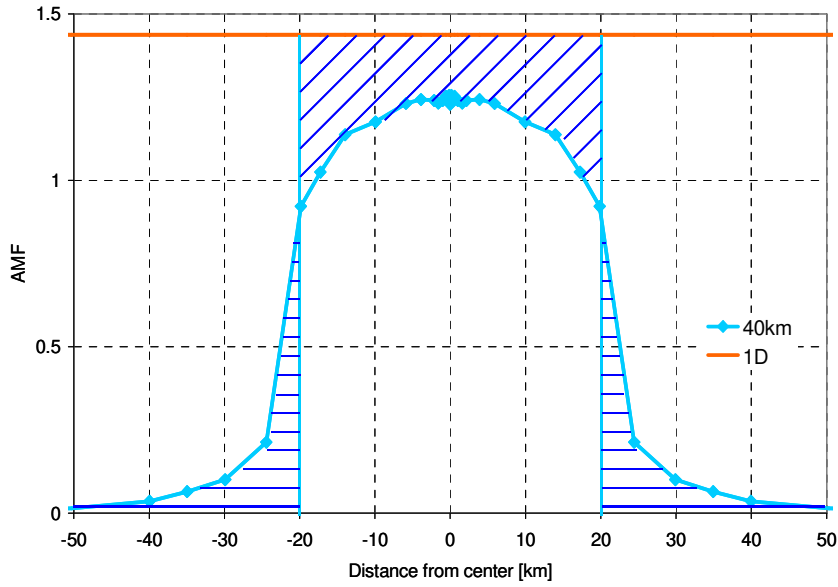


~~Fig. 6~~  ~~$\text{SO}_2$  absorption cross section (273K, Bogumil et al., 2000, see also <https://www.iup.uni-remen.de/gruppen/molspec/databases/sciamachydata/index.html>).~~ The green and orange bars indicate different  $\text{SO}_2$  fit ranges used in the operational TROPOMI product and the MPIC  $\text{SO}_2$  retrieval. The vertical bars indicate ~~wavelengths used in the 3D-RTM simulations.~~

1100

1105

1110



1115 | Fig. 7 AMFs for plume scans (as in Fig. 45) in near-nadir viewing geometry (SZA=0°) for **SO<sub>2</sub> (weak)** at 313 nm and a plume at 5-6 km altitude. In the area of the plume the AMFs are smaller than the 1D-AMF, whereas outside they are larger than zero. The differences are indicated by the blue marked areas for a plume of 40 x 40 km<sup>2</sup>.

1120

1125

1130

1135

1140

1145

Ground pixel size: 3.5 x 5.5 km<sup>2</sup>

Ground pixel size: 200 x 200 km<sup>2</sup>

(TROPOMI)

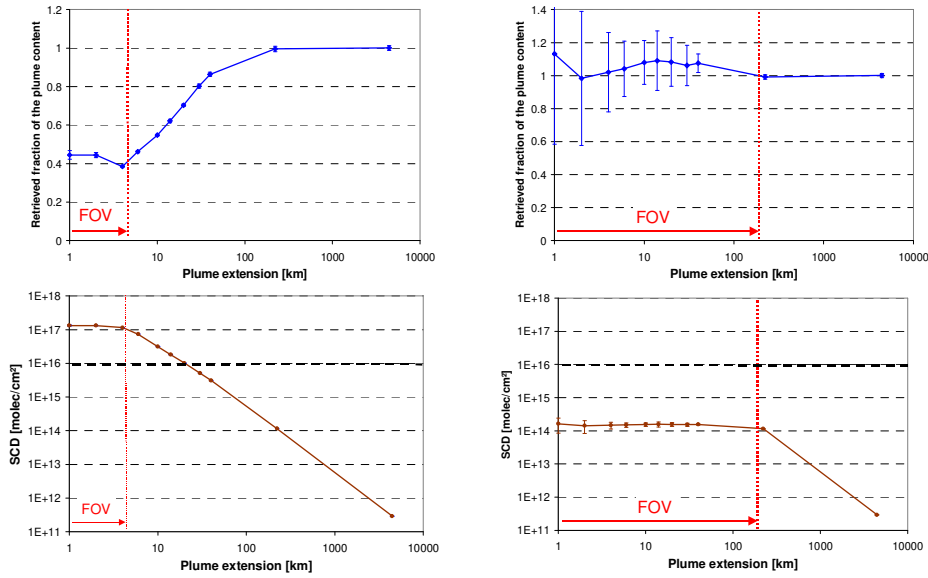
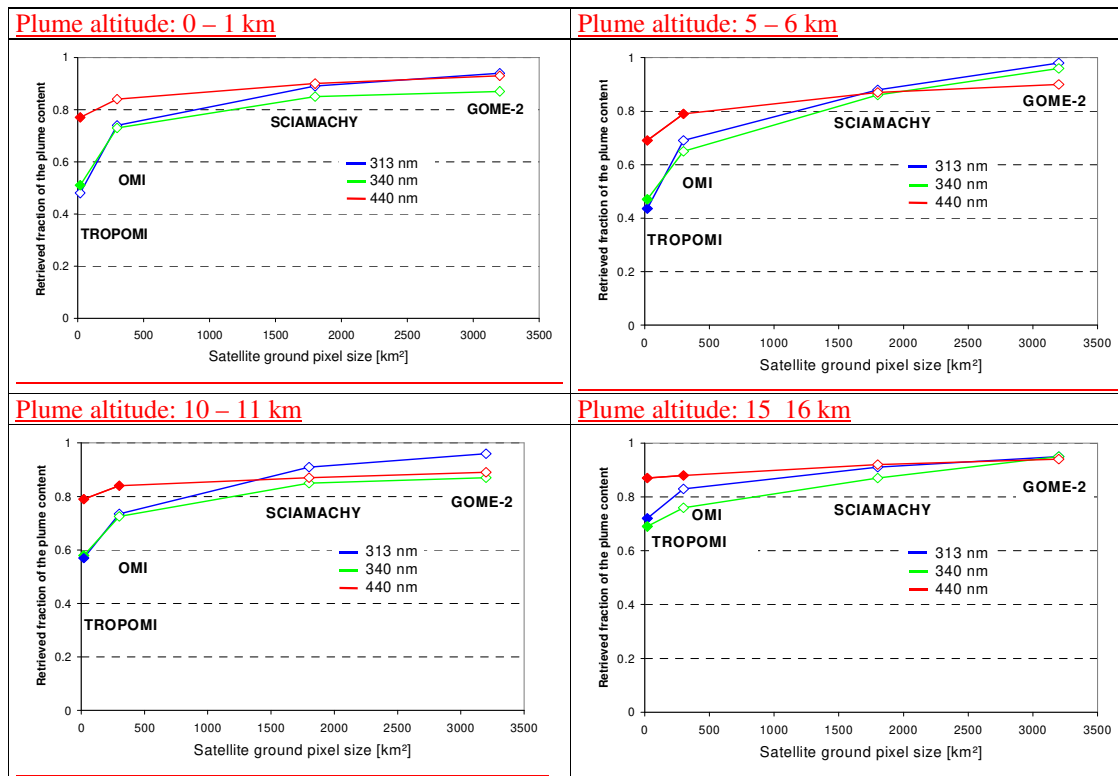


Fig. 8 Top: Retrieved Fraction-fraction of the plume content molecules that is detected inside a ground-pixel (using a 1D-AMF) as a function of the horizontal plume extension (note the logarithmic scale) for measurements of SO<sub>2</sub> at 313 nm. Bottom: measured SO<sub>2</sub> for a SO<sub>2</sub> VCD (for a 1 x 1 km<sup>2</sup> pixel) of 1 · 10<sup>18</sup> molec/cm<sup>2</sup>. The horizontal dashed line indicates the detection limit (assuming an OD threshold of 0.001). Left: results for a TROPOMI ground pixel; right: results for a large ground pixel of 200 x 200 km<sup>2</sup>. Note that in the case of plume size > ground pixel size, only the fraction of the plume within the ground pixel size is considered. Simulations for a plume altitude from 5 to 6 km, wavelength of 313 nm and for VZA=0, and SZA=0°. The error bars represent the standard deviation calculated from 40 individual simulations. Results for other plume altitudes and molecules (wavelengths) are shown in appendix A3.

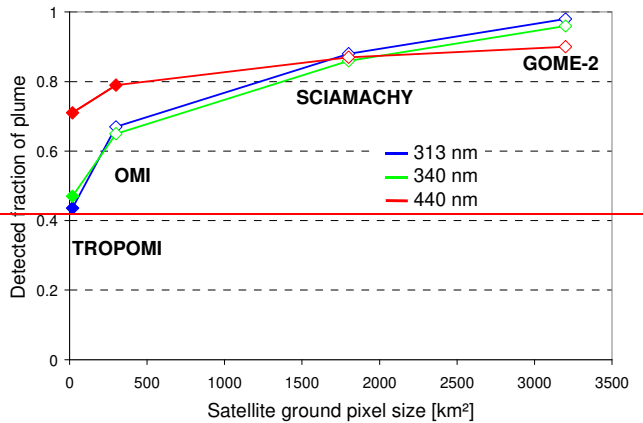


1180 **Fig. 9** Horizontal coverage of a 1 x 1 x 1 km<sup>3</sup> plume (yellow hatched areas) by TROPOMI observations at different wavelengths. The numbers at the top of the TROPOMI pixels indicate the fractions of the plume molecules retrieved from that ground pixel. The numbers at the bottom indicate the optical depth of the trace gas absorption. Red values represent results above the respective detection limit.

1185





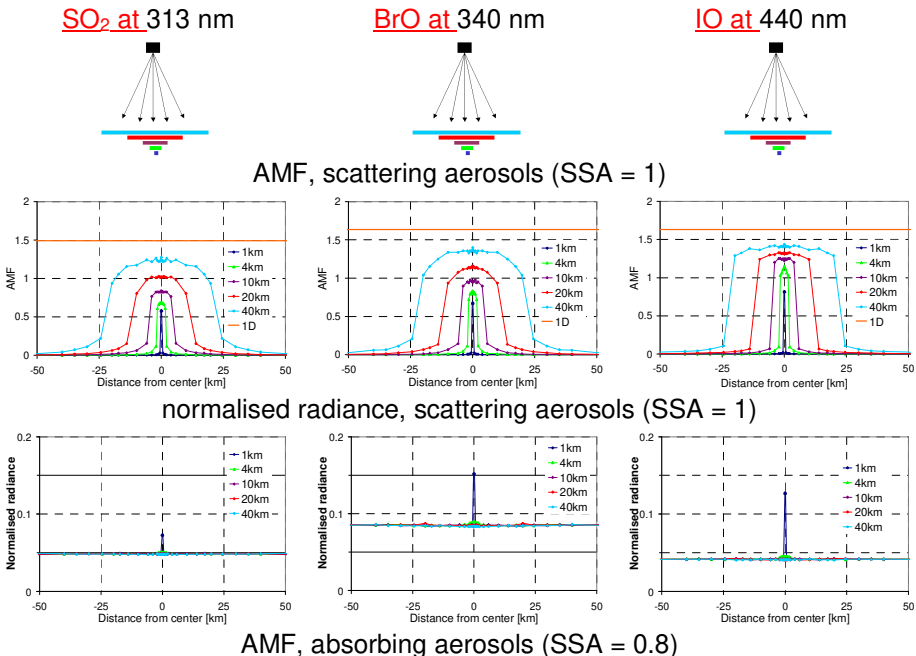


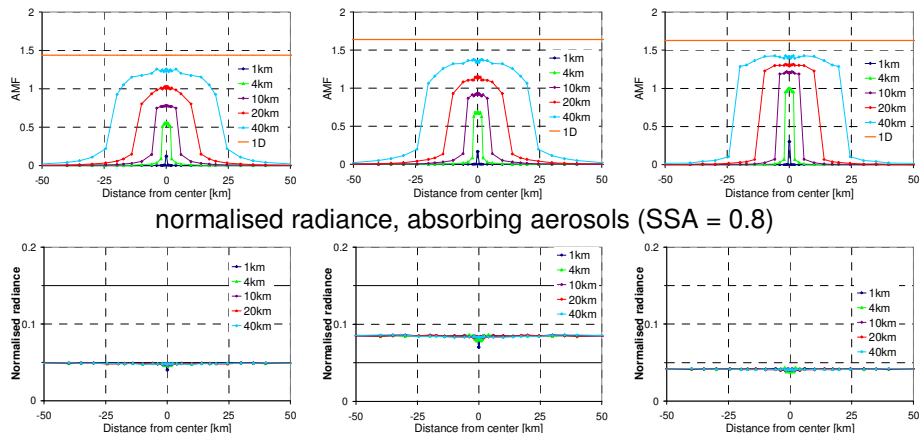
1190 **Fig. 10** retrieved Fraction-fraction of the plume content detected for different satellite sensors if a 1D-AMF is applied (for a 1 x 1 x 1 km<sup>3</sup> plume at 5–6 km different altitudes). Full symbols indicate observations above the detection limit. For the relatively large ground pixel sizes of SCIAMACHY and GOME-2 the errors are between 5 and 10%.

1195

1200

1205





normalised radiance, absorbing aerosols (SSA = 0.8)

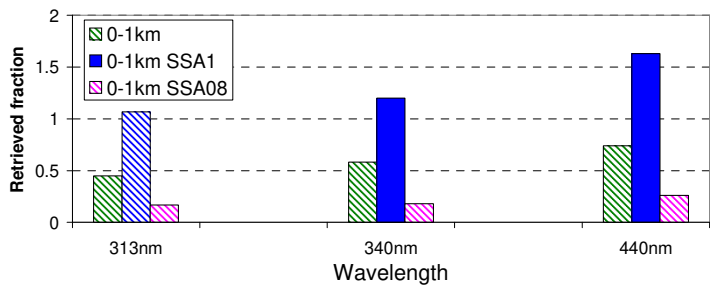
**Fig. 11** AMFs and normalised radiances for plume scans in near-nadir viewing geometry ( $SZA=0^\circ$ ) for different wavelengths and aerosol contents. The satellite scans the plume with a narrow FOV ( $\sim 0.014^\circ$ ). The different colours represent AMFs for plumes at 5 – 6 km altitude and with different horizontal extensions (from  $1 \times 1 \text{ km}^2$  to  $40 \times 40 \text{ km}^2$ ). The rather low radiance at 313 nm (in spite of the high probability of Rayleigh scattering) is caused by the stratospheric ozone absorption. [Results for other plume altitudes are shown in appendix A3.](#)

1210

1215

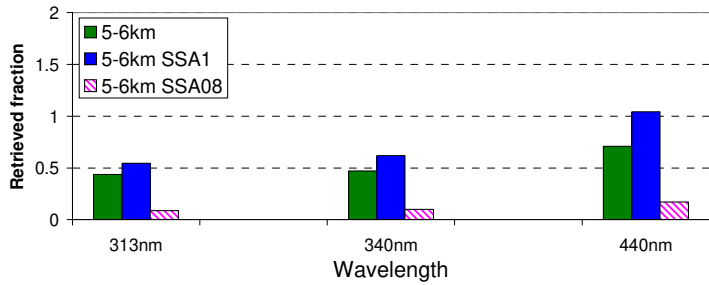
1220

**A) 5-Plume altitude: 0 – 6-1 km**

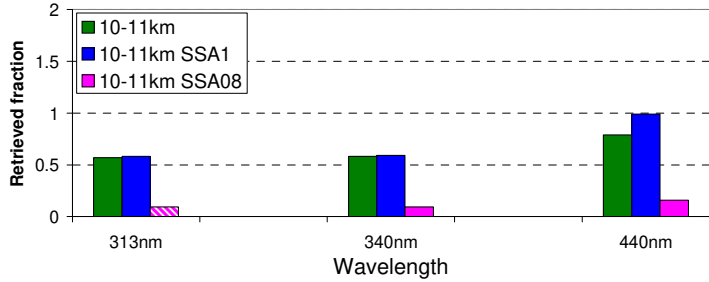


1225

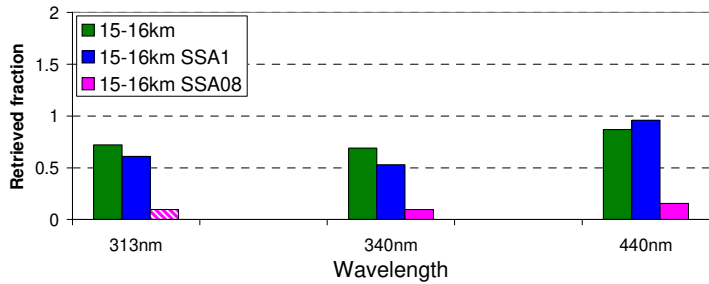
**B) Plume altitude: 5 – 4-6 km**



1230 **C) Plume altitude: 10 – 11 km**



**D) Plume altitude: 15 – 16 km**



1235 **Fig. 12 Retrieved Fraction fraction of the plume content detected at different wavelengths for different plume heights and aerosol scenarios if the respective 1D-AMF at 0 – 1 km or 5 – 6 km altitude (without aerosols) is applied for TROPOMI observations (horizontal plume extension 1 x 1 km<sup>2</sup>). Hatched bars indicate scenarios, for which the absorption is below the detection limit for the weak trace gas scenarios described in section 2.1 (results for the satellite pixel directly above the plume).**

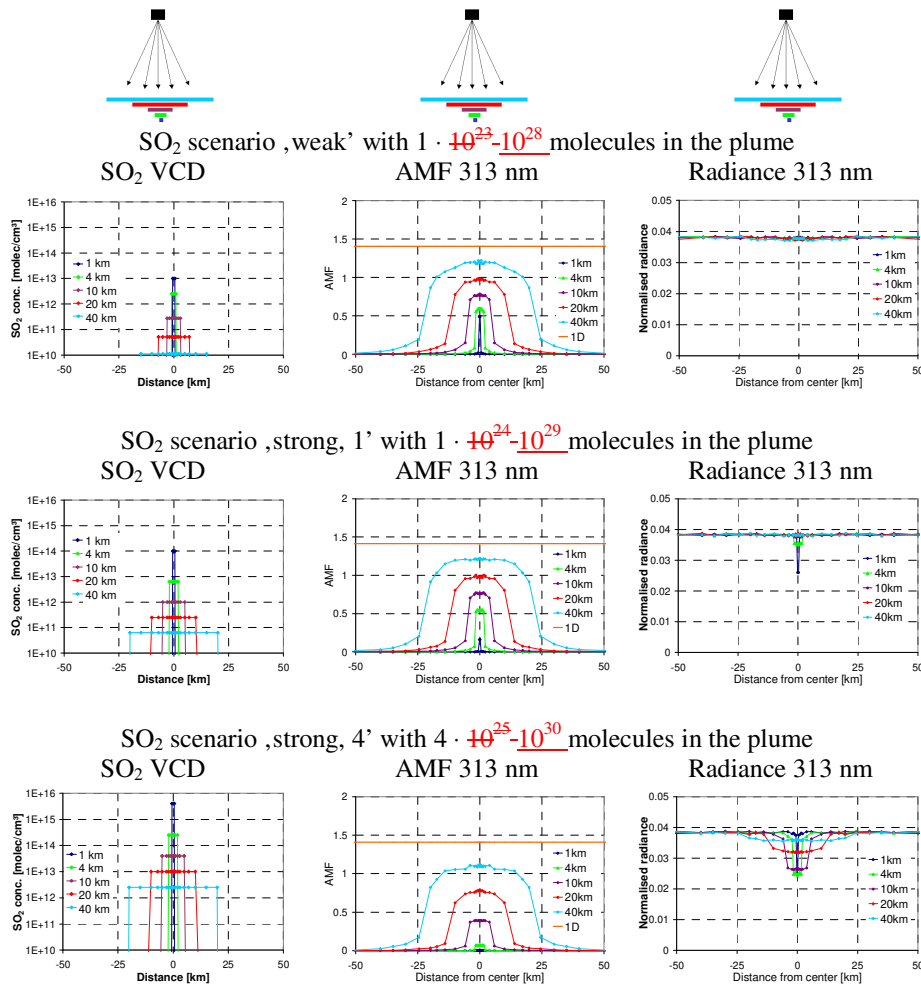
1240

1245

1250

1255

1260



1265

**Fig. 13** Plume scans for SO<sub>2</sub> plumes with different amounts of molecules and different horizontal extensions (for the different SO<sub>2</sub> scenarios, see table 3). Left: SO<sub>2</sub> VCDs of the plumes, middle: AMFs at 313 nm; right: normalised radiances at 313 nm. Here only the scenarios ‘weak,’ ‘strong,1’ and ‘strong,4’ are considered to illustrate the transition from cases with no saturation to cases with medium or strong saturation. The additional intermediate scenarios ‘strong,2’ and ‘strong,3’ are later also used for the quantification of the saturation effect for the different plume extensions (Fig. 14) and satellite instruments (Fig. 15). Results for other plume altitudes are shown in Fig. A3.4 in appendix A3.

1270

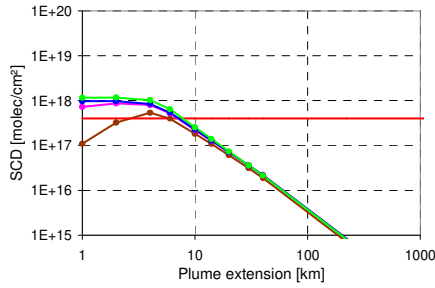
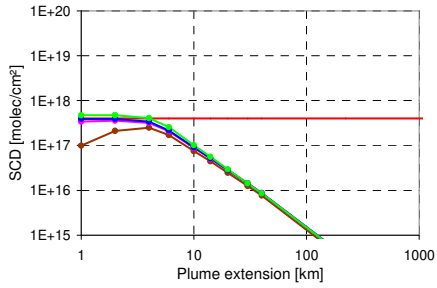
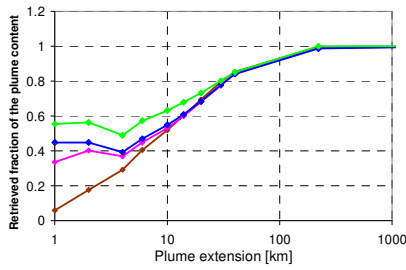
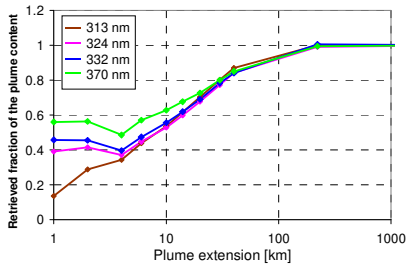
1275

1280

1285

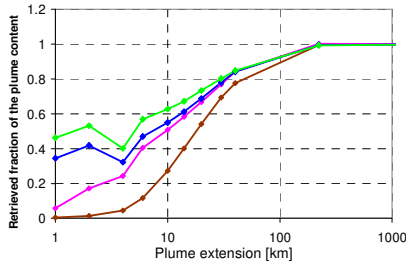
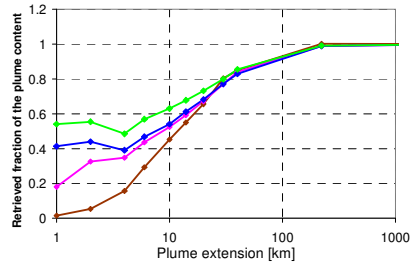
plume content:  $1 \cdot 10^{19}$ - $10^{29}$  molecules

plume content:  $2.5 \cdot 10^{19}$ - $10^{29}$  molecules



plume content:  $1 \cdot 10^{20}$ - $10^{30}$  molecules

plume content:  $4 \cdot 10^{20}$ - $10^{30}$  molecules



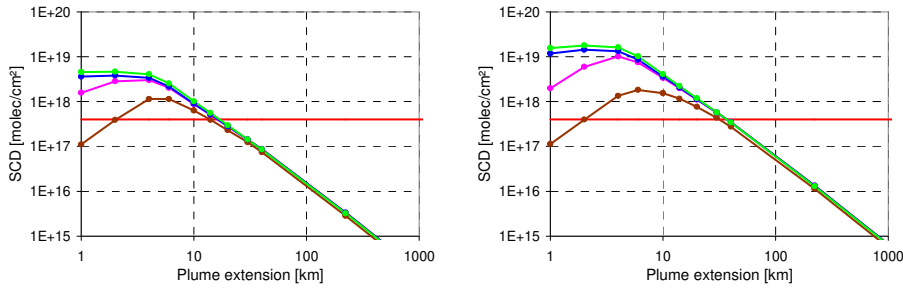
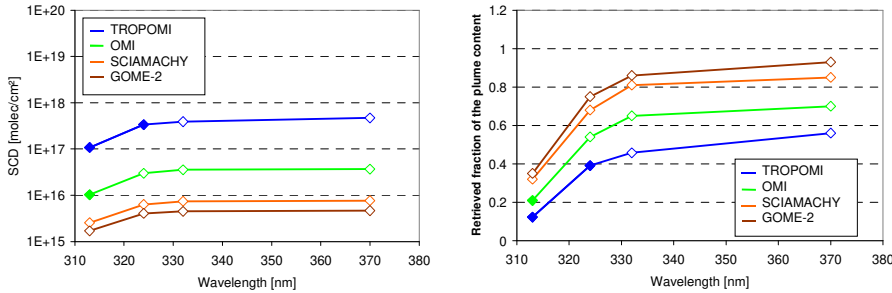


Fig. 14 **Derived-Retrieved** fraction of the plume **molecules content** (top) and SO<sub>2</sub> SCDs (bottom) from TROPOMI measurements at different wavelengths as function of the plume size and for different amounts of molecules in the plume. The red horizontal line indicates the threshold, above which the operational SO<sub>2</sub> retrieval switches from the standard fit window to the first alternative fit window (at longer wavelengths). **Results for other plume altitudes are shown in appendix A3.**

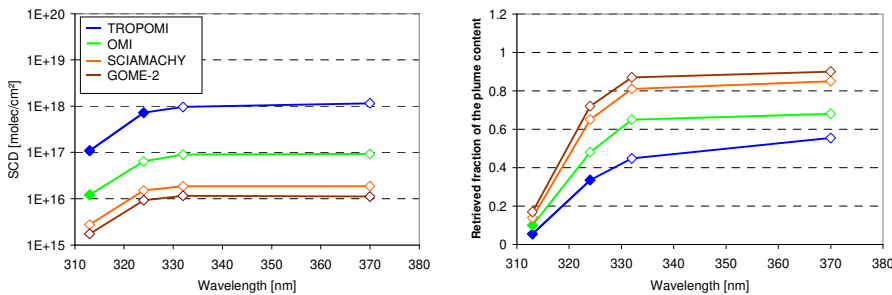
1290

1295

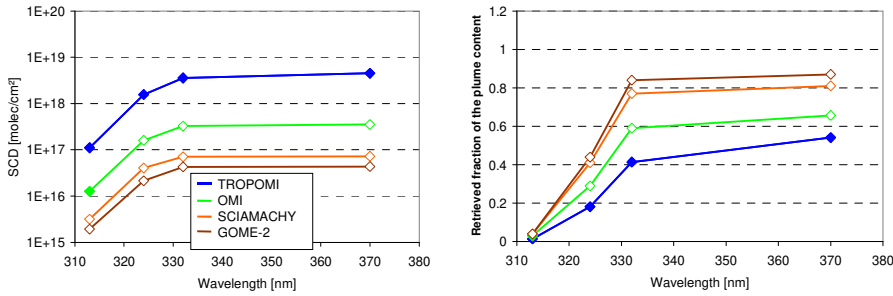
plume content:  $1 \cdot 10^{19}$ - $10^{29}$  molecules, plume size: 1 x 1 km<sup>2</sup>



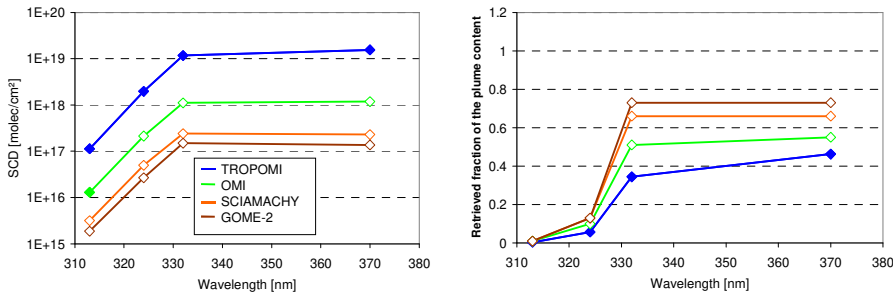
plume content:  $2.5 \cdot 10^{19}$ - $10^{29}$  molecules, plume size: 1 x 1 km<sup>2</sup>



plume content:  $1 \cdot 10^{20}$ - $10^{30}$  molecules, plume size: 1 x 1 km<sup>2</sup>

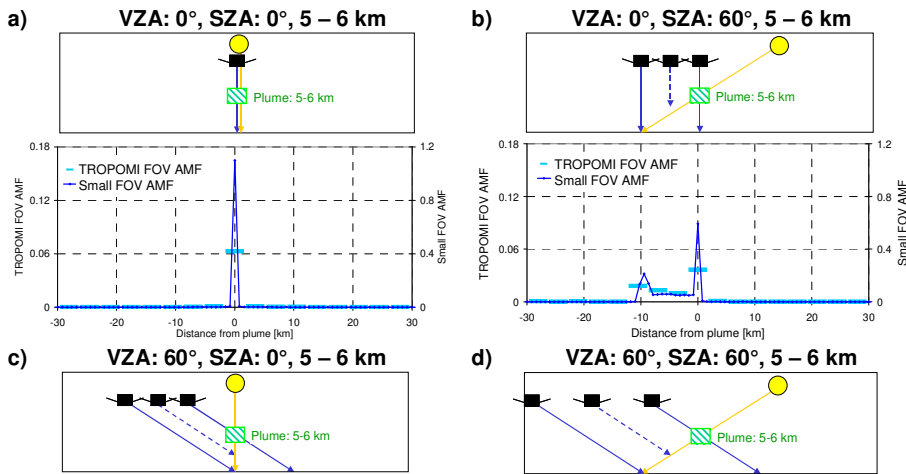


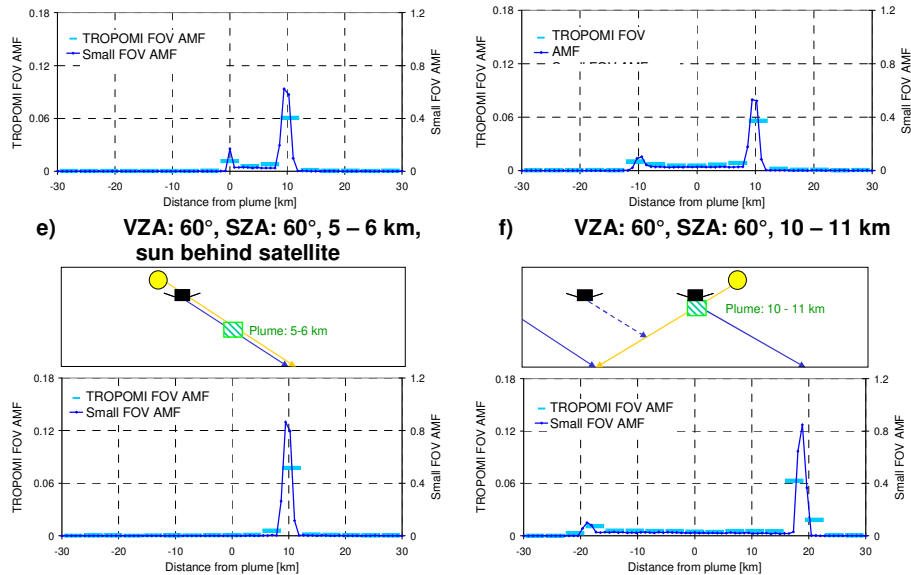
plume content:  $4 \cdot 10^{20} - 10^{30}$  molecules, plume size:  $1 \times 1 \text{ km}^2$



1300 **Fig. 15 Fractions Retrieved fractions (output / input amount of the SO<sub>2</sub> plume) of the plume content and SO<sub>2</sub> SCDs for different satellite instruments and for a plume size of 1 x 1 km<sup>2</sup> as function of the wavelength. The full symbols represent measurements with SCDs above the detection limit. Note that for the rather large ground pixel sizes of SCIAMACHY and GOME-2 the errors are between 5 and 10%. Results for other plume altitudes are shown in appendix A3.**

1305



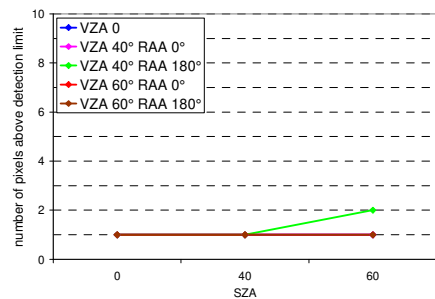


1310 **Fig. 16** AMFs for TROPOMI observations of elevated plumes for different combinations of SZA and VZA. The blue lines show the AMFs for observations with a narrow FOV ( $\sim 0.014^\circ$ ) (right y axis); the bright blue symbols represent simulations with a TROPOMI FOV (left axis). All simulations are for IO at 440 nm and plume sizes of  $1 \times 1 \times 1 \text{ km}^3$ . Results for 313 nm ( $\text{SO}_2$ ) and 340 nm ( $\text{BrO}$ ) are shown in Figs. A5.1 and A5.2 in appendix A5.

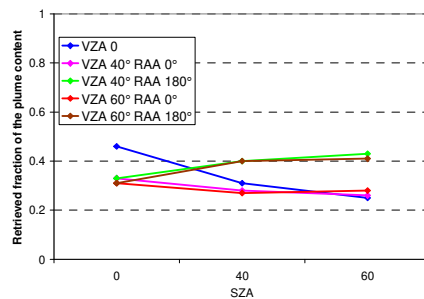
1315

1320

number of pixels above the detection limit for the weak  $\text{SO}_2$  the-scenario (313 nm)

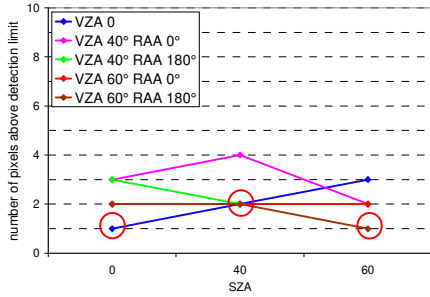


detected-plume-fraction/retrieved fraction of the plume content for the weak  $\text{SO}_2$  scenario (313 nm)

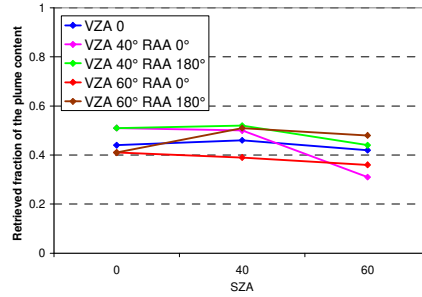




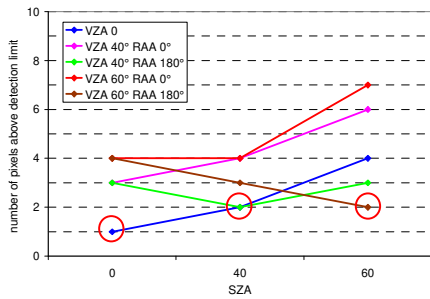
number of pixels above the detection limit for BrO (340 nm)



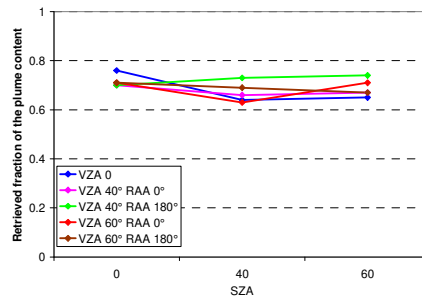
retrieved fraction of the plume content  
detected-plume-fraction for BrO (340 nm)



number of pixels above the detection limit for IO (440 nm)



retrieved fraction of the plume content  
detected-plume-fraction for IO (440 nm)

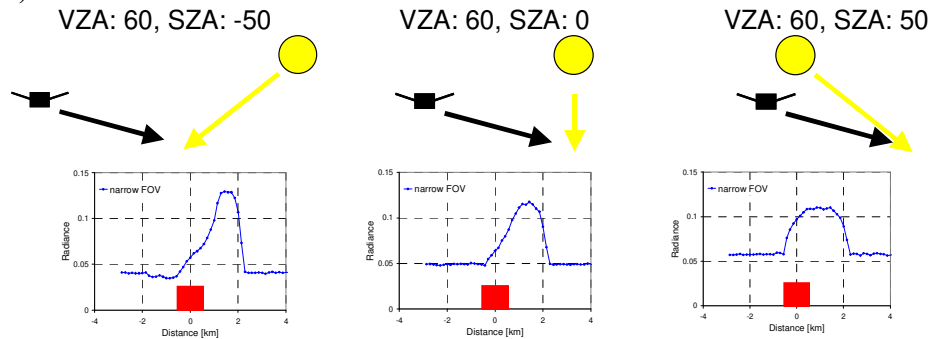


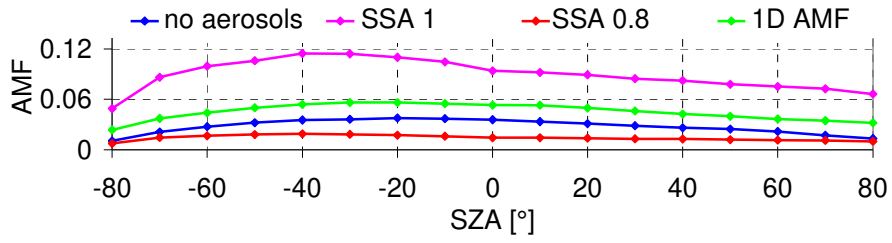
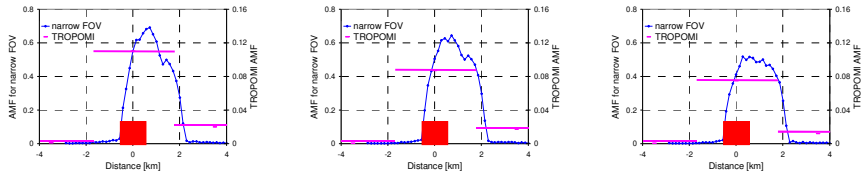
1325 Fig. 17 Number of satellite pixels with SCD above the detection limit (left) and ~~detected~~ retrieved fraction of the plume ~~amount~~ content (right) for TROPOMI observations of SO<sub>2</sub> (weak, 313 nm), BrO (340 nm), and IO (440 nm) with different viewing and solar zenith angles. The plume has an extension of 1 x 1 x 1 km<sup>3</sup> and is located at 5 – 6 km altitude. Left: results for the scenario IO-VCD<sub>low</sub>; right: results for scenario IO-VCD<sub>high</sub> (see table 3). The red circles indicate scenarios with the sun and the satellite in the same direction for which the smearing effect is smallest. RAA indicates the relative azimuth angle between the viewing direction and the sun. Here a RAA of 180° represents cases where the sun shines in the same direction of the satellite view.

1330

1335

a) 440 nm





1340

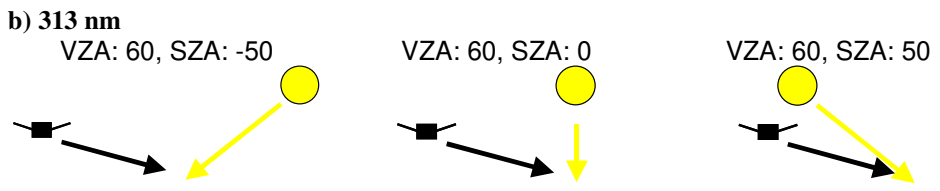
1345

1350

1355

1360

1365



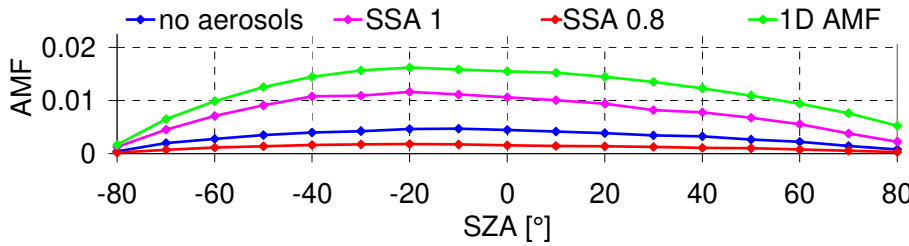
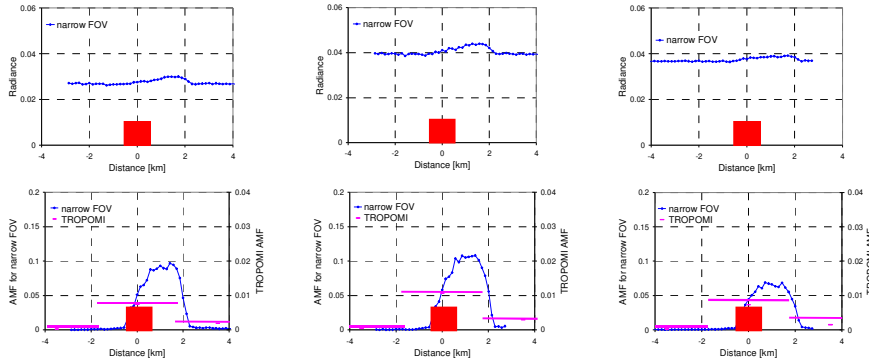


Fig. 18 Dependence of the AMF and normalised radiance for a slant viewing angle ( $VZA = 60^\circ$ ) on the illumination angle for IO at 440 nm (a) and SO<sub>2</sub> at 313 nm (b). The upper panels show sketches of the investigated viewing and illumination angles (SZA of  $-50^\circ$ ,  $0^\circ$ ,  $50^\circ$ ). The middle panels show the normalised radiances and AMFs for these scenarios (for plumes with scattering aerosols) as function of the relative distance from the plume ( $1 \times 1 \times 1 \text{ km}^3$ , red boxes). Note the different y-axes for the AMFs calculated for a narrow FOV (left) or TROPOMI FOV (right). The plume is located directly above the surface ( $0 - 1 \text{ km}$ ). The bottom panels show the AMFs for a TROPOMI FOV as function of the SZA (also for a  $VZA$  of  $60^\circ$ ). The different lines represent 3D-AMFs for plumes without aerosols (blue), with scattering (magenta) and absorbing (red) aerosols as well as the 1D-AMF (without aerosols).

1370

1375

1380

1385

1390

SO<sub>2</sub> at 313 nm,  $VZA: 0^\circ$       BrO at 340 nm,  $VZA: 0^\circ$       IO at 440 nm,  $VZA: 0^\circ$

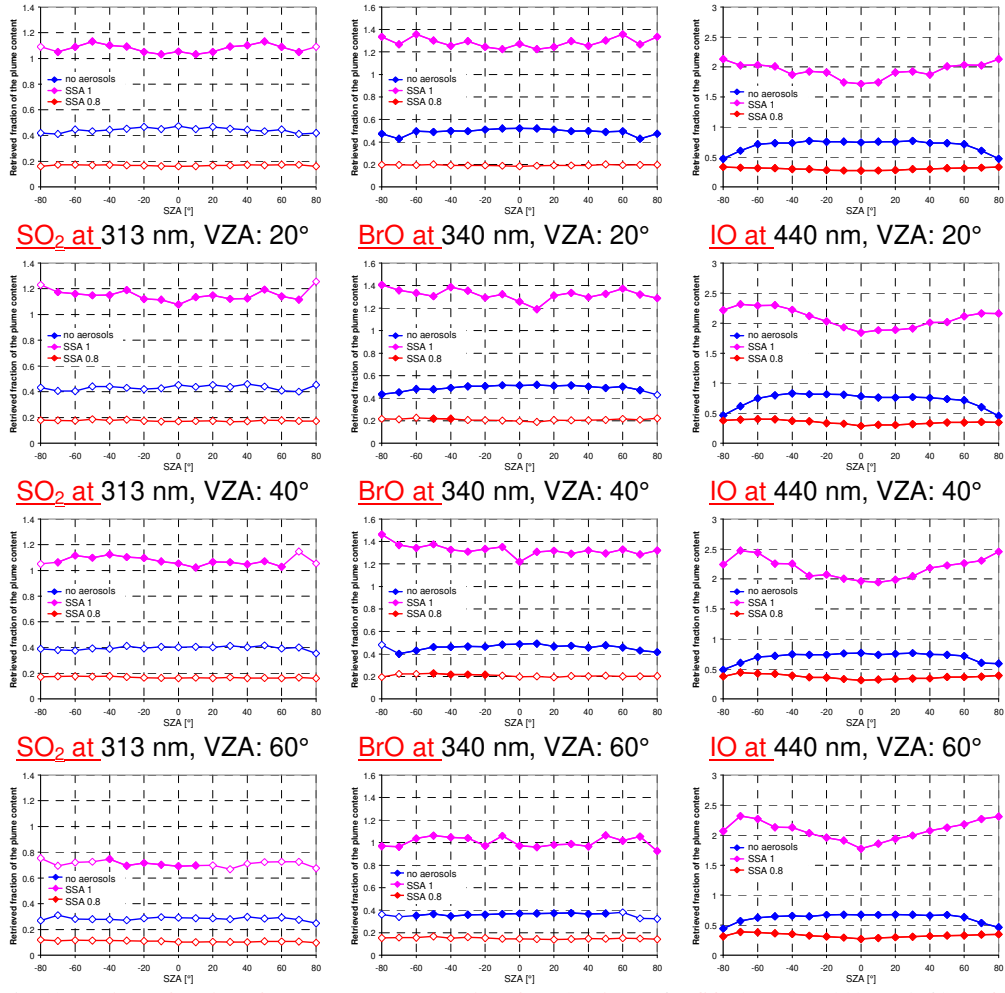
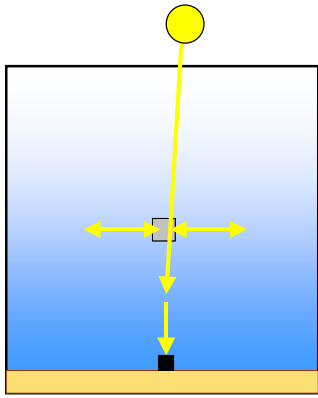


**Fig. 19 Retrieved fraction of the plume content Ratios of the 3D-AMFs for  $\text{SO}_2$  (weak) at 313 nm (left), BrO at 340 nm (center) and IO at 440 nm (right) divided by the corresponding 1D-AMFs as function of the SZA for different viewing angles (blue: plume without aerosols; magenta: plume with scattering aerosols; red: plume with absorbing aerosols).**

1395 Symbols in full colour represent results above the detection limit.

1400

Zenith view, SZA: 0.3°



Zenith view, SZA: 10°

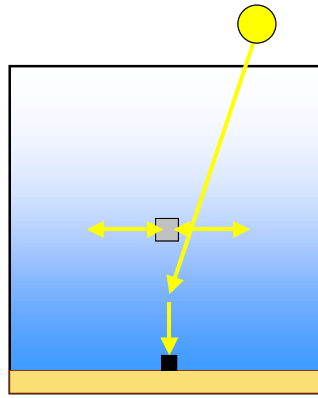


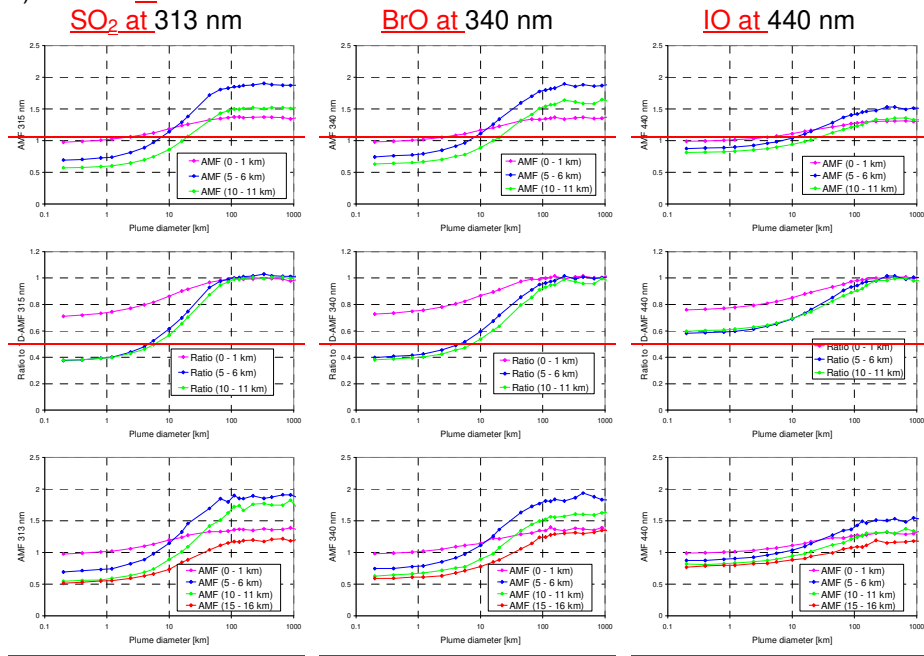
**Fig. 20** Ground based observations of a narrow plume in zenith direction. For almost overhead sun (SZA of 0.3°, left), the direct sun light traverses the plume before it is scattered into the field of view of the instrument. For larger SZA (right), direct sun light is scattered into the field of view of the instrument without having crossed the plume. In both scenarios no direct sun light is observed by the instruments.

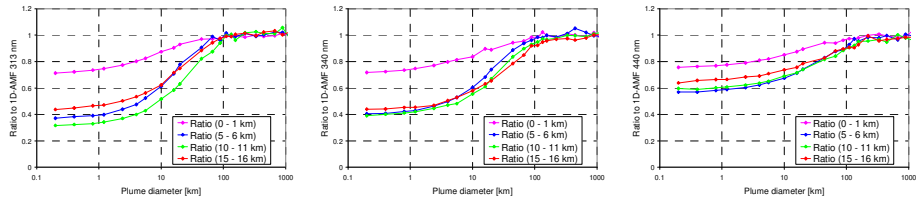
1405

1410

1415

a) SZA = 0.3°



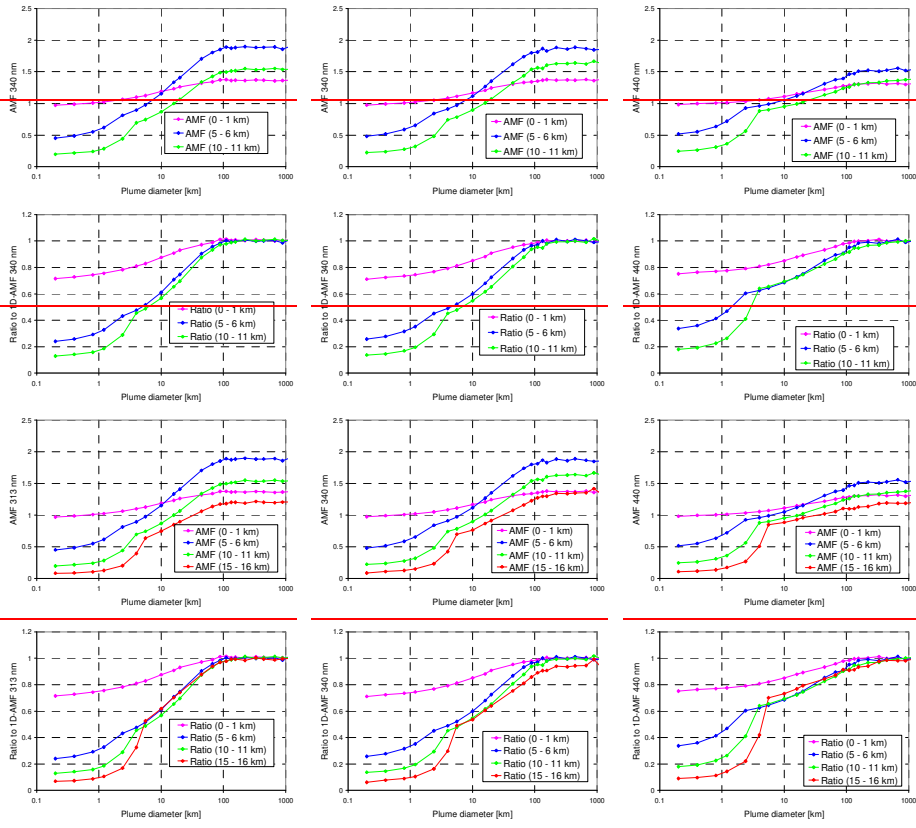


b) SZA = 10°

SO<sub>2</sub> at 313 nm

BrO at 340 nm

IO at 440 nm



1420

**Fig. 20-21** Dependence of the AMF on the horizontal plume extension for ground based observations (FOV: 0.014°, VZA = 0°, SZA = 0.3° (a) and SZA = 10° (b). In the upper panels the AMFs for different plume altitudes and wavelengths are shown. In the bottom panels the AMFs normalised by the corresponding 1D AMFs are shown.

1425

1430

1435

1440

1445

Appendix A1 Selection of surface albedo and influence of the surface albedo on the RTM results

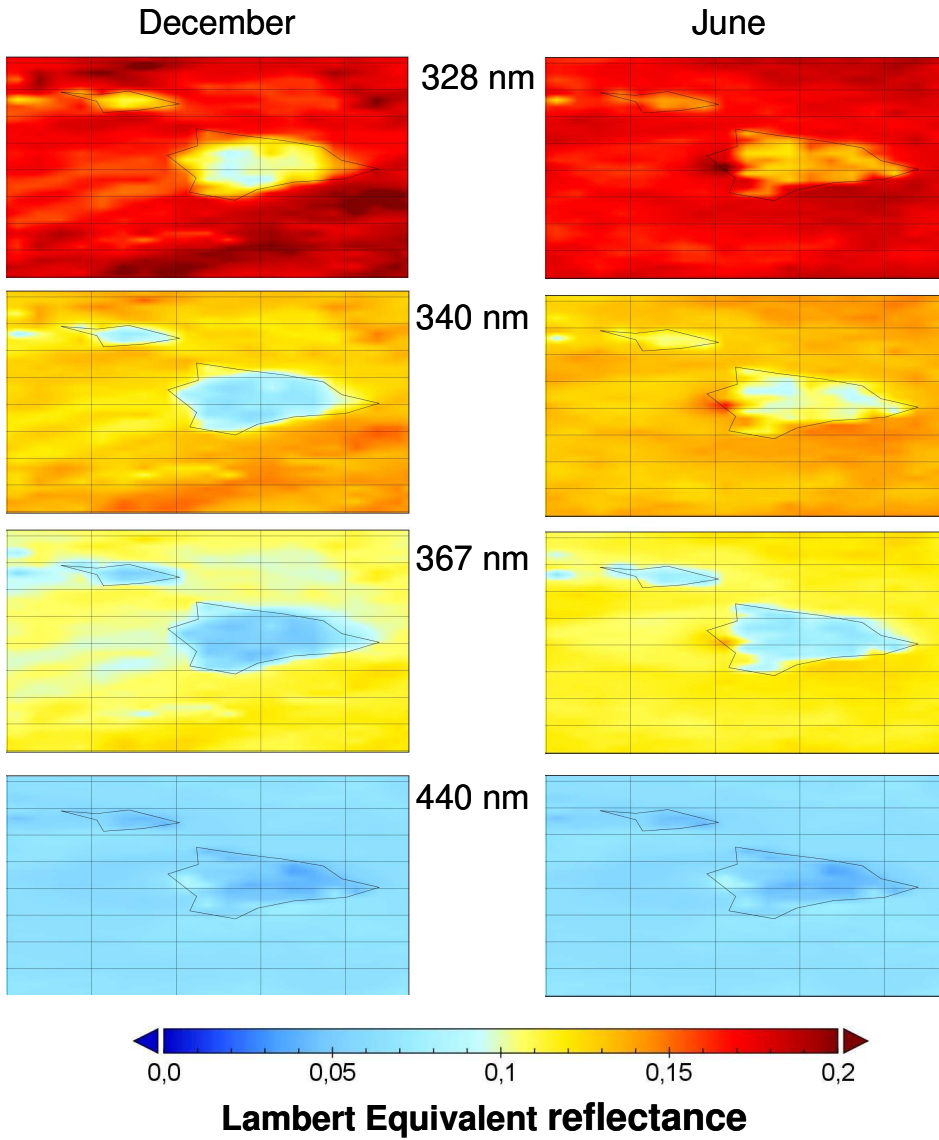
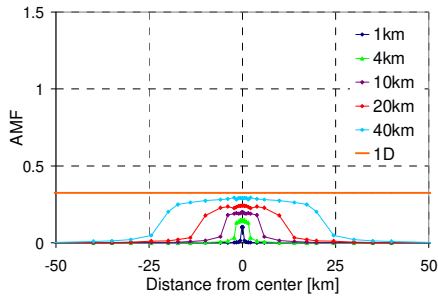


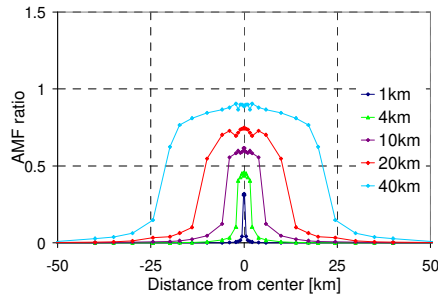
Fig. A1.1 Minimum Lambertian equivalent albedos over Hawaii derived from TROPOMI observations for December (left) and June (right). Data obtained from the TEMIS data base (<https://www.temis.nl/>), see also Tilstra et al. (2021).

1450

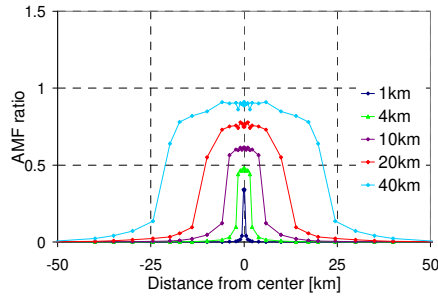
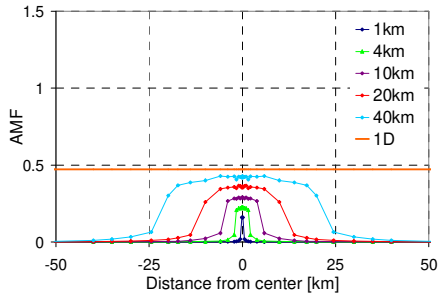
a) AMF for SO<sub>2</sub> at 313 nm, albedo 5%      AMF ratio for SO<sub>2</sub> at 313 nm, albedo 5%



AMF for SO<sub>2</sub> at 313 nm, albedo 10%

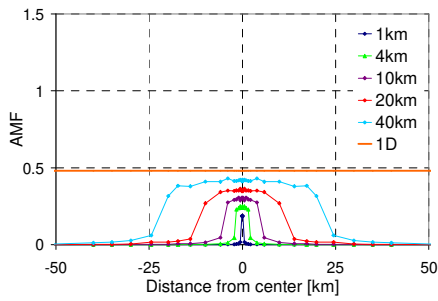


AMF ratio for SO<sub>2</sub> at 313 nm, albedo 10%

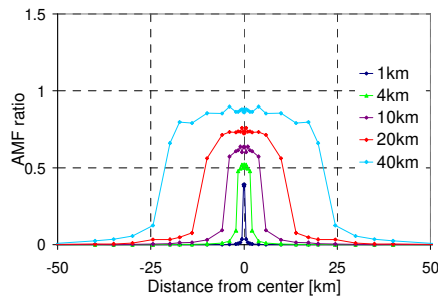


b)

AMF for BrO at 340 nm, albedo 5%

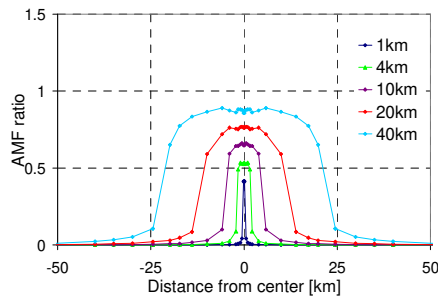
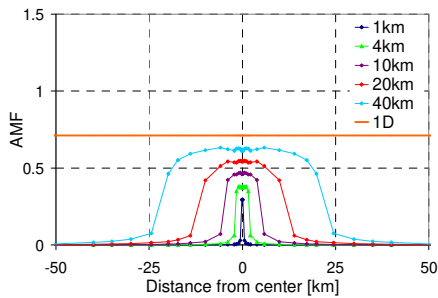


AMF ratio for BrO at 340 nm, albedo 5%



AMF for BrO at 340 nm, albedo 10%

AMF ratio for BrO at 340 nm, albedo 10%



1455

c)

AMF for IO at 440 nm, albedo 5%

AMF ratio for IO at 440 nm, albedo 5%



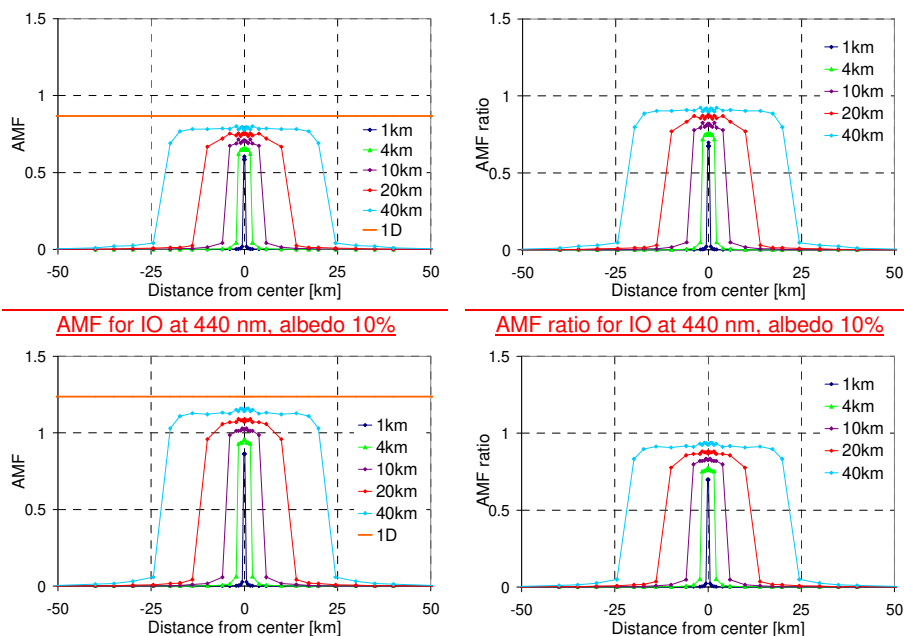


**Fig. A1.2 AMFs (left) and corresponding ratios to the 1D-AMFs (right) for plume scans in near-nadir viewing geometry ( $SZA=0^\circ$ ,  $VZA=0^\circ$ ) for (a)  $SO_2$  at 313 nm, (b)  $BrO$  at 340 nm, and (c)  $IO$  at 440 nm. It is assumed that the satellite scans the plume with a narrow FOV ( $\sim 0.014^\circ$ ). The different colours represent AMFs for plumes at 5-6 km altitude and with different horizontal extensions (from  $1 \times 1 \text{ km}^2$  to  $40 \times 40 \text{ km}^2$ ). Results are shown for a surface albedo of 5% (as used in general in this study) and 10%. The ratios of the AMFs for narrow plumes to the corresponding 1D-AMFs hardly depend on the surface albedo.**

#### Appendix A1-A2 Differential absorption cross sections for the selected trace gases and wavelengths

The following table shows a summary of the differential absorption cross sections used in this study to relate the trace gas SCDs to the corresponding optical depths.

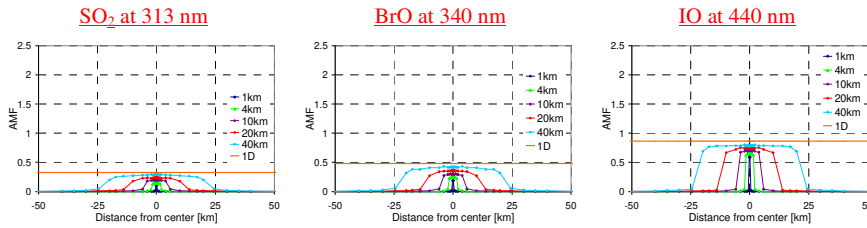
The values were determined by convolution of the original cross section with a ~~Gaussian~~ Gaussian slit function with FWHM of 0.5 nm (similar to TROPOMI). In addition to the  $IO$  absorption cross section also those of  $H_2O$  and  $NO_2$  are shown, which could also be analysed in the same spectral range around 440 nm. Note that the absorption cross sections depend on temperature. Also the values from different studies differ, especially for  $IO$  and  $H_2O$ . Finally, the differential absorption cross sections will depend on the spectral resolution of the instrument. Thus the values in Table A.1.1 can serve as useful reference (e.g. in this study), but might differ for other applications.

**Table A1A2.1 Differential absorption cross sections for the trace gases considered in this study.**

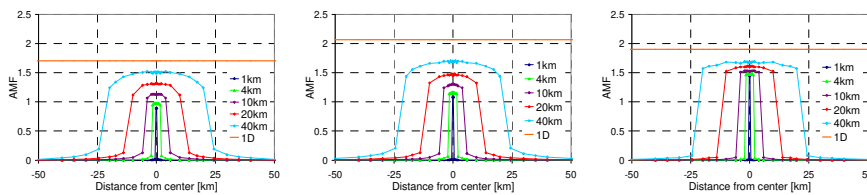
Trace gas, wavelength	Differential absorption cross section after convolution with Gaussian instrument line shape with FWHM of 0.5 nm.
$SO_2$ , 313 nm (Bogumil et al., 2000)	$1 \cdot 10^{-19} \text{ cm}^2$
$SO_2$ , 324 nm (Bogumil et al., 2000)	$4 \cdot 10^{-21} \text{ cm}^2$
$SO_2$ , 332 nm (Bogumil et al., 2000)	$4 \cdot 10^{-22} \text{ cm}^2$
$SO_2$ , 370 nm (Bogumil et al., 2000)	$5 \cdot 10^{-22} \text{ cm}^2$
$BrO$ , 340 nm (Wilmouth et al., 1999)	$1.7 \cdot 10^{-17} \text{ cm}^2$
$IO$ , 440 nm (Hönninger, 1999 <del>2000</del> )	$2 \cdot 10^{-17} \text{ cm}^2$
$NO_2$ , 440 nm (Vandaele et al., 1997)	$3 \cdot 10^{-19} \text{ cm}^2$
$H_2O$ , 440 nm (Rothman et al., 2005)	$3.4 \cdot 10^{26} \text{ cm}^2$

**Appendix A3 Simulation results for different plume altitudes**

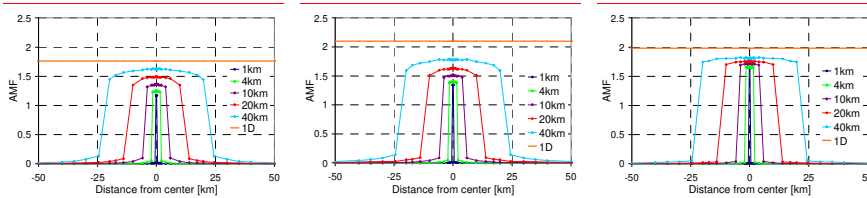
**Height**  
**0-1km**



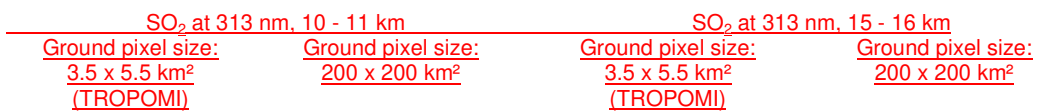
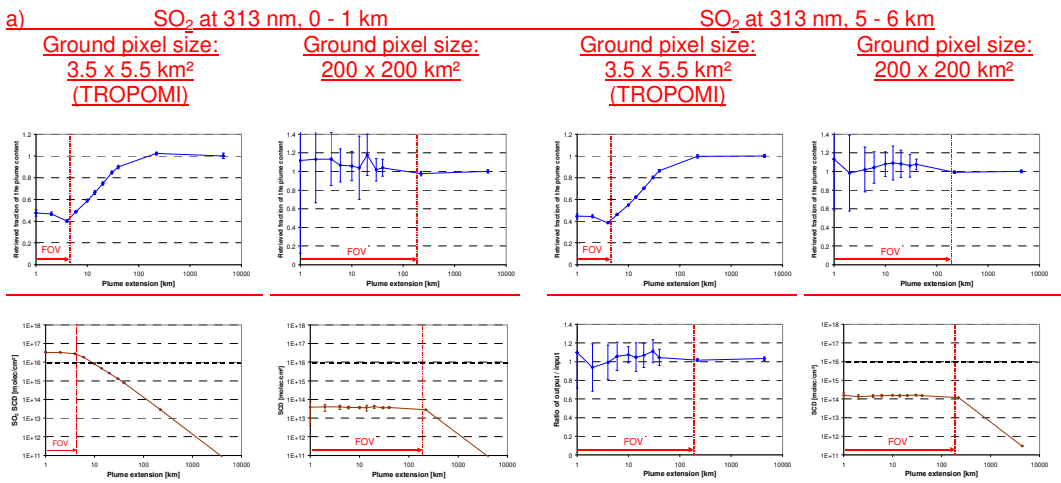
**10-11km**

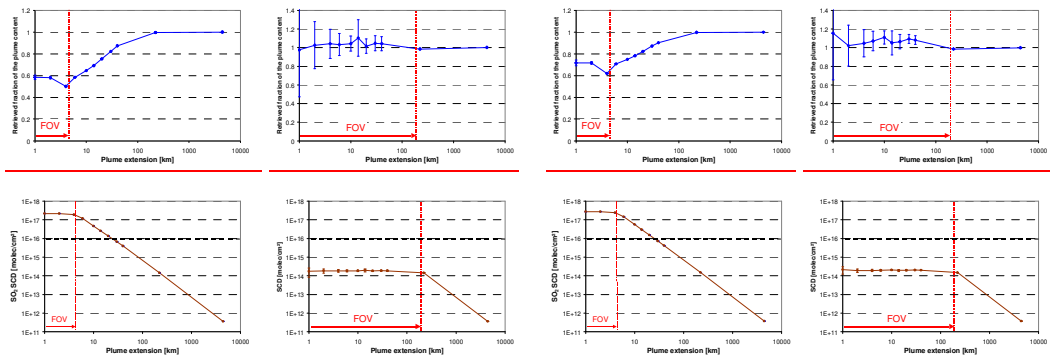


**15-16km**

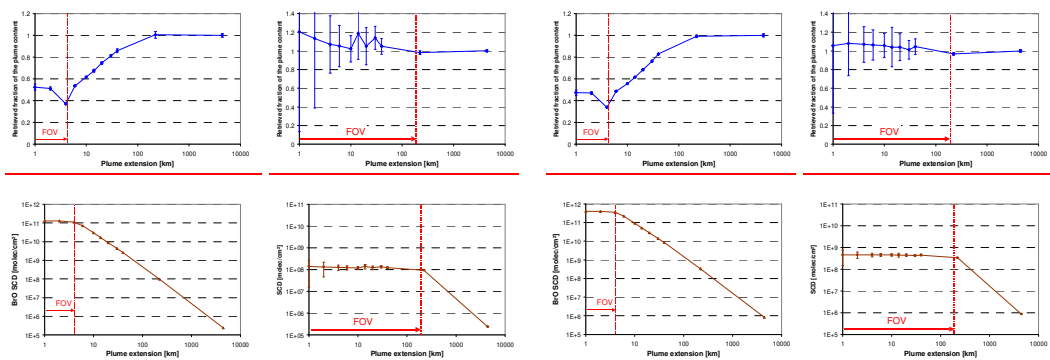


**Fig. A3.1 Same as Fig. 5, but for additional plume heights: AMFs for plume scans in near-nadir viewing geometry (SZA=0°, VZA=0°) at different wavelengths. It is assumed that the satellite scans the plume with a narrow FOV (~0.014°). The different colours represent AMFs for plumes with different horizontal extensions (from 1 x 1 km² to 40 x 40 km²).**



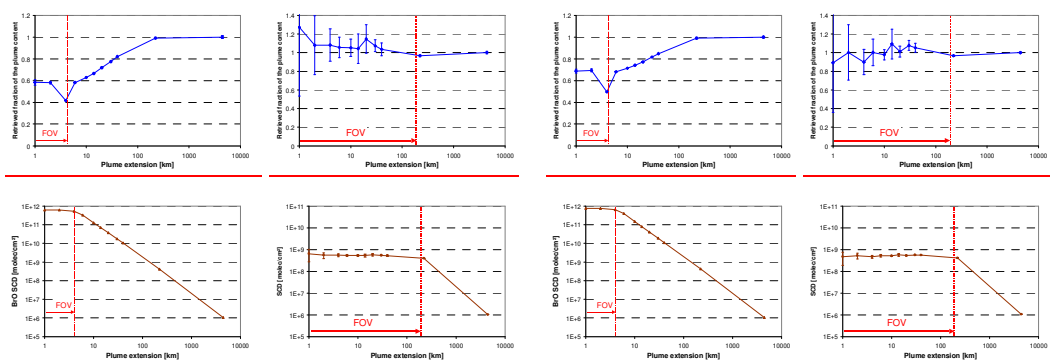


b) **BrO at 340 nm, 0 - 1 km** **BrO at 340 nm, 5 - 6 km**  
Ground pixel size: 3.5 x 5.5 km<sup>2</sup> (TROPOMI) Ground pixel size: 200 x 200 km<sup>2</sup> Ground pixel size: 3.5 x 5.5 km<sup>2</sup> (TROPOMI) Ground pixel size: 200 x 200 km<sup>2</sup>



1495

**BrO at 340 nm, 10 - 11 km** **BrO at 340 nm, 15 - 16 km**  
Ground pixel size: 3.5 x 5.5 km<sup>2</sup> (TROPOMI) Ground pixel size: 200 x 200 km<sup>2</sup> Ground pixel size: 3.5 x 5.5 km<sup>2</sup> (TROPOMI) Ground pixel size: 200 x 200 km<sup>2</sup>

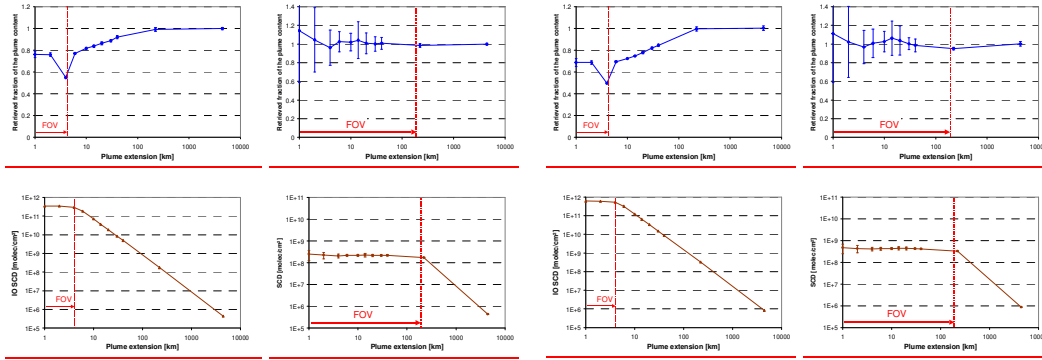


1500

c) **IO at 440 nm, 0 - 1 km** **IO at 440 nm, 5 - 6 km**  
Ground pixel size: 3.5 x 5.5 km<sup>2</sup> Ground pixel size: 200 x 200 km<sup>2</sup> Ground pixel size: 3.5 x 5.5 km<sup>2</sup> Ground pixel size: 200 x 200 km<sup>2</sup>

(TROPOMI)

(TROPOMI)



c) IO at 440 nm, 10 - 11 km IO at 440 nm, 15 - 16 km  
 Ground pixel size:  $3.5 \times 5.5 \text{ km}^2$  (TROPOMI) Ground pixel size:  $200 \times 200 \text{ km}^2$   
 Ground pixel size:  $200 \times 200 \text{ km}^2$  Ground pixel size:  $3.5 \times 5.5 \text{ km}^2$  (TROPOMI)

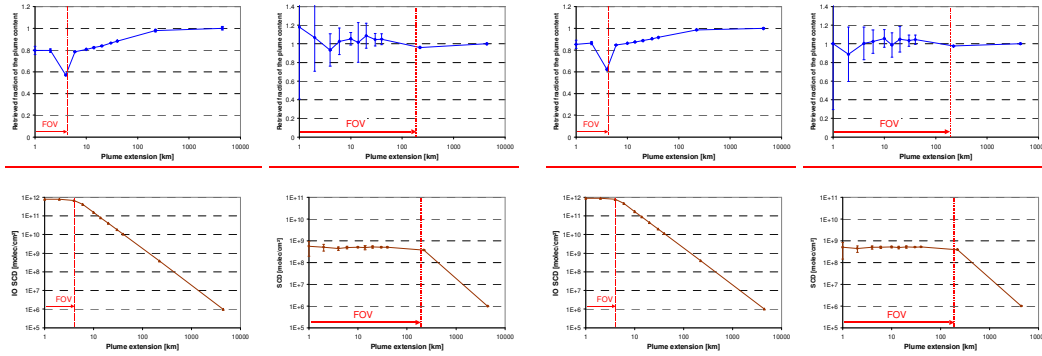


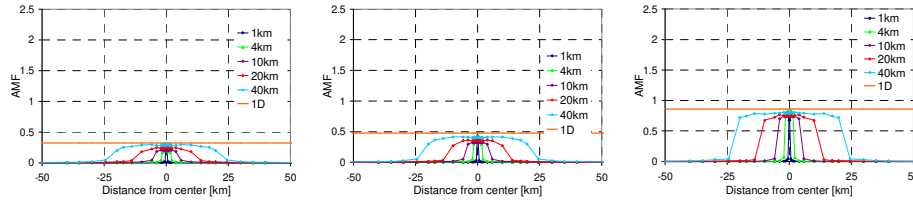
**Fig. A3.2 Same as Fig. 8, but for additional plume heights and wavelengths: Top: Retrieved fraction of the plume content as a function of the horizontal plume extension (note the logarithmic scale). Bottom: measured trace gas SCDs (for a  $1 \times 1 \text{ km}^2$  pixel). The horizontal dashed line indicates the detection limits (see section 2.1). Left: results for a TROPOMI ground pixel; right: results for a large ground pixel of  $200 \times 200 \text{ km}^2$ . Note that in the case of plume size > ground pixel size, only the fraction of the plume within the ground pixel size is considered. Simulations for  $VZA=0^\circ$  and  $SA=0^\circ$ . The error bars represent the standard deviation calculated from 40 individual simulations.**

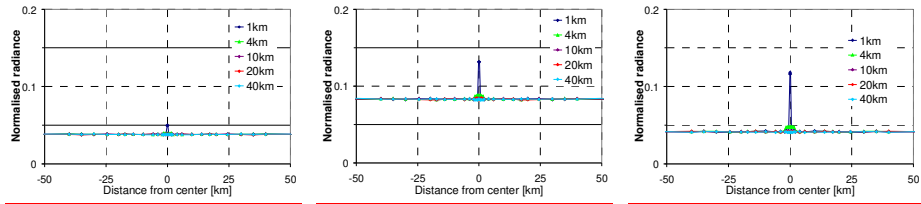
a) 0-1 km

313 nm, SSA=1

340 nm, SSA=1

440 nm, SSA=1

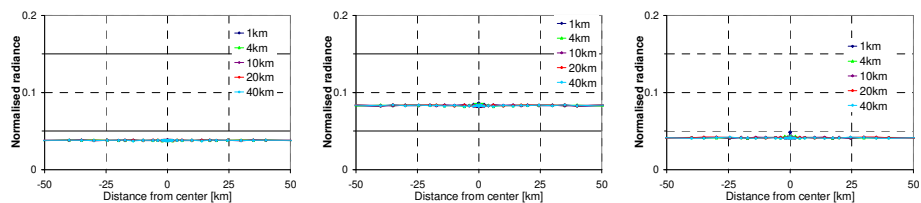
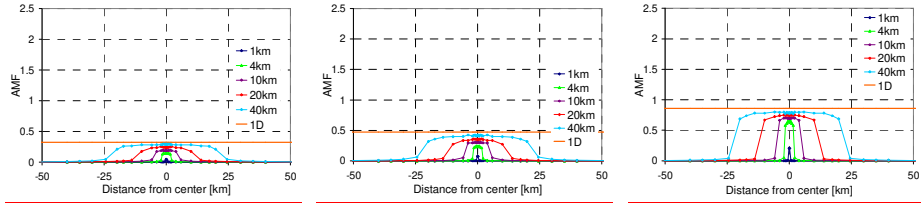




313 nm, SSA=0.8

340 nm, SSA=0.8

440 nm, SSA=0.8

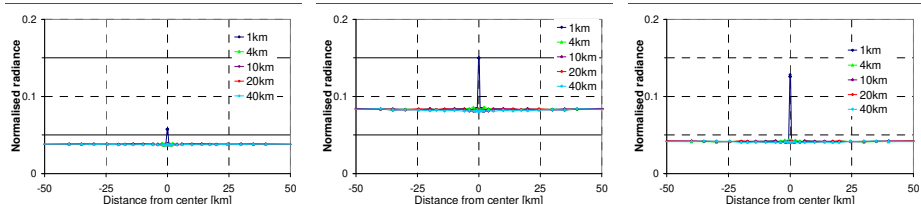
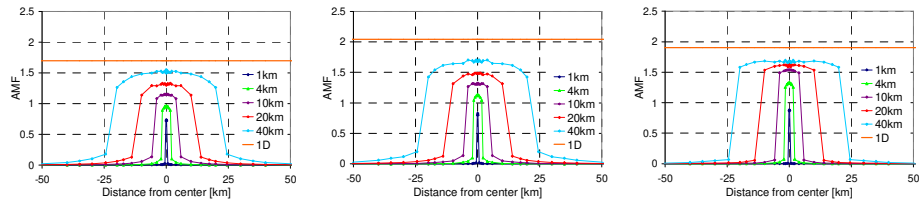


b) 10-11 km

313 nm, SSA=1

340 nm, SSA=1

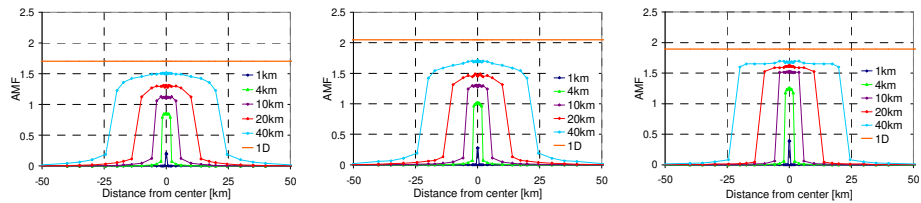
440 nm, SSA=1



313 nm, SSA=0.8

340 nm, SSA=0.8

440 nm, SSA=0.8



1520

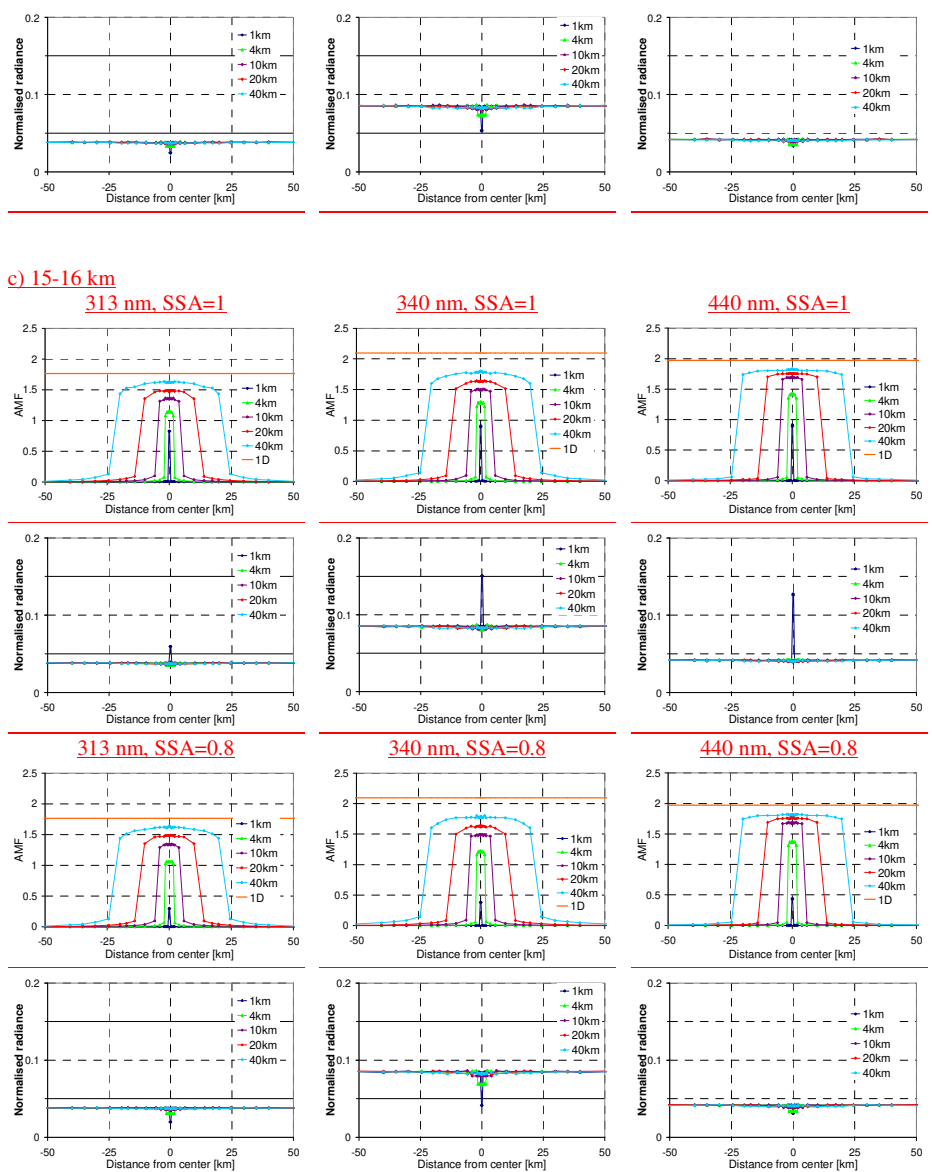
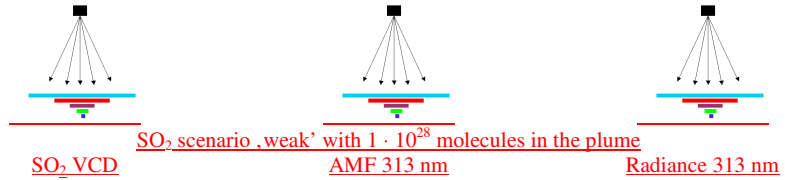


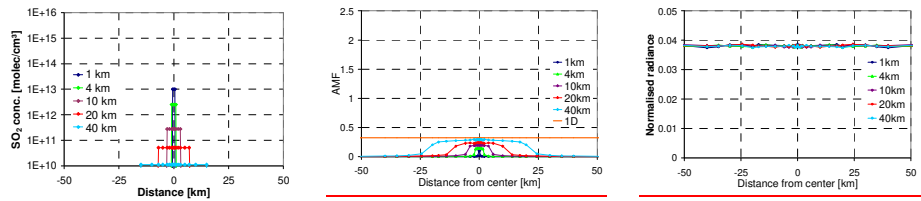
**Fig. A3.3** Same as Fig. 11, but for additional plume heights: AMFs and normalised radiances for plume scans in near-nadir viewing geometry ( $SSA=0^\circ$ ) for different wavelengths and aerosol contents. The satellite scans the plume with a narrow FOV ( $\sim 0.014^\circ$ ). The different colours represent AMFs for plumes with different horizontal extensions (from  $1 \times 1 \text{ km}^2$  to  $40 \times 40 \text{ km}^2$ ). The rather low radiance at 313 nm (in spite of the high probability of Rayleigh scattering) is caused by the stratospheric ozone absorption.

1525

1530

a) 0-1km



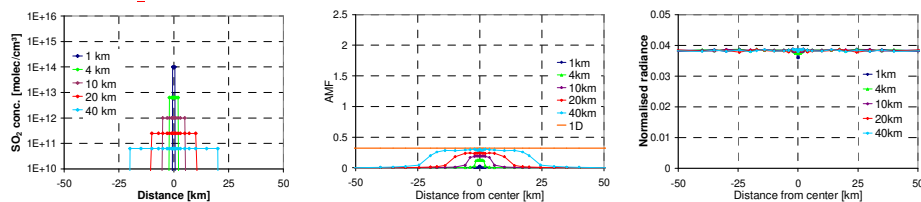


SO<sub>2</sub> scenario ,strong, 1' with  $1 \cdot 10^{29}$  molecules in the plume

SO<sub>2</sub> VCD

AMF 313 nm

Radiance 313 nm

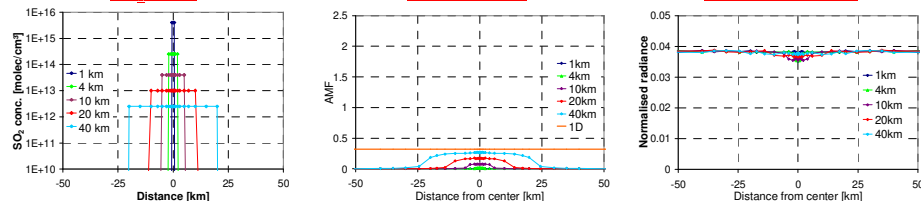


SO<sub>2</sub> scenario ,strong, 4' with  $4 \cdot 10^{30}$  molecules in the plume

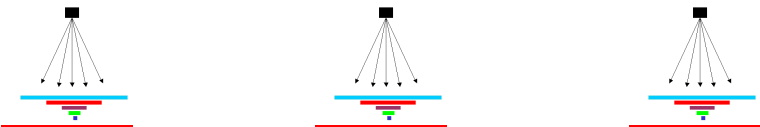
SO<sub>2</sub> VCD

AMF 313 nm

Radiance 313 nm



b) 10-11 km

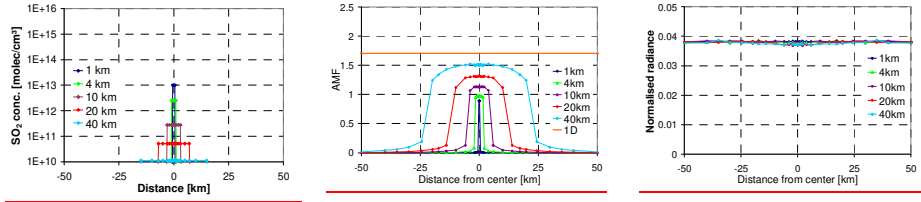


SO<sub>2</sub> scenario ,weak' with  $1 \cdot 10^{28}$  molecules in the plume

SO<sub>2</sub> VCD

AMF 313 nm

Radiance 313 nm

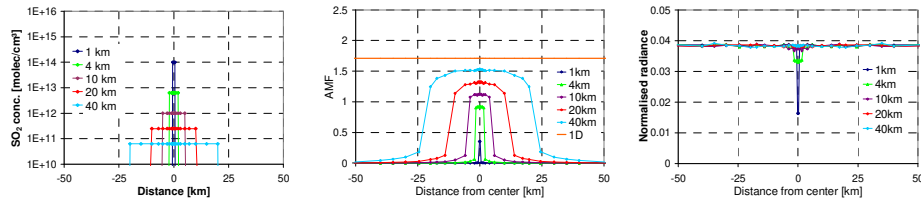


SO<sub>2</sub> scenario ,strong, 1' with  $1 \cdot 10^{29}$  molecules in the plume

SO<sub>2</sub> VCD

AMF 313 nm

Radiance 313 nm

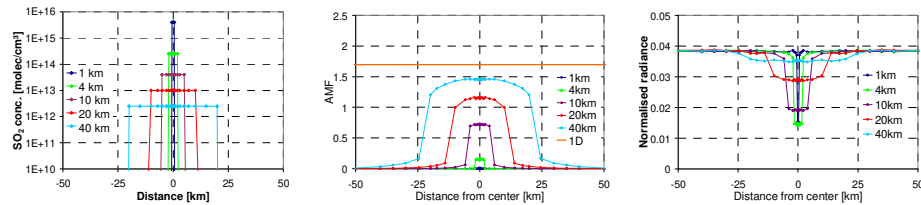


SO<sub>2</sub> scenario ,strong, 4' with  $4 \cdot 10^{30}$  molecules in the plume

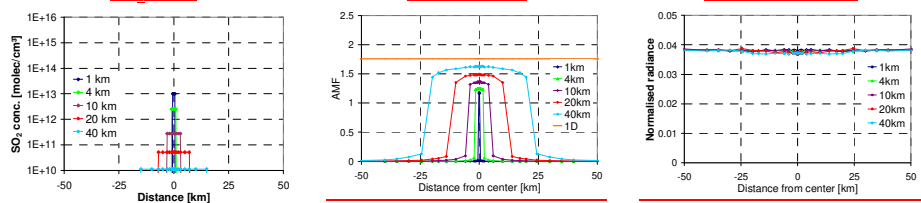
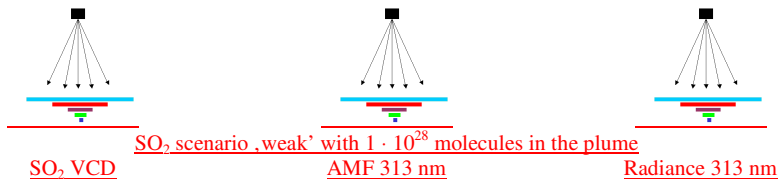
SO<sub>2</sub> VCD

AMF 313 nm

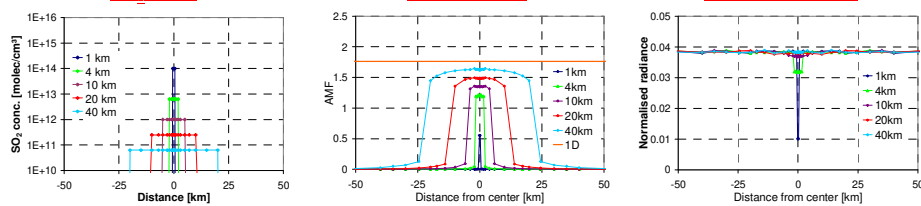
Radiance 313 nm



c) 15-16 km



SO<sub>2</sub> scenario 'strong, 1' with 1 · 10<sup>29</sup> molecules in the plume



SO<sub>2</sub> scenario 'strong, 4' with 4 · 10<sup>30</sup> molecules in the plume

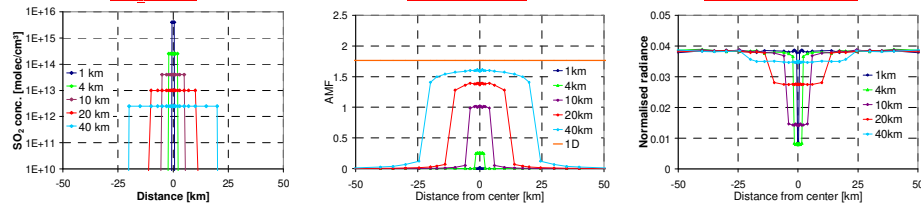


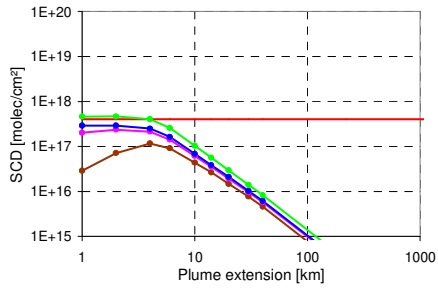
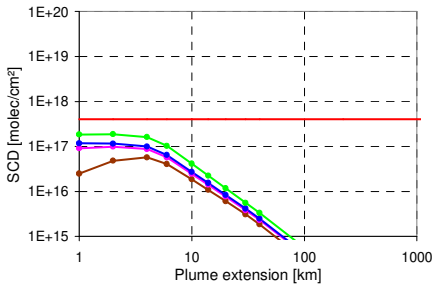
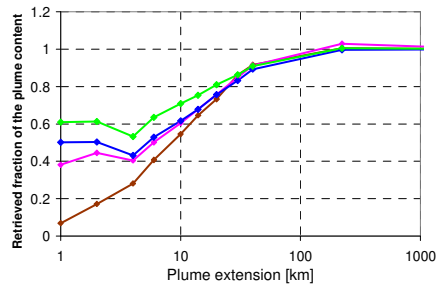
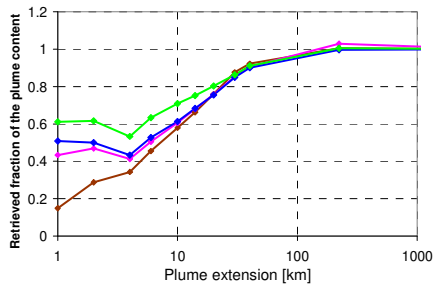
Fig. A3.4 Same as Fig. 13, but for additional plume heights: Plume scans for SO<sub>2</sub> plumes with different amounts of molecules and different horizontal extensions (for the different SO<sub>2</sub> scenarios, see table 3). Left: SO<sub>2</sub> VCDs of the plumes, middle: AMFs at 313 nm; right: normalised radiances at 313 nm.

a) 0-1km

Plume content: 1 · 10<sup>29</sup> molecules

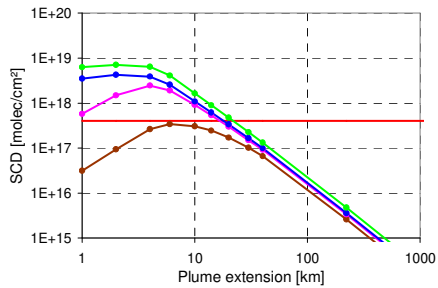
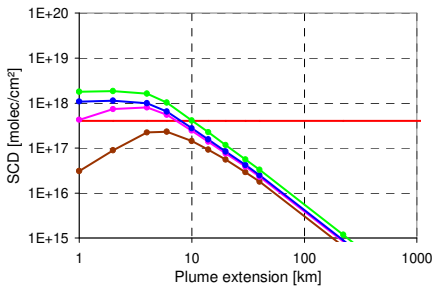
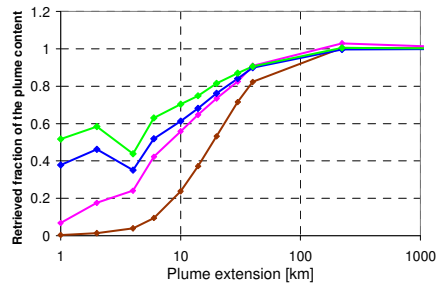
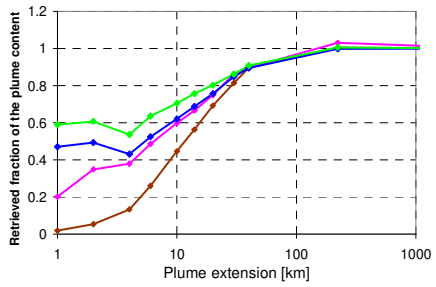
Plume content: 2.5 · 10<sup>29</sup> molecules





Plume content:  $1 \cdot 10^{30}$  molecules

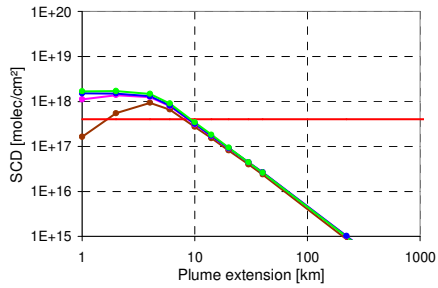
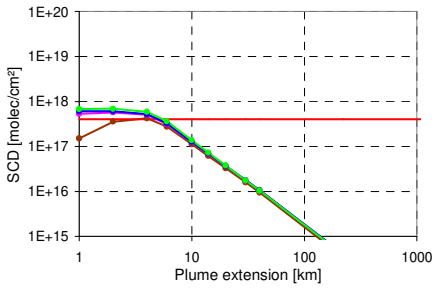
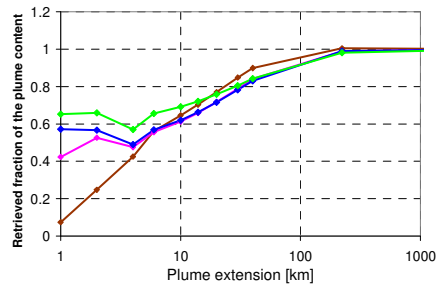
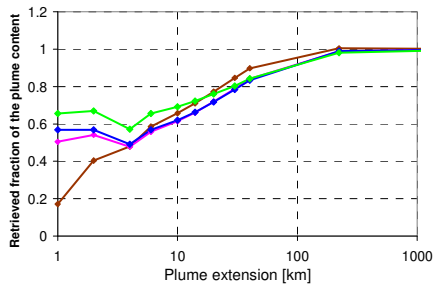
Plume content:  $4 \cdot 10^{30}$  molecules



b) 10-11km

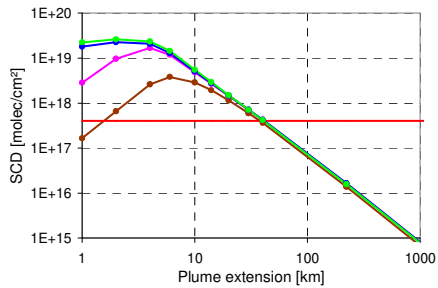
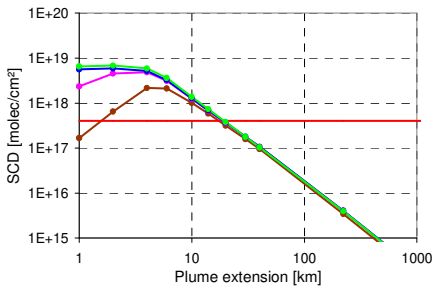
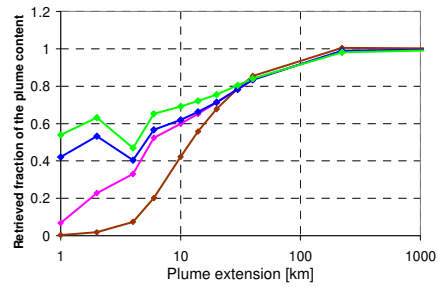
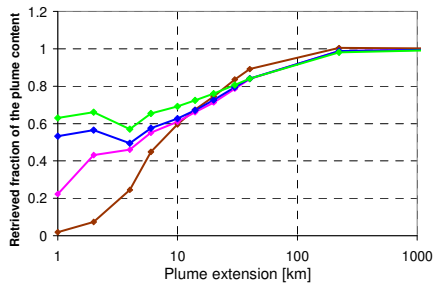
Plume content:  $1 \cdot 10^{29}$  molecules

Plume content:  $2.5 \cdot 10^{29}$  molecules



Plume content:  $1 \cdot 10^{30}$  molecules

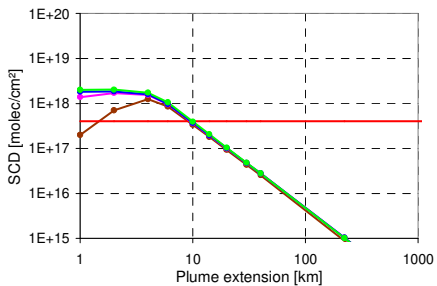
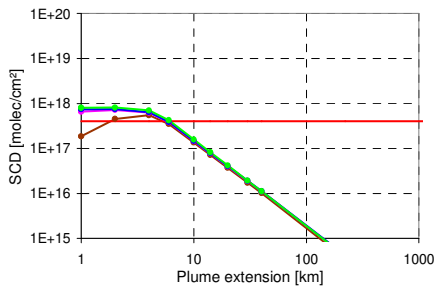
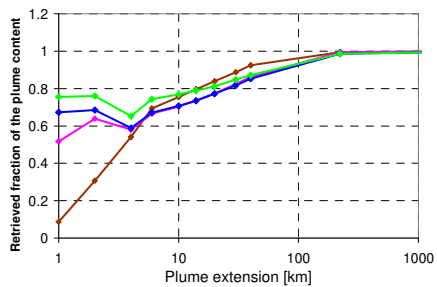
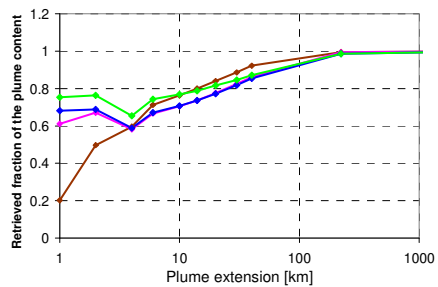
Plume content:  $4 \cdot 10^{30}$  molecules



c) 15-16km

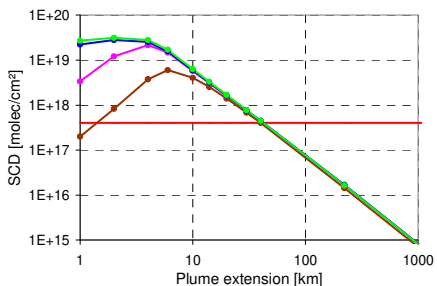
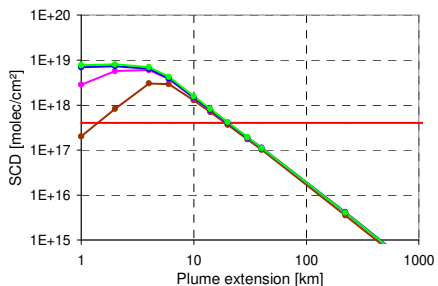
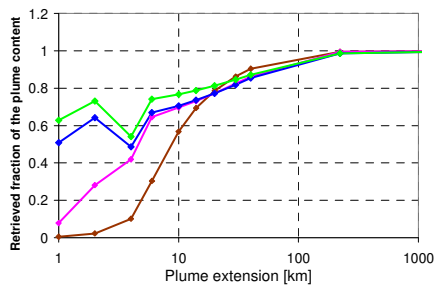
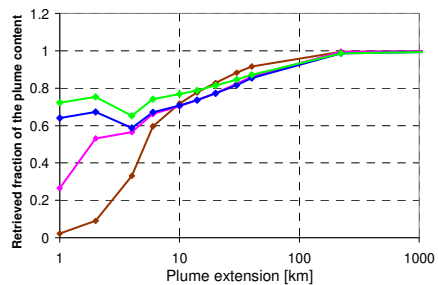
Plume content:  $1 \cdot 10^{29}$  molecules

Plume content:  $2.5 \cdot 10^{29}$  molecules



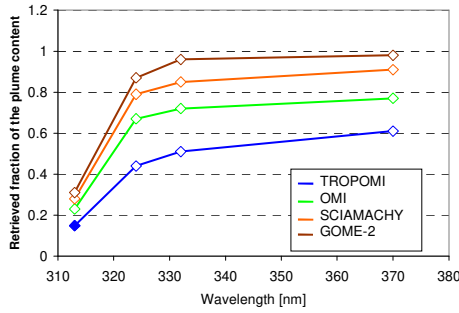
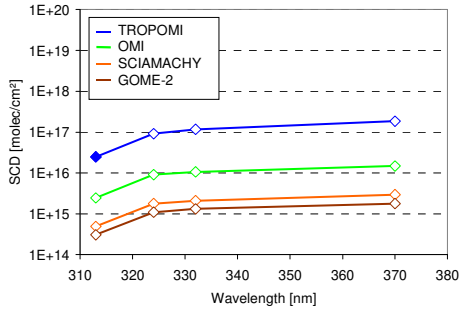
Plume content:  $1 \cdot 10^{30}$  molecules

Plume content:  $4 \cdot 10^{30}$  molecules

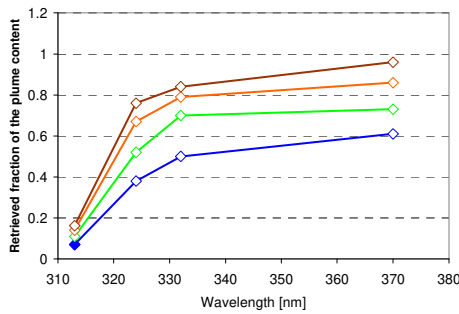
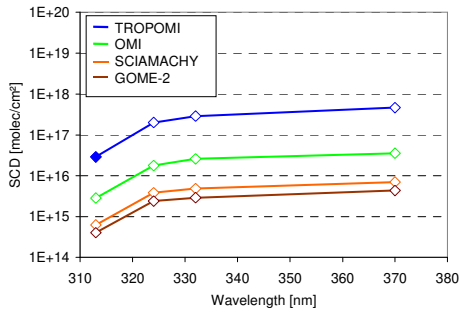


1550 **Fig. A3.5 Same as Fig. 14, but for additional plume heights: retrieved fraction of the plume content (top) and SO<sub>2</sub> SCDs (bottom) from TROPOMI measurements at different wavelengths as function of the plume size and for different amounts of molecules in the plume. The red horizontal line indicates the threshold, above which the operational SO<sub>2</sub> retrieval switches from the standard fit window to the first alternative fit window (at longer wavelengths).**

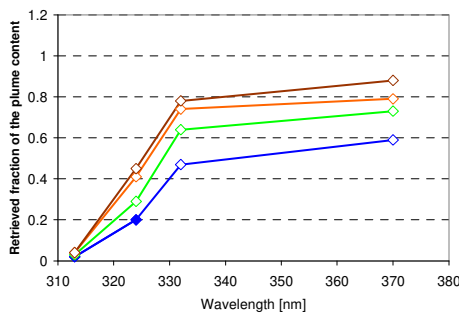
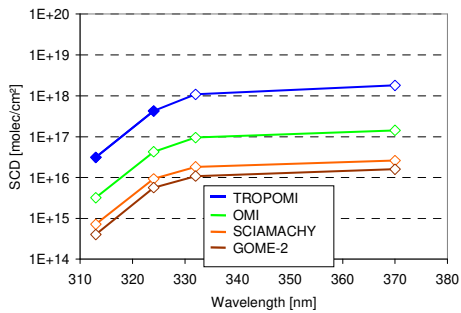
1555 0-1km  
plume content:  $1 \cdot 10^{29}$  molecules



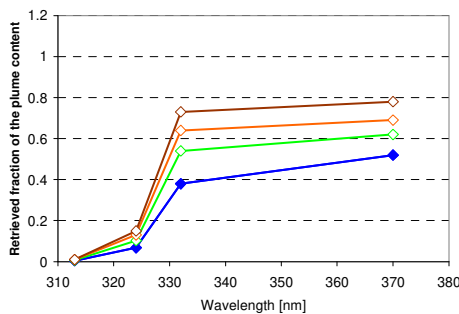
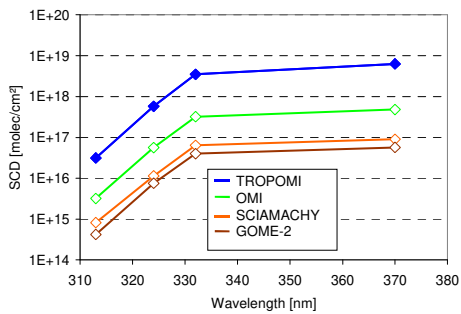
plume content:  $2.5 \cdot 10^{29}$  molecules



plume content:  $1 \cdot 10^{30}$  molecules



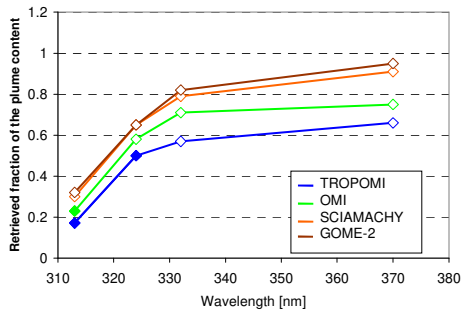
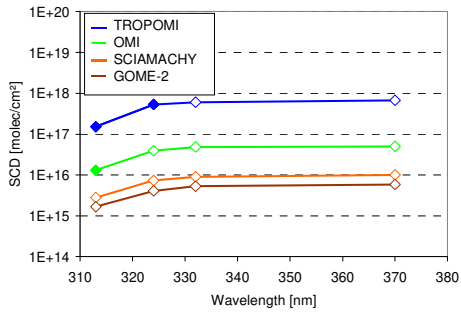
plume content:  $4 \cdot 10^{30}$  molecules



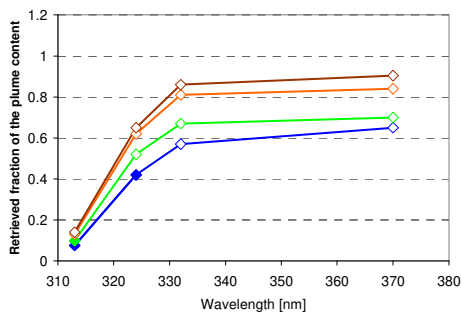
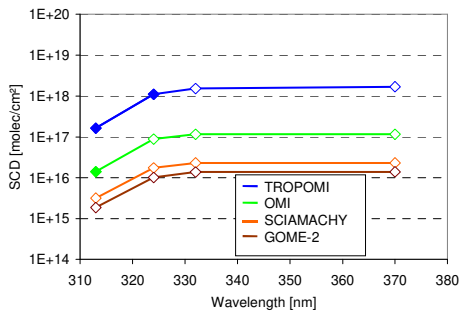
1560

10-11km

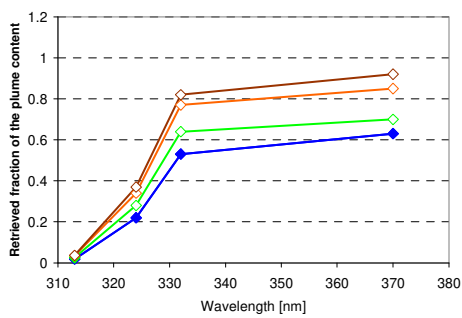
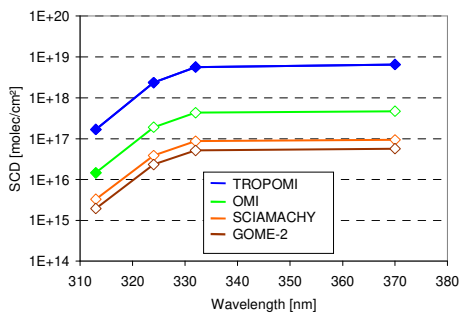
plume content:  $1 \cdot 10^{29}$  molecules



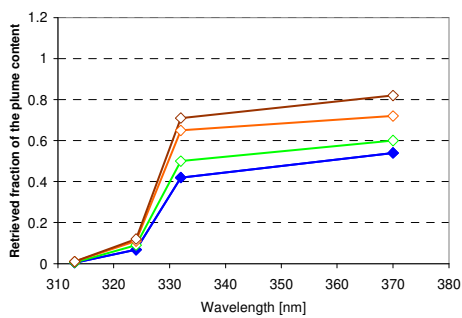
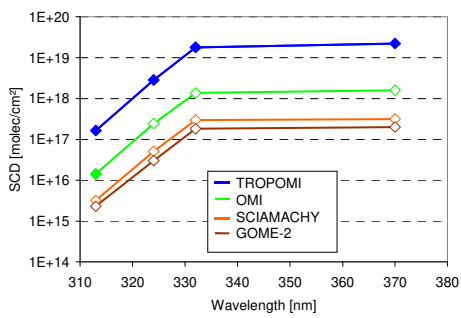
plume content:  $2.5 \cdot 10^{29}$  molecules



plume content:  $1 \cdot 10^{30}$  molecules

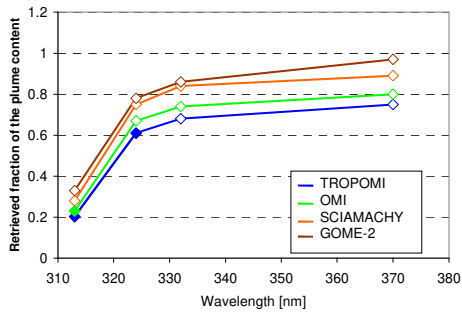
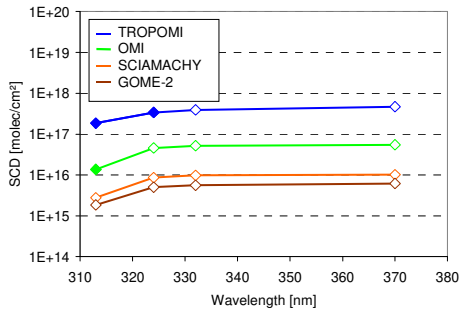


plume content:  $4 \cdot 10^{30}$  molecules

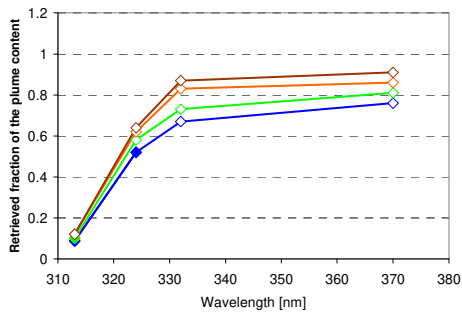
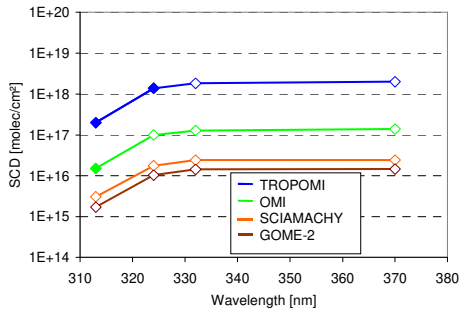


15-16km

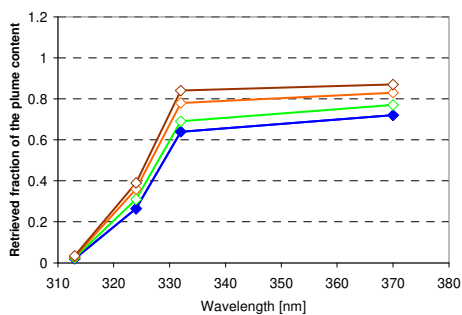
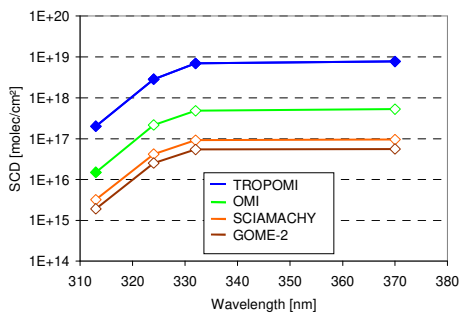
plume content:  $1 \cdot 10^{29}$  molecules



plume content:  $2.5 \cdot 10^{29}$  molecules



plume content:  $1 \cdot 10^{30}$  molecules



plume content:  $4 \cdot 10^{30}$  molecules

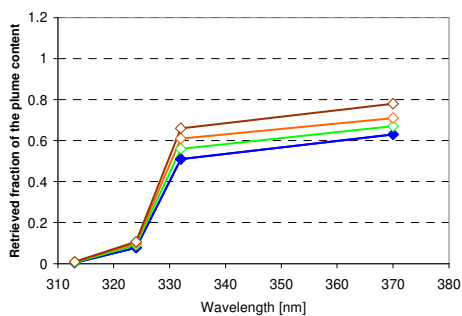
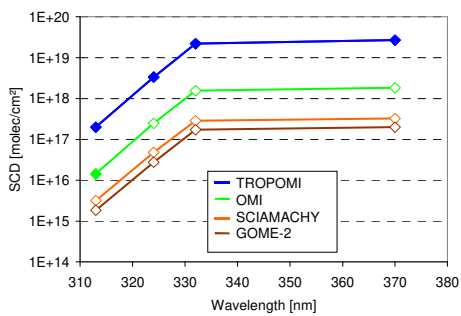


**Fig. A3.6** Same as Fig. 15, but for additional plume heights: Retrieved fractions of the plume content and SO<sub>2</sub> SCDs for different satellite instruments and for plume size of 1 x 1 km<sup>2</sup> as function of the wavelength. The full symbols represent measurements with SCDs above the detection limit. Note that for the rather large ground pixel sizes of SCIAMACHY and GOME-2 the errors are between 5 and 10%.

1565

1570

1575 **Appendix A2-A4 Effect of the wavelength dependence of the AMF**

In this section we quantify the effect of the wavelength dependence of the AMF for selected representative scenarios by the comparison of the results of two simulations:

a) monochromatic AMFs (only affected by the saturation effect)

1580 b) ‚true‘ AMFs (affected by the saturation effect and the wavelength dependence of the AMF)

The ‚true‘ AMFs are calculated in the following way (see also Marquard et al., 2000): first a measured spectrum for a selected SO<sub>2</sub> scenario is simulated at ‚high‘ spectral resolution (~0.22 FWHM, the spectral resolution of the SO<sub>2</sub> cross section). In order to minimise the computational effort for Monte Carlo simulations (and also to minimise the noise), the spectra are calculated in the following way: first a wavelength close to the center of a SO<sub>2</sub> fit range is chosen. For this

1585 wavelength, the radiance is simulated as function of the absorption cross section. Note that in order to minimise the noise the same photon trajectories are used for the simulations with different absorption cross sections. Based on the derived relationship between the radiance and the absorption cross section, a high resolution spectrum for the selected SO<sub>2</sub> scenario is calculated and convolved by the instrument slit function (here we assume a FWHM of 0.5 nm). In the next step, the simulated spectra are analysed by DOAS similar to the measured spectra. Finally, the derived SO<sub>2</sub> SCD is divided by the

1590 SO<sub>2</sub> VCD (used as input for the respective scenario) to yield the ‚true‘ AMF.

The upper part of Figure A2A4.1 shows the ‚true AMFs‘ derived for the standard fit window around 313 nm and the corresponding monochromatic AMFs for single wavelengths for 4 different plume scenarios. Additional results for 332 nm are shown in the bottom part of the figure. Besides the AMFs, also the ratios of the monochromatic AMFs and the true AMFs are shown. For scenarios with high AMFs (monochromatic AMFs > about 0.6), the difference between the

1595 monochromatic AMFs and the true AMFs is small (<10%), but for smaller AMFs, the difference increases (up to more than 50% for monochromatic AMF below about 0.4). In Fig. A2A4.2, the ratios of the true AMFs and monochromatic AMFs as function of the vertical optical depth of the SO<sub>2</sub> absorption are shown. For the same fit window, a similar dependence is found, almost independent from the SO<sub>2</sub> scenario. However, a different relationship is found for a different fit window indicating the specific spectral patterns of the SO<sub>2</sub> absorption in the different fit windows.

1600 These findings indicate that for an accurate quantitative assessment, true AMFs for selected plume scenarios and wavelengths have to be individually calculated. Nevertheless, for the wavelengths considered here, the underestimation is < 5% if the vertical OD is below about 2.5%.

It should be also noted that for scenarios with high optical depth, the ‚optical definition‘ of the AMF (equation 1) should be used for the interpretation of the measurements. For such cases, the AMFs calculated based on geometric photon trajectories

1605 (e.g. box-AMFs) will differ from those calculated by equation 1 in Pukite and Wagner (2016).

a) 313 nm,  $1 \cdot 10^{19}$  molecules      b) 313 nm,  $2.5 \cdot 10^{19}$  molecules

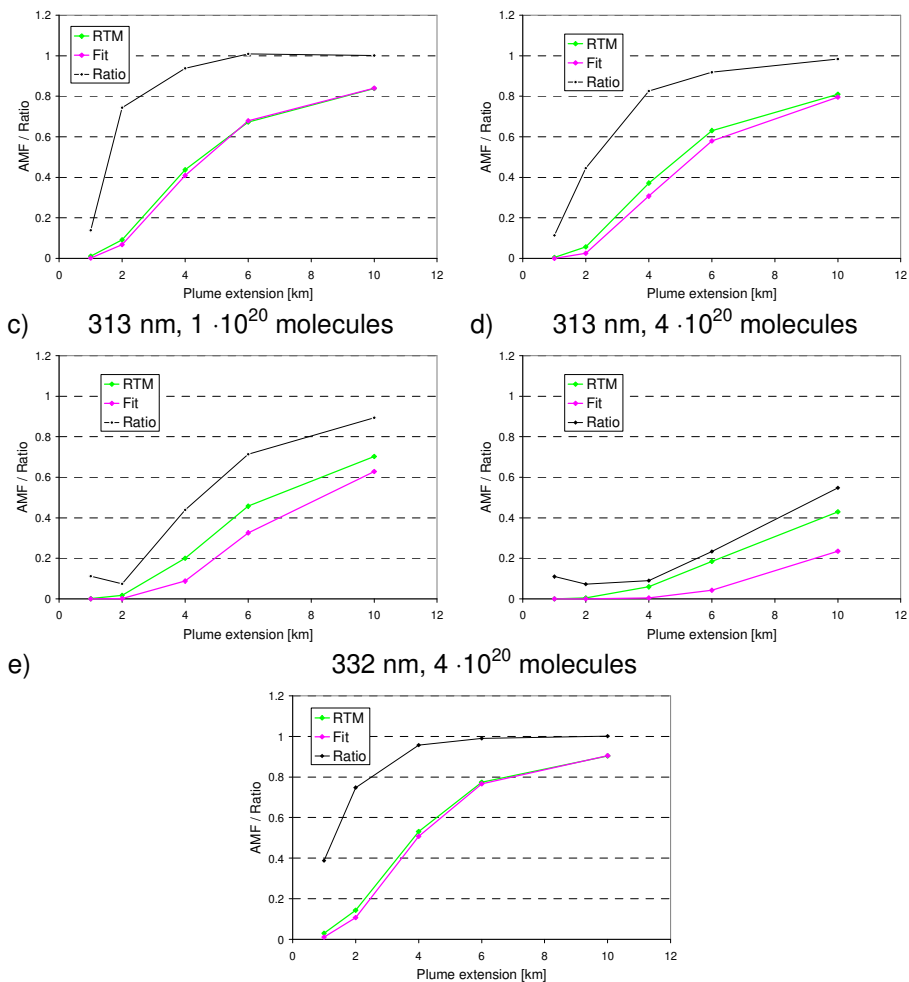
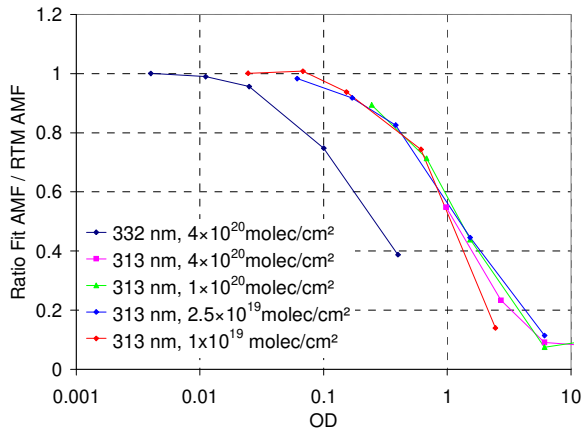


**Fig. A2A4.1** True AMFs (magenta lines) and monochromatic AMFs (green lines) as function of the horizontal plume extension for different SO<sub>2</sub> scenarios. Also the ratios of both AMFs are shown (black lines). The AMFs and AMF ratios depend on the wavelength and the SO<sub>2</sub> amount.





1615 | Fig. A2A4.2 Ratio between true AMFs and monochromatic AMFs as function of the vertical optical depth of SO<sub>2</sub> in the plume.

1620

1625

1630

1635

1640

1645

1650

1655

Appendix A3-A5 Geometric effects for  $\text{SO}_2$  (weak) at 313 nm and  $\text{BrO}$  at 340 nm

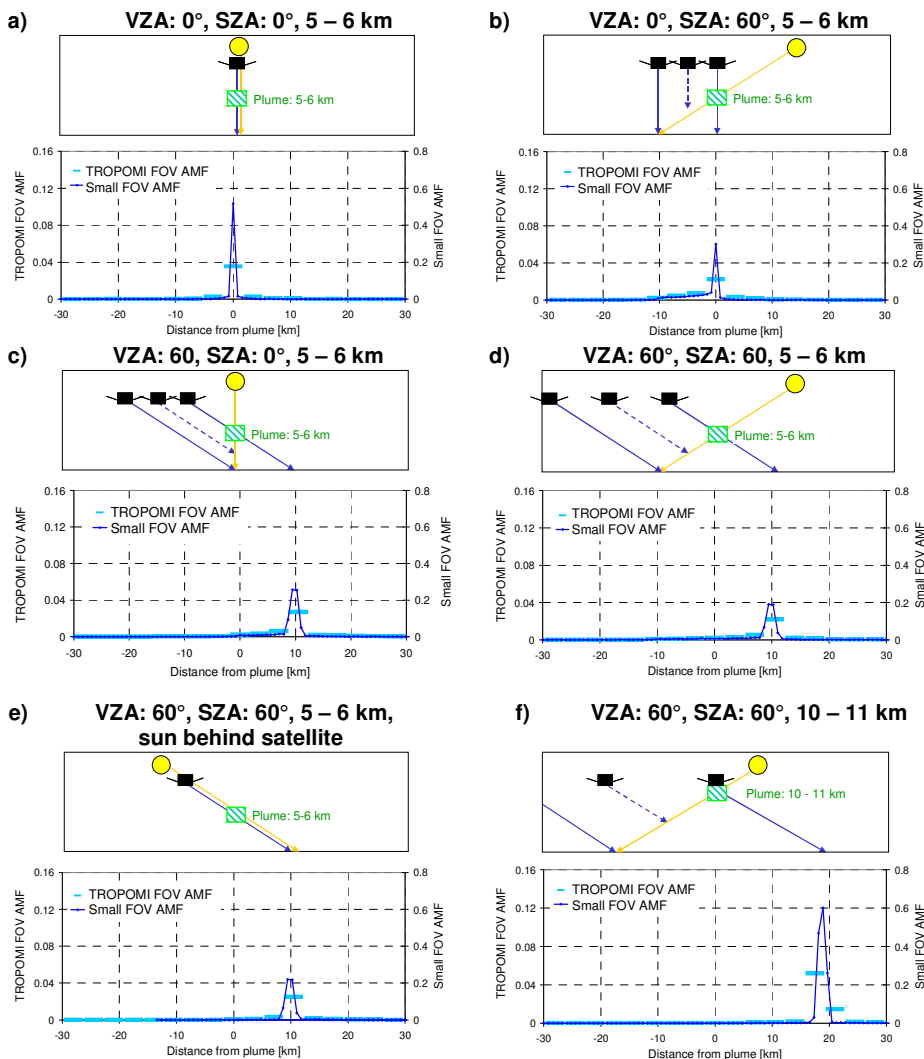
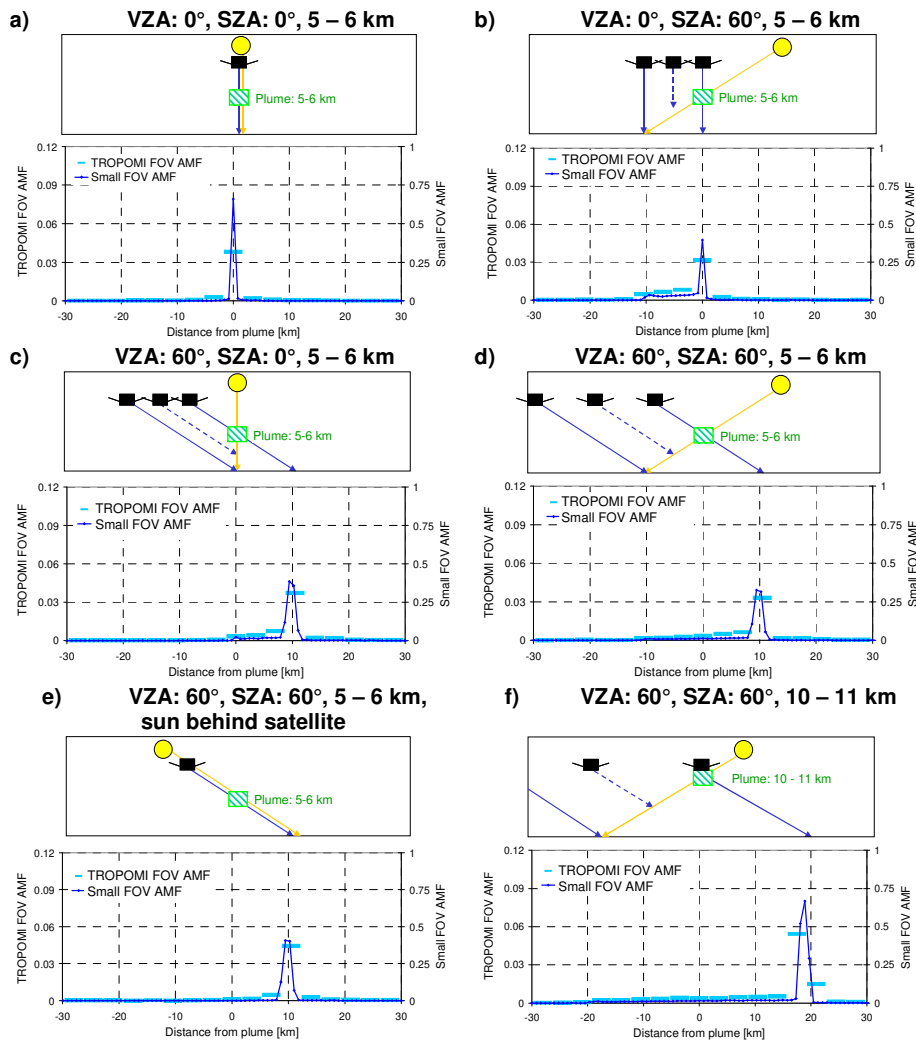


Fig. A3A5.1 AMFs for TROPOMI observations of elevated plumes for different combinations of SZA and VZA. The blue lines show the AMFs for observations with a narrow FOV ( $\sim 0.014^\circ$ ) (right y axis); the bright blue symbols represent simulations with a TROPOMI FOV (left axis). All simulations are for  $\text{SO}_2$  (weak) at 313 nm and plume sizes of  $1 \times 1 \times 1 \text{ km}^3$ .

1660

1665

1670



1675 **Fig. A3A5.2** AMFs for TROPOMI observations of elevated plumes for different combinations of SZA and VZA. The blue lines show the AMFs for observations with a narrow FOV ( $\sim 0.014^\circ$ ) (right y axis); the bright blue symbols represent simulations with a TROPOMI FOV (left axis). All simulations are for BrO at 340 nm and plume sizes of  $1 \times 1 \text{ km}^3$ .